Accelerating Computations for Oil and Gas Problems: Reduced Physical Modeling of Hydraulic Fracturing and High-Performance Computing for Fluid Flow in a Porous Medium

by
Innokentiy Protasov

A dissertation submitted to the Department of Civil & Environmental Engineering,
Cullen College of Engineering
in partial fulfillment of the requirements for the degree of

Doctor of Philosophy
in Civil Engineering

Chair of Committee: Roberto Ballarini
Committee Member: Egor Dontsov
Committee Member: Pradeep Sharma
Committee Member: Christine Ehlig-Economides
Committee Member: Konrad Krakowiak
Committee Member: Mostafa Momen

University of Houston
August 2020

ACKNOWLEDGMENTS

I express my earnest gratitude to the people whose support made this work possible.

First and foremost, I would like to thank my academic advisors, Dr. Roberto Ballarini and Dr. Egor Dontsov, with whom I had the privilege to work. Their guidance and friendship in research and life are invaluable. They taught me not only how to excel in academic studies but also how to be a productive researcher. I much appreciate their inspiration and patience, which I will always remember.

I am grateful to Dr. Anthony Peirce for his discussions on the aspects of hydraulic fracture modeling and for performing and providing numerical simulations using the ILSA model. Validation of the algorithms developed in this work primarily relies on his data.

I would like to thank the members of the dissertation committee, Dr. Pradeep Sharma, Dr. Christine Ehlig-Economides, Dr. Konrad Krakowiak, and Dr. Mostafa Momen, for their attentive review of this work.

The last chapter of this dissertation presents the results of the work performed during the National Renewable Energy Lab internship in collaboration with Dr. Justin Chang and Dr. Jeffery Allen. I am grateful to them for teaching me a lot about high-performance computing and computer science aspects of physical modeling.

I appreciate computational resources provided by the Research Computing Data Core at the University of Houston. Furthermore, I would like to thank Dr. Amit Amritkar for his discussion on high-performance computing.

The support of the University of Houston in the form of graduate tuition fellowship and Houston Endowment fellowship is greatly acknowledged.

Last but not least, I am grateful to my family and friends who supported me throughout this academic journey.

ABSTRACT

The mechanical modeling of hydraulic fractures is a mathematically complex problem involving the coupling between the equations that describe fracturing of and fluid flow through the porous rock, and fluid flow inside the fractures. Simulation of these physical processes can offer critical insights into practical design problems associated with hydraulic fracturing technology. However, exploration of the influence of the relatively large number of control variables defining the design space is limited by the available computational resources. Generally speaking, the computational time can become a bottleneck for practical usage of available hydraulic fracture simulators. Acknowledging this limitation, this thesis presents a series of combined analytical-computational models that enable efficient simulation of the propagation of multiple non-planar hydraulic fractures, within the context of hardware-conscious advanced numerical techniques.

Hydraulic fracture simulations are often coupled with the fluid flow within the surrounding porous rock. This thesis realizes the need for computationally efficient porous media flow simulations that achieve a similar level of efficiency as the fast hydraulic fracturing models. Remarkable computational efficiency is achieved through the novel formulations of numerical techniques and the state-of-the-art computational methods: reduced-order modeling of the hydraulic fracturing, and the application of physical block solvers to the porous media flow.

TABLE OF CONTENTS

LIST OF TABLES

LIST OF FIGURES

List of Abbreviations

1D	one-dimensional;
2D	two-dimensional;
KGD	Khristianovich-Geertsma-De Klerk;
PKN	Perkins-Kern-Nordgren;
EPKN	enhanced Perkins-Kern-Nordgren;
mEPKN	enhanced Perkins-Kern-Nordgren for multiple fractures;
P3D	pseudo-3D;
EP3D	enhanced pseudo-3D;
mEP3D	enhanced pseudo-3D for multiple fractures;
ILSA	implicit level set algorithm;
DDM	displacement discontinuity method;
EDDM	elliptic displacement discontinuity method;
2D DDM	two-dimensional displacement discontinuity method;
LEFM	linear elastic fracture mechanics;
FEniCS	finite element computer software;
pFibs	parallel FEniCS implementation of block solvers;
DPP	double porosity-permeability.

1 Introduction and motivation

Hydraulic fracturing refers to the process of initiating and propagating cracks within a rock formation by injection of a highly pressurized fluid. This technology, which creates permeable channels within the reservoir that allow the hydrocarbons to flow to the surface, has been successfully implemented by the petroleum industry since the late 1940s to stimulate oil and gas wells (Montgomery and Smith, 2010; Economides and Nolte, 2000). Other applications of hydraulic fracturing include waste disposal (Abou-Sayed et al., 1989), rock mining (Jeffrey and Mills, 2000), and geothermal energy extraction (Brown, 2000).

Modeling of fluid pressure-driven cracks has become an integral part of the hydraulic fracturing treatment by providing guidance for characterizing and stimulating reservoirs. The physical processes occurring during hydraulic fracturing include the initiation and propagation of the fractures within the rock formation, the flow of the pressurized fluid inside the fractures, and the flow of the fluids present in the reservoir. The early hydraulic fracture models, which include those of Khristianovich-Geertsma-De Klerk (KGD) (Khristianovic and Zheltov, 1955; Geertsma and De Klerk, 1969), Perkins-Kern-Nordgren (PKN) (Perkins and Kern, 1961; Nordgren, 1972), radial (Abe et al., 1976), and the pseudo-3D (P3D) (Settari and Cleary, 1986; McLennan and Picardy, 1985), are amenable to analytical treatment because they are based on highly simplified physical descriptions. However, the stringent assumptions adopted by the models severely limit their range of applicability (Warpinski et al., 1993). With the advances in computational power, more realistic and in turn complex numerical models have been presented for a three-dimensional crack configuration (Vandamme and Curran, 1989; Sherman et al., 2015; Kumar and Ghassemi, 2015; Dontsov and Peirce, 2017) and multiple hydraulic fractures (Kresse et al., 2013; Damjanac et al., 2013; Wu et al., 2017; Dontsov and Peirce, 2016b). The complexity of numerical models

used as a design tool for hydraulic fracturing treatment is limited by the amount of available computational resources. While, in some cases, expensive simulations are justified, the computational efficiency of hydraulic fracture models is critical to the practical exploration of the design parameter space. These design applications benefit from trading some of the accuracy of the numerical solution for better computational efficiency. However, this pursuit may come at the cost of low accuracy and possibly, for certain situations, unrealistic results. A detailed review of recent advances in numerical modeling of hydraulic fracturing is presented in (Adachi et al., 2007; Lecampion et al., 2018).

This study is dedicated to the investigation and further advancing of computationally efficient and accurate methods of hydraulic fracture modeling that account for fluid-driven propagation of cracks within and the flow of fluid throughout a porous rock formation. The classical approach in hydraulic fracture models consists of the analysis of a crack in an elastic medium whose surfaces are pressurized by a fluid (Adachi et al., 2007; Peirce and Detournay, 2008). Some models consider the flow of fluids in the medium containing the cracks, which is important for understanding the transfer of reservoir fluid during and after the hydraulic fracturing treatment. Models have also been formulated that account for the effects on fracture propagation of the additional stresses arising from the flow of fluid through the porous rock (Boone and Ingraffea, 1990; Vandamme and Roegiers, 1990; Kovalyshen, 2010; Sherman et al., 2015; Yoshioka and Bourdin, 2016; Damjanac and Cundall, 2016; Baykin and Golovin, 2018; McClure et al., 2018; Rezaei et al., 2019; Chukwudozie et al., 2019). This suggests that the "full" problem can be expanded into two coupled sub-problems: one that considers the propagation within a rock formation of a crack whose surfaces are pressurized by a flowing fluid, and another that considers fluid flow within the rock formation. The coupling comes via the flow and traction boundary

conditions on the crack surface. The first problem will henceforth be referred to as the hydraulic fracture problem, and the second one will be referred to as the fluid flow problem.

Due to the two-dimensional (2D) nature of a crack's geometry, the fracture propagation problem can be formulated solely in terms of fracture opening and tractions over the crack surface, without specifying solid media deformations and stress elsewhere. This method, which is referred to as the boundary element method, reduces the boundary value problem to an integral equation over the crack surface. The method, therefore, significantly decreases the number of unknowns in the simulations, in that the fields within the volume are not involved in the solution procedure. This is in contrast to the finite element method, in which the unknowns include the displacements throughout the volume. However, because the boundary element method operates on integral equations, the discretization leads to a dense system of algebraic equations, while the finite element method results in a sparse system. From the computational point of view, the numerical solution of dense systems of equations is arithmetically more intensive than that of sparse systems, meaning that it requires more basic arithmetic operations performed by the computing unit. As a result, if the problem size is large, the boundary element method requires a significantly larger number of computing unit operations than the finite element method. At the same time, the boundary element method's requirements for computer memory are significantly smaller than those of the finite element method. An important feature of the boundary element method is the convenience of deriving reduced-order models, which replace the original formulation by an approximate model preserving the most important physical phenomena. Reduced-order models offer a balance between accuracy and computational efficiency, but this approach is problem specific and requires a deep understanding of key physical processes. Such models have been extensively

studied and implemented in fracture simulations (Kresse et al., 2013; Wu et al., 2017, 2012; Olson, 2008; Adachi and Peirce, 2008; Weng, 1992; Dontsov and Peirce, 2015a, 2016a; Wu and Olson, 2015; Dontsov et al., 2019). This study focuses on the further development of this approach in the context of multiple interacting non-planar hydraulic fractures.

The problem of fluid flow outside cracks often complements the hydraulic fracture propagation problem, either as a simplified empirical law, as a set of governing equations for three-dimensional fluid flow through poroelastic medium, or as something in between (Carter, 1957; Kanin et al., 2020b,a; Boone and Ingraffea, 1990; Boone et al., 1991; Vandamme and Roegiers, 1990; Sherman et al., 2015; Rezaei et al., 2019; Chukwudozie et al., 2019). Three-dimensional porous media flow offers the best accuracy for multiple fractures of complex topology. Because the domain of interest involves the whole three-dimensional space, the problem is formulated using the finite element method. As was mentioned, in this case, the number of unknowns in the equations is much larger than in the fracture propagation problem. However, the efficiency of finite element simulations can be increased by using special methods of solving sparse systems of equations, in the way the boundary element method cannot. Modern approaches employ splitting matrices into blocks based on the physics of the problem and then applying preconditioners and solvers to each block (Brown et al., 2012). In this study, we undertake this approach in the context of porous media fluid flow problems.

To summarize, this dissertation includes the following objectives:

(1) Develop a computationally efficient reduced-order model for multiple non-planar hydraulic fractures and assess the accuracy of its predictions with those of reference models, for a wide range of problem parameters.

(2) Accelerate finite element method simulations of fluid flow problems by using

iterative block solvers and preconditioners for algebraic linear systems.

The coupling of the reduced-order models for hydraulic fracturing with the three-dimensional fluid flow in porous media may not be reasonable, because those models typically have significantly different levels of computational efficiency. However, as the model order reduction accelerates the hydraulic fracturing problem, the state-of-the-art computational techniques developed for the finite element simulations may bring the computational efficiency to the level comparable with that of the reduced-order models for hydraulic fracturing. Therefore, we identified the stated objectives with the intent to make such coupling justified.

The dissertation is structured as follows. Chapter 2 presents the problem formulation for multiple non-planar hydraulic fractures and describes the concept of model order reduction. A review of hydraulic fracture models for multiple cracks is discussed in Section 2.1. Problem statement and assumptions are given in Section 2.2. Governing equations for the fully 3D problem are presented in Section 2.3. The concept of model order reduction is explained in Section 2.4.

Chapter 3 introduces the reduced-order model for multiple planar hydraulic fractures with constant height, which is a development of the enhanced blade-like model for a single crack. The first goal of this chapter is to highlight the differences between various types of reduced-order models for hydraulic fracturing. In particular, we investigate local and non-local approaches to elasticity, which, together with the lubrication equation, represent the physical processes related to solid deformations, fracture toughness, and fluid viscosity. Because leak-off has little influence on the aforementioned processes, it is omitted in this chapter. The second goal of this chapter is to evaluate the accuracy and limitations of the developed reduced-order model. The model is validated against the reference fully 3D model for single and multiple fracture cases. One observed limitation, related to the inaccuracy of fluid pressure, is

addressed in Chapter 4. The history of blade-like hydraulic fracture models, range of applicability, and assumptions are described in Section 3.1. The governing equations of the reduced model for multiple planar hydraulic fractures with constant height are presented in Section 3.2. The results of the model are validated in planar cracks case for a broad range of parameters in Section 3.3. The summary of the chapter is given in Section 3.4. The limitations of the model are addressed in the next chapter.

In Chapter 4, the more advanced reduced-order model for multiple non-planar hydraulic fractures is presented. In particular, the following limitations of the model in Chapter 3 are addressed: constant height assumption, inability to model fractures at early times, planar fracture configurations, and inaccurate global fluid balance evaluation. The model is based on the enhanced pseudo-3D model and extends the approach to the case of multiple cracks, aimed to overcome the first two limitations. The non-planar fractures are introduced, whose propagation paths are determined by enforcing that their front is associated with a null Mode II stress intensity factor. The last limitation is addressed by deriving the correction for fluid pressure near the wellbore. The description of the pseudo-3D class of models and basic assumptions are given in Section 4.1. The governing equations of the reduced-order model for multiple non-planar hydraulic fractures are presented in Section 4.2. The results of the model validation for planar cracks and fracture turning are detailed in Section 4.3. The summary of the chapter is given in Section 4.4.

Chapter 5 describes the problem of fluid flow in porous media, which is often solved in conjunction with the hydraulic fracturing problem. The motivation for such coupling is described in Section 5.1. The governing equations for the coupled system, including the poroelasticity, porous media fluid flow, and the fracture propagation, are presented in Section 5.2. Section 5.3 presents the computational paradigm for efficient and scalable modeling of porous media flow via Darcy 's model and double

porosity-permeability model. The scaling results are computed with the developed software package and well-established scientific libraries. The chapter is summarized in Section 5.4. Note that the implementation of the coupling itself is left to future work.

Chapter 6 concludes the dissertation by summarizing the main objectives and the results of the study, and also proposing future work topics. The chapter is followed by the reference list and appendices.

2 Problem formulation for multiple non-planar hydraulic fractures

2.1 Background

This chapter introduces the mathematical model for multiple non-planar hydraulic fractures and describes the concept of model order reduction. Due to the focus on the fracture propagation processes, the formulation considers the porous media flow in its simplified version through Carter's law. Particularly, the boundary condition for the fluid flow into the surrounding rock is represented by a simplified diffusion model, uncoupling the fracture problem from the three-dimensional porous media flow problem. The rock deformations are modeled according to linear elasticity, via the integral equations arising in the displacement discontinuity method (DDM). The fluid flow inside the cracks is modeled according to the lubrication theory. Problem statement and assumptions are detailed in Section 2.2. Governing equations for the fully 3D problem are presented in Section 2.3. The concept of model order reduction is explained in Section 2.4.

2.2 Problem statement and assumptions

We consider the problem of multiple interacting hydraulic fractures growing inside a rock formation of homogeneous properties that is subjected to three layers of confining stress, as illustrated in Fig. 1. The rock is assumed to be linear elastic, brittle, and permeable, whereby its properties are characterized by Young's modulus E, Poisson's ratio ν, Mode I fracture toughness K_{Ic}, and Carter's leak-off coefficient C_L (Carter, 1957). The fracturing fluid is incompressible Newtonian with dynamic viscosity μ; the effect of gravity on the fluid pressure is neglected. We assume zero fluid lag at the fracture front, which is typically the case under high confinement

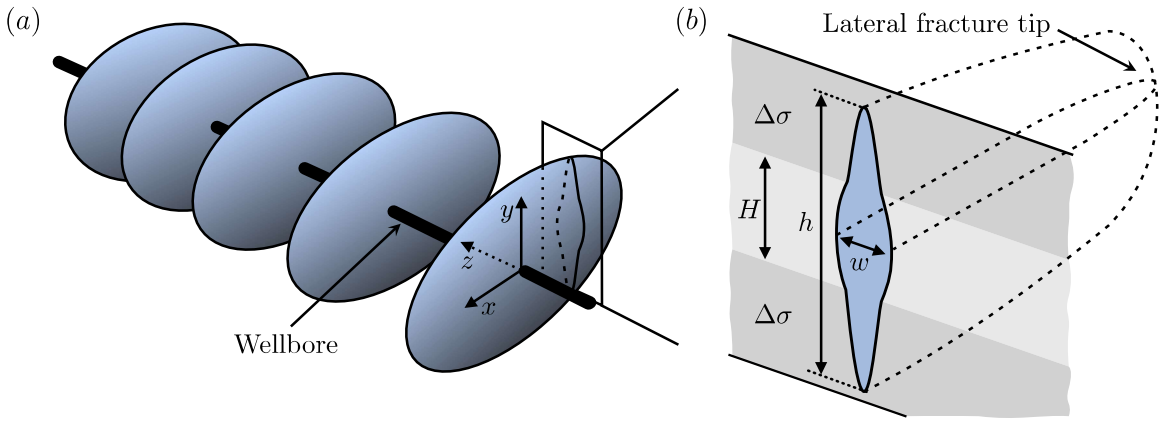

Figure 1: (a) Schematics of multiple hydraulic fractures propagating from a wellbore inside a rock with symmetric stress barriers. (b) Scheme of a vertical cross-section of a hydraulic fracture inside a rock with symmetric stress barriers.

conditions occurring underground (Garagash and Detournay, 2000; Detournay and Garagash, 2003; Detournay and Peirce, 2014).

With the reference to Fig. 1a, the global coordinate system $\mathbf{x} = (x, y, z)$ is centered at the injection point of the first fracture with the z-axis being parallel to the wellbore that is drilled in the minimum horizontal stress direction. The y-axis is referred to as the vertical direction and is parallel to the vertical stress, while the x-axis is parallel to the maximum horizontal stress direction. It is also assumed that the fractures remain vertical non-planar, i.e., that they can turn only in the xz-plane. This is a reasonable assumption since the vertical stress is much larger than the horizontal stresses under the typical operating conditions. Figure 1b shows a vertical cross-section of a hydraulic fracture subjected to stress barriers, where h is the total fracture height, and w is fracture opening. We assume that the confining stress in the three layers is distributed symmetrically with respect to the y-axis so that the middle layer with height H is subjected to the compressive stress σ, while the magnitude of the stress in the surrounding layers is increased by $\Delta\sigma$.

The formulation of the mathematical model follows the description provided next. We consider N_f vertical hydraulic fractures that are driven by fluid injected from the

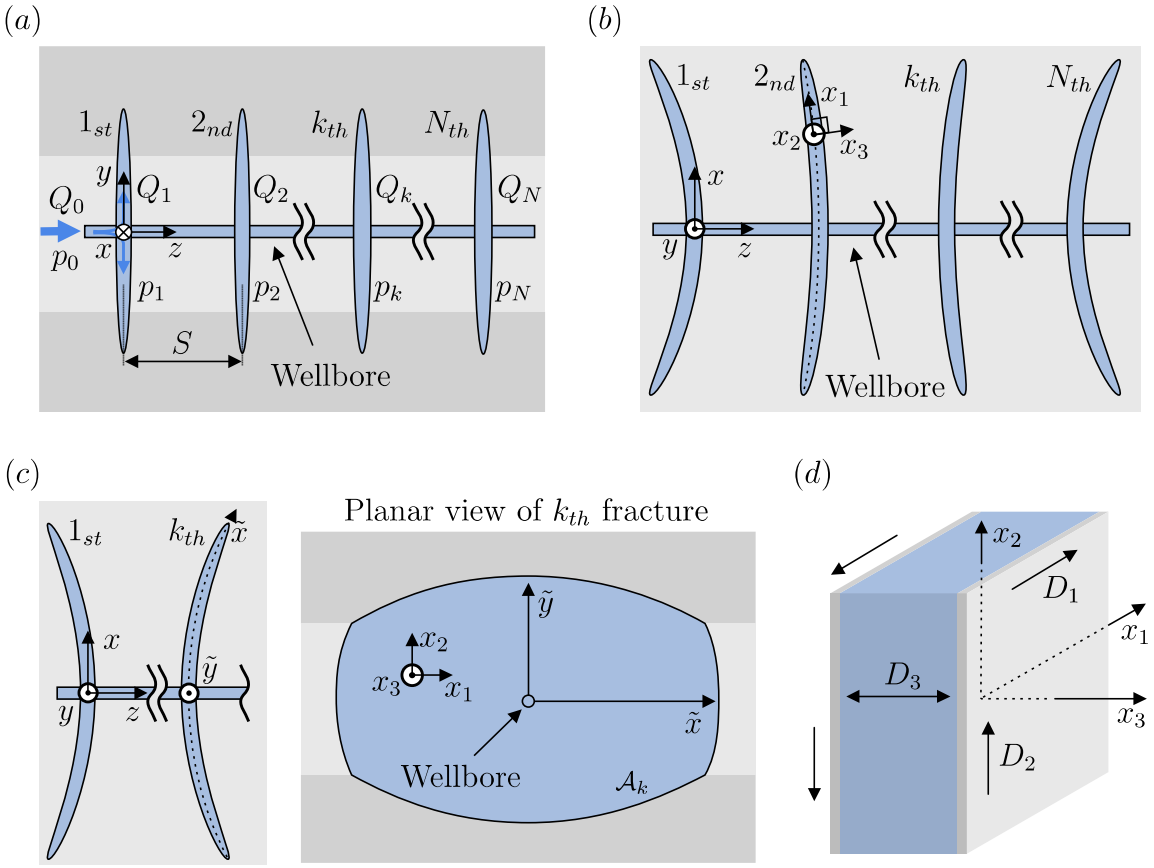

Figure 2: (a) Side view of the hydraulic fracture problem for N fractures; fractures are vertical; the total injection rate Q_0 is distributed between the fractures. (b) Top view of the hydraulic fracture problem; Fractures can be non-planar. (c) Top view of the kth hydraulic fracture and its unfolded planar view. (d) Schematics of the deformations caused by the displacement discontinuity vector in the local coordinate system.

horizontal wellbore located in the middle layer. Figure 2a shows a side view of the problem. The spacing between neighboring perforations in the wellbore from which the cracks originate is denoted by S. The fluid pressure inside the wellbore, p_0, is considered to be spatially constant, i.e., the pipe friction is neglected. However, the perforation pressure drop, caused by fluid entering the fractures through narrow perforation holes, is included. Consequently, the pressure inside the fracture at the location of the wellbore differs from p_0 and is denoted by p_k for the kth fracture. The total injection rate Q_0 is distributed between the fractures, such that the kth fracture receives the injection rate Q_k. Note that the cross-sections of the fractures in Fig. 2a are vertical.

Figure 2b is the top view of the non-planar (curved) fractures. For the purpose of computation of the stress interaction between the fractures, a local coordinate system (x_1, x_2, x_3) is introduced. These directions are defined, such that x_1 lies along the fracture, x_2 is vertical, and x_3 is perpendicular to the fracture surface.

The thin laminar flow inside the fracture can be approximated using lubrication theory and formulated as a two-dimensional problem over the fracture surface. Since the fracture surface may be curved, we utilize the coordinates $\tilde{x}$ and $\tilde{y}$ that represent the position along the fracture length and height, respectively, with the origin being at the injection point. The relation between the coordinate systems is shown in Fig. 2c. Note that each fracture has its own set of coordinates.

The elastic interaction between the fractures is formulated using the displacement discontinuity method. Let the displacement discontinuity vector across the fracture surface be $\mathbf{D}$. It is convenient to consider $\mathbf{D}$ in the local coordinate system x_1, x_2, and x_3, shown in Fig. 2d. For the displacements u_i $(i = 1, 2, 3)$ corresponding to the directions of the local coordinate system, the components of the displacement

discontinuity vector $\mathbf{D}$ are defined as

$$D_i = u_i\Big|_{x_3=+0} - u_i\Big|_{x_3=-0}, \quad i = 1, 2, 3, \tag{2.1}$$

where D_1, D_2 are the shear components (crack-sliding displacements) and D_3 is the normal component (crack-opening displacement). The crack-opening displacement is henceforth written as w, i.e., the fracture width.

As mentioned previously, modeling propagation of multiple hydraulic fractures requires the coupling of the following physical phenomena: i) elastic equilibrium of the rock medium in view of the presence of multiple fractures in a formation, ii) fluid distribution between the fractures, iii) viscous fluid flow and the associated pressure drop along the fracture, and iv) the propagation condition that governs the position of the fracture front. All are addressed in the next section within the context of 3D fractures. These relations will then be used as a basis for constructing the reduced pseudo-3D models. As detailed in the next sections, the problem is formulated in terms of fracture opening $w(\mathbf{x}, t)$ and the position of a fracture front at any time t. To reduce the number of numerical constants, the following definitions are adopted in this paper:

$$\mu' = 12\mu, \quad E' = \frac{E}{1-\nu^2}, \quad K' = 4\left(\frac{2}{\pi}\right)^{1/2} K_{Ic}, \quad C' = 2C_L, \tag{2.2}$$

where E' is the plane strain modulus, μ' is the scaled fluid viscosity, C' is the scaled leak-off coefficient, and K' is the scaled fracture toughness of the rock formation.

2.3 Governing equations for fully 3D problem

Elasticity relation. First, we present the integral equations that relate stresses and displacements in the displacement discontinuity method (Crouch and Starfield,

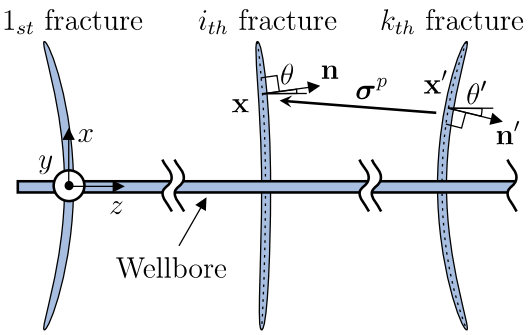

Figure 3: Elastic interaction between fractures.

1983; Hills et al., 1996). Figure 3 schematically shows the problem, in which the opening of the k_{th} fracture at $\mathbf{x}'$ imparts a stress field at the surface of the i_{th} fracture at $\mathbf{x}$. Because the fracture surfaces may be curved, we define the normal to the fracture surface at $\mathbf{x}'$ as $\mathbf{n}'$, and the normal at $\mathbf{x}$ as $\mathbf{n}$. The angle between the positive direction of the z-axis and $\mathbf{n}$ is denoted as θ, and for $\mathbf{n}'$ as θ'.

The stresses produced by the displacement discontinuity (DD) field can be calculated based on the Green's function approach. Therefore, we consider a point displacement discontinuity at $\mathbf{x}'$ that induces a stress field at $\mathbf{x}$. Since $\mathbf{x}$ and $\mathbf{x}'$ have different local coordinate systems, it is necessary to introduce coordinate transformations. The vector $\mathbf{x} - \mathbf{x}'$ is expressed as x_1, x_2, x_3 in the system local to $\mathbf{x}'$. The stress tensor in terms of x_1, x_2, x_3 and D_1, D_2, D_3, in the local coordinate system, is denoted by $\boldsymbol{\sigma}^p$ and is expressed in terms of the derivatives of the potential

$$\phi_i = \frac{D_i}{\sqrt{x_1^2 + x_2^2 + x_3^2}}, \quad i = 1, 2, 3. \tag{2.3}$$

The exact relation between $\boldsymbol{\sigma}^p$ and ϕ_i is given in Appendix A. The same stress tensor in the coordinate system local to $\mathbf{x}$, is found via tensor transformation,

$$\hat{\boldsymbol{\sigma}}^p(\mathbf{x}, \mathbf{x}') = \mathbf{T}(\mathbf{x}, \mathbf{x}')\boldsymbol{\sigma}^p(\mathbf{x} - \mathbf{x}')\mathbf{T}(\mathbf{x}, \mathbf{x}')^T, \tag{2.4}$$

where $\mathbf{T}$ is the matrix of rotation from the local coordinate system at $\mathbf{x}'$ to the local system at $\mathbf{x}$:

$$\mathbf{T} = \begin{pmatrix} \cos(\theta - \theta') & 0 & \sin(\theta - \theta') \\ 0 & 1 & 0 \\ -\sin(\theta - \theta') & 0 & \cos(\theta - \theta') \end{pmatrix}. \tag{2.5}$$

The contributions of point displacement discontinuities to the stress tensor given by Eq. (2.4) can be integrated over $\mathcal{A}_k$ to yield the stress field from the k-th fracture

$$\boldsymbol{\sigma}^k(\mathbf{x}) = \int_{\mathcal{A}_k} \hat{\boldsymbol{\sigma}}^p(\mathbf{x}, \mathbf{x}') d\mathcal{A}'_k. \tag{2.6}$$

The total stress tensor at any point is a superposition of the stress fields produced by all fractures and the geological stress field $\boldsymbol{\sigma}^g$, and is written as

$$\boldsymbol{\sigma} = \sum_{k=1}^{N} \boldsymbol{\sigma}^k + \boldsymbol{\sigma}^g. \tag{2.7}$$

The total stress field must satisfy the traction boundary conditions along fracture surfaces. The normal component of traction in the k_{th} fracture is equated with the fluid pressure, and the shear component is set to zero since the fluid is unable to sustain shear stress. These two conditions lead to

$$\boldsymbol{\sigma} \cdot \mathbf{n}^k = -p_k \mathbf{n}^k, \quad \mathbf{x} \in \mathcal{A}_k, \quad k = 1 \dots N_f. \tag{2.8}$$

It is worth mentioning that while (2.8) is written in terms of stress components, it is actually a function of the displacement discontinuities as detailed in Appendix A.

The assumptions that lead to the vertical crack configuration and the applied stress field render the shear component of displacement discontinuity in the vertical direction, D_2, irrelevant. For this reason, only the components of stress $\boldsymbol{\sigma}$ that correspond to directions x_1 and x_3 are considered. It is convenient to denote the relevant components of the displacement discontinuity vector D_1 and D_3 respectively

by D_s and D_n. Similarly, the relevant total stress components σ_{13} and σ_{33} are denoted by σ_s and σ_n.

Flux balance and lubrication equation. Hydraulic fractures are driven by fluid injected from a wellbore. Figure 2 shows N vertical hydraulic fractures emanating from the same wellbore. The injection rate Q_0 represents the total fluid flux that is distributed among the fractures, such that

$$\sum_{k=1}^{N} Q_k = Q_0, \tag{2.9}$$

where Q_k is the fluid flux into the k_{th} fracture. Fluid pressure p_0 inside the wellbore is considered constant throughout the pipe's length (i.e., viscous friction in the pipe is ignored). The fluid pressure experiences a drop by the amount of $\Delta p_{k,\text{perf}}$ upon entering the k_{th} fracture as a result of the perforation friction. Thus for the kth fracture, the pressure equilibrium at the wellbore requires that

$$p_k\Big|_{\text{wellbore}} + \Delta p_{k,\text{perf}} = p_0, \quad k = 1 \dots N_f, \tag{2.10}$$

where $p_k\Big|_{\text{wellbore}}$ is the value of the fluid pressure at the location where the wellbore intersects the k_{th} fracture surface. For the case of n perforation holes for the kth port of entry, the pressure drop can be found from the following expression (Cramer, 1987; Crump and Conway, 1988)

$$\Delta p_{k,\text{perf}} = \frac{8\rho Q_k^2}{\pi^2 C_{d,k}^2 d_k^4 n^2}, \tag{2.11}$$

where ρ is the density of the fluid, $C_{d,k}$ is the dimensionless discharge coefficient for the k_{th} perforation cluster that represents the effect of the perforation shape on the pressure drop (Lord, 1994; Romero et al., 1995; El-Rabaa et al., 1997), while d_k is

the corresponding perforation diameter.

Fluid balance inside the k_{th} fracture is formulated in terms of the previously defined fracture opening w_k. To account for the fracture curvature, the fluid flux due to pressure gradient is written in terms of the coordinate system $(\tilde{x}, \tilde{y})$; therefore $\nabla = (\frac{\partial}{\partial \tilde{x}}, \frac{\partial}{\partial \tilde{y}})$ denotes the surface gradient in the balance of fluid, which is written as

$$\frac{\partial w_k}{\partial t} + \nabla \cdot \mathbf{q}_k + q_k^{\text{leak-off}}(\tilde{x}, \tilde{y}, t) = Q_k(t)\delta(\tilde{x}, \tilde{y}), \quad (\tilde{x}, \tilde{y}) \in \mathcal{A}_k, \quad k = 1 \dots N_f, \quad (2.12)$$

where $\mathbf{q}_k$ is the two-dimensional fluid flux inside the k_{th} fracture, $q_k^{\text{leak-off}}$ is the fluid leak-off from the k_{th} fracture into permeable rock, and the right-hand side represents the fluid flux coming from the wellbore into the k_{th} fracture. Following Carter's model (Carter, 1957), the fluid leak-off term can be written as

$$q_k^{\text{leak-off}}(\tilde{x}, \tilde{y}, t) = \begin{cases} \frac{C'}{\sqrt{t - t_{0,k}(\tilde{x}, \tilde{y})}}, & t \geq t_{0,k}(\tilde{x}, \tilde{y}), \\ 0, & t < t_{0,k}(\tilde{x}, \tilde{y}), \end{cases}, \quad k = 1 \dots N_f, \quad (2.13)$$

where $t_{0,k}(\tilde{x}, \tilde{y})$ is the time at which the fracture front was located at $(\tilde{x}, \tilde{y})$.

The fracture opening is significantly smaller than all other fracture dimensions. This allows the application of the lubrication approximation to the thin laminar flow inside the fracture, so that the flux obeys Poiseuille's law

$$\mathbf{q}_k = -\frac{w_k^3}{\mu'} \nabla p_k, \quad k = 1 \dots N_f, \quad (2.14)$$

which, combined with the fluid balance Eq. (2.12), yields the Reynolds equation (or lubrication equation) for each fracture

$$\frac{\partial w_k}{\partial t} = \frac{1}{\mu'} \nabla \cdot \left(w_k^3 \nabla p_k \right) - q_k^{\text{leak-off}} + Q_k \delta(\tilde{x}, \tilde{y}), \quad (\tilde{x}, \tilde{y}) \in \mathcal{A}_k, \quad k = 1 \dots N_f. \quad (2.15)$$

The zero fluid lag assumption renders the lubrication equation applicable along all fracture surfaces. Recall that the effect of gravity is neglected.

Fracture propagation. The zero fluid lag problem is computationally difficult because the coalescence of the fluid front and the fracture front yields a free boundary problem with singular fluid pressure at the fracture front. However, it has been shown that in situations of vanishing fluid lag, it is more efficient to utilize the boundary condition for a zero-lag situation (Detournay and Peirce, 2014), in which the zero fluid pressure boundary condition of the finite lag case is replaced by a zero flux condition. In addition to the zero flux condition, the fracture opening and the shear displacement discontinuity in the immediate vicinity of the crack front corresponds to the asymptotic linear elastic fracture mechanics (LEFM) solution (Rice, 1968; Tada et al., 2000), which, in terms of the distance from the front s, can be written as

$$w = \sqrt{\frac{32}{\pi}} \frac{K_I}{E'} s^{1/2}, \quad s \to 0, \tag{2.16}$$

where K_I is the Mode I stress intensity factor, and

$$D_s = \sqrt{\frac{32}{\pi}} \frac{K_{II}}{E'} s^{1/2}, \quad s \to 0, \tag{2.17}$$

where K_{II} is the Mode II stress intensity factor. Here the relations between the width and shear DD in terms of the corresponding local values are $w \equiv D_3$ and $D_s \equiv D_1$. Note that for the vertical fractures and applied loading considered here the Mode III stress intensity factor is not relevant. For relatively brittle materials such as rock, it is assumed that the crack will extend according to one of the local symmetry criteria (Erdogan and Sih, 1963). To first order, these criteria, which assume the material is tension-weak, predict the same extension direction. The zero

Mode II stress intensity factor criterion demands that, as the crack extends, its front is characterized by a null Mode II stress intensity factor. The maximum hoop stress criterion dictates that the crack extends in the direction that is normal to the direction of the principal stress (parallel to the direction of zero shear stress) produced by the crack before its extension. For the sake of convenience in the simulation procedure, the present formulation uses the zero Mode II criterion to select the direction of the crack extension, and the position of the crack front is determined by setting the Mode I stress intensity factor of the extended crack equal to the fracture toughness. Thus write

$$K_I = K_{Ic}, \tag{2.18}$$

where this stress intensity factor corresponds to the new crack front, for which its Mode II factor is zero.

The above equations define the exact problem for a three-dimensional hydraulic fracture. Numerical solution of this problem requires a representation of each crack surface by a two-dimensional mesh. Prohibitive amounts of computational resources are therefore required to solve the 3D problem when it is used in hydraulic fracture simulators, whose goal is to search for optimal configurations. To address the challenge, in the next section, we develop a procedure that relies on approximations of the crack opening in the vertical dimension to reduce the dimensionality of the problem while maintaining a remarkable level of accuracy.

2.4 Reduced-order modeling

It has been established that the coupling and associated competition between various physical phenomena involved in hydraulic fracturing, including fluid viscosity, fracture toughness, and fluid leak-off, result in a complex multiscale behaviour (Detournay, 2004, 2016). Computational methods such as the finite element method

(FEM) (Chen, 2013; Salimzadeh and Khalili, 2015; Gordeliy et al., 2019), the displacement discontinuity method (Peirce and Detournay, 2008; Dontsov and Peirce, 2017), and the phase-field method (Mikelić et al., 2015; Chukwudozie et al., 2019) are capable of resolving the multiscale nature of the singularities along the crack front, but only if extremely fine meshes are used. This makes such methods computationally expensive and thus severely limits their use in design applications that require fast solutions and extensive exploration of the design parameter space.

The reduced-order modeling concept is based on the approximation of the original model's governing equations to reduce the number of variables to be computed. The method relies on additional assumptions such as radial symmetry or plane strain conditions and forgoes some information about the solution, but in return, it can offer a significant increase in computational efficiency. The choice of assumptions is critical to the accuracy of this method, due to strong limitations on the possible solutions imposed by the assumptions. In particular, it is important that model order reduction preserves the multiscale behavior, one of the deciding factors in the fracture evolution.

The early reduced-order models for hydraulic fracturing use the classical KGD, PKN, and P3D solutions to reduce the problem to one-dimensional (1D) along the crack length (Settari and Cleary, 1986; Palmer, 1983; Palmer and Carroll, 1983; Adachi et al., 2010). These models do not fully account for the multiscale behavior inherent to hydraulic fractures. This limitation has been addressed in subsequent studies (Adachi and Peirce, 2008; Weng, 1992; Dontsov and Peirce, 2015a, 2016a; Linkov and Markov, 2020; Skopintsev et al., 2020), in particular in the enhanced PKN (EPKN) and the enhanced P3D (EP3D) models (Dontsov and Peirce, 2015a, 2016a). It is worth mentioning that the EPKN and the EP3D models were formulated for a single hydraulic fracture.

Another approach to model order reduction comes from the asymptotic analysis of the solution near the tip. The pre-computed near-tip asymptotic solutions have been used to approximate the whole near-tip region of the finite crack (Peirce and Detournay, 2008; Gordeliy and Peirce, 2013; Dontsov and Peirce, 2017; Zia and Lecampion, 2020). This method does not change the dimensionality of the problem, but it considerably reduces the number of variables related to the near-tip solution along the perimeter of the crack. On a side note, the asymptotic solutions for the near-front region have been derived for different types of fluid rheology, such as Newtonian (Garagash et al., 2011; Dontsov and Peirce, 2015c), power-law (Dontsov and Kresse, 2018), Carreau (Moukhtari and Lecampion, 2018), and Herschel-Bulkley (Bessmertnykh and Dontsov, 2019). Because it is necessary to have such solutions readily available for computational purposes and storing them in computer memory may be undesired, the alternative was offered in the form of fast approximate solutions (Dontsov and Peirce, 2015c; Dontsov and Kresse, 2018; Bessmertnykh and Dontsov, 2019).

In this study, we develop a model order reduction technique for multiple non-planar hydraulic fractures, based on the approach undertaken in the EPKN and EP3D models. In addition, the crack near-tip region is approximated by the near-tip asymptotic solution. The developed models are validated against the implicit level set algorithm (ILSA) (Peirce and Detournay, 2008; Peirce and Bunger, 2015; Dontsov and Peirce, 2017), which is a displacement discontinuity-based hydraulic fracturing simulator capable of modeling multiple planar hydraulic fractures in isotropic elastic media. ILSA gradually changes the fracture front position, to capture the necessary multiscale behavior associated with the near-tip asymptotic solution, and numerically solves the unreduced governing equations of the full 3D problem.

3 Reduced-order model for multiple planar hydraulic fractures with constant height

3.1 Background

This chapter describes the reduced-order model for multiple planar hydraulic fractures with constant height. The geometry of the problem is illustrated in Fig. 4. The origins of the model under study are traced to one of the early classical models, called as Perkins-Kern-Nordgren (PKN) model (Perkins and Kern, 1961; Nordgren, 1972). The PKN model considers a vertically oriented planar hydraulic fracture with a constant height. The constant height idealization reflects the idea that the reservoir layer of constant height is surrounded by layers with much larger confining stress, preventing fractures from growing in the vertical direction. It is worth mentioning that, in the classical approach, the length of the fracture is assumed to be much larger than the height. As a consequence, the PKN model does not accurately represent fracture propagation at early times when the fracture length is less or comparable to the height of the reservoir layer. Due to relatively small computational costs, the PKN model is often used as a basis for constructing more sophisticated models, such as when multiple hydraulic fractures propagate simultaneously from a single wellbore or when a network of hydraulic and natural fractures is considered (Kresse et al., 2013; Wu et al., 2017).

It is known that the classical PKN model is unable to capture the effect of fracture toughness in the lateral direction. Two toughness-dependent pressure boundary conditions were proposed to address this limitation. The first one provides a value for the pressure that is based on the energy calculations (Sarvaramini and Garagash, 2015), and the second one utilizes the pressure value from the radial fracture propagating in the toughness dominated regime (Nolte, 1991). Recently, a non-local elasticity

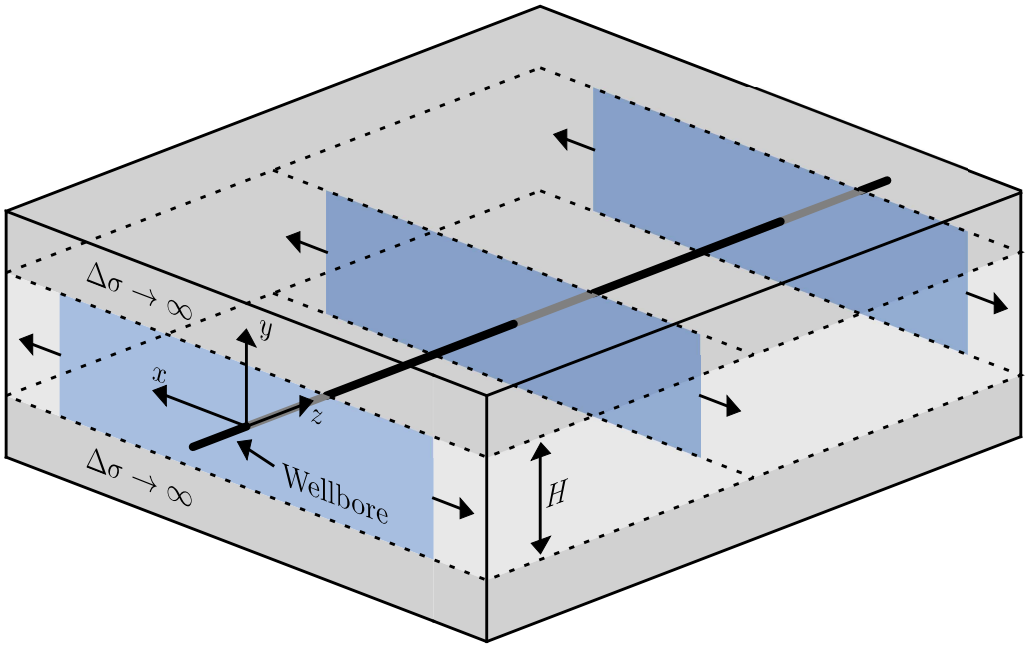

Figure 4: Problem geometry for blade-like or PKN type models.

approach was introduced in the enhanced PKN (EPKN) model (Dontsov and Peirce, 2016a), which replaces the plane strain limit of the elasticity integral with a more accurate approximation. The elliptic cross-section (as in the classical PKN model) is used to reduce the two-dimensional integral to a one-dimensional form by performing analytical integration in the fracture height direction. The fracture toughness is introduced through the toughness-dependent asymptotic solution at the fracture tip, which is used to advance the crack front. Another approach to account for the non-local elastic interactions is typically taken in the modeling of multiple hydraulic fractures and a fracture network problem (Olson, 2008; Kresse et al., 2013; Wu et al., 2017). These studies employ the two-dimensional displacement discontinuity method (2D DDM), which uses pressure-width relation that is based on the plane strain elasticity integral but utilizes the correction factor that accounts for a finite fracture height.

The developed model introduces several important modifications to the single crack EPKN formulation (Dontsov and Peirce, 2016a). First, the modeling of multiple

cracks involves a fixed mesh algorithm, instead of the moving mesh. Second, the method extends the non-local elasticity relation to the stress tensor's normal and shear components not restricted to the fracture plane. These modifications are aimed at accurate evaluation of the physical processes related to elasticity, fracture toughness, and fluid viscosity, which are typically most difficult to model together. Leak-off is omitted for simplicity because it does not influence the aforementioned processes. However, the algorithm can be easily modified to account for leak-off, as shown in Chapter 4.

The accuracy of the developed model is compared to other reduced models for a single blade-like or PKN hydraulic fracture, with the emphasis on evaluating different approaches to non-local elasticity, including the EPKN and the 2D DDM. The results obtained with the developed model for multiple cracks are validated against the implicit level set algorithm (ILSA) (Peirce and Detournay, 2008; Dontsov and Peirce, 2017). The latter is a fully coupled hydraulic fracturing simulator for multiple planar hydraulic fractures, which solves the governing equations related to the full 3D problem. In particular, we investigate the influence of the fracture spacing and height on the accuracy of the solution for a case of five simultaneously propagating planar hydraulic fractures with constant height. The results presented in this chapter are published in (Protasov and Donstov., 2017; Protasov et al., 2018).

3.2 Governing equations

This section is organized as follows. We start by outlining the EPKN model's main feature related to plane strain approximation. Then, derivation of the approximate stress tensor is performed, in which both normal and shear components are considered. Next come the governing equations of the reduced-order model for multiple cracks, which will henceforth be referred to as mEPKN. Finally, derivation of the approximate

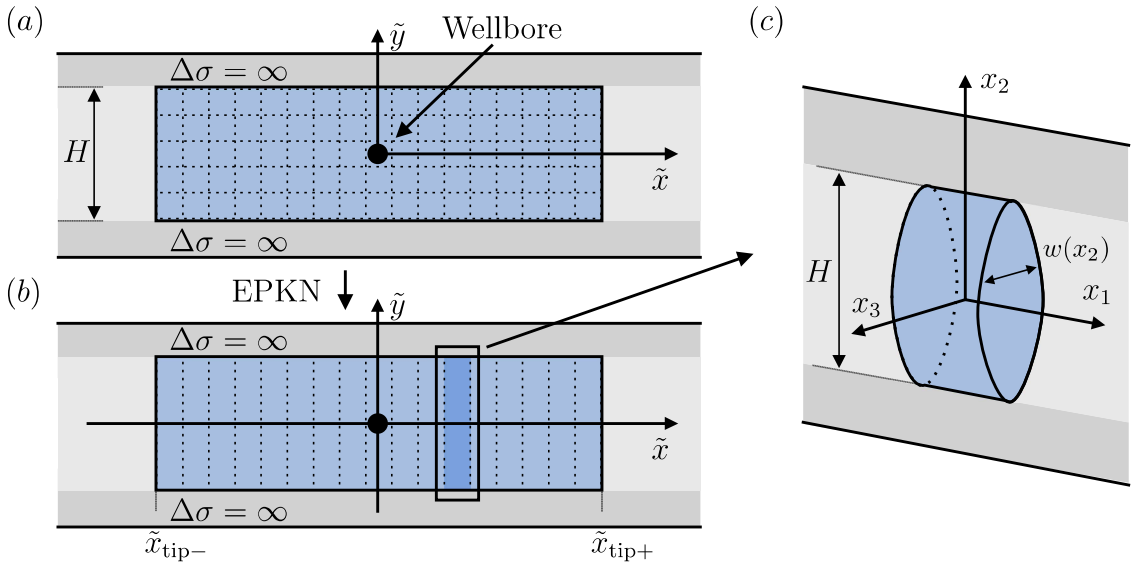

Figure 5: (a) 2D mesh over the fracture surface used in DDM. (b) 1D mesh used in EPKN method. (c) EPKN mesh element representing a fracture cross-section, following the plane strain solution in Eq. (3.1).

lubrication equation is presented, and followed by the propagation criteria for the lateral fracture fronts.

3.2.1 Model order reduction

In this section, we implement model order reduction, based on the EPKN approximation (Dontsov and Peirce, 2016a), to the problem of multiple hydraulic fractures formulated in Chapter 2. Additionally, the following assumptions are imposed: planar fracture growth, constant fracture height, and zero leak-off. First, we introduce the approximation procedure of the EPKN method (Dontsov and Peirce, 2016a).

Fracture opening and approximation procedure. Consider a vertical hydraulic fracture propagating in the reservoir layer of height H between stress layers with much larger confining stress, as illustrated in Fig. 5a. The fracture height is constant and equal to H, and the lateral fracture front is flat. The lateral and the vertical coordinates in the fracture plane with the origin at the wellbore are denoted by $\tilde{x}$ and $\tilde{y}$,

respectively. Figure 5a also shows a two-dimensional numerical mesh arising in the DDM approach. Instead of 2D mesh, the EPKN based model order reduction employs a one-dimensional mesh along the fracture length, as depicted in Fig. 5b. Here, $\tilde{x}_{\text{tip}+}$ and $\tilde{x}_{\text{tip}-}$ represent the coordinates of the lateral fronts. Because the fracture length is assumed to be much longer than the height, the fracture opening can be approximated by the plane strain solution, and the vertical fluid flow is negligible. The EPKN mesh element, approximated by the plane strain solution, is shown in Fig. 5c, where, in addition, the local coordinate system of the mesh element x_1, x_2, x_3 is introduced for convenience. In particular, the relation between stress and displacements is given in the local coordinate system.

Solution for the fracture opening under plane strain condition can be written as

$$w_{\text{ps}}(\tilde{y}) = \sqrt{\frac{8H}{\pi}} \frac{K_I}{E'} \sqrt{1 - \left(\frac{2\tilde{y}}{H}\right)^2}, \tag{3.1}$$

where K_I is the stress intensity factor at the vertical fracture tip. The model order reduction is based on the vertical averaging of functions that depend on $\tilde{y}$ by the following expression

$$\bar{f}(\tilde{x}) = \frac{1}{H} \int_{-H/2}^{H/2} f\left(\tilde{x}, \tilde{y}\right) \, d\tilde{y}, \tag{3.2}$$

where $\bar{f}$ is referred to as the average or the effective function. The plane strain solution given by Eq. (3.1) is the main approximation used in the EPKN model. Together with the averaging procedure given by Eq. (3.2), these expressions allow to formulate the problem in terms of the average fracture opening $\bar{w}$, such that

$$w_k(\tilde{x}, \tilde{y}) = \frac{4}{\pi} \bar{w}(\tilde{x}) \sqrt{1 - \left(\frac{2\tilde{y}}{H}\right)^2}, \tag{3.3}$$

where $\bar{w}$ depends only on the lateral coordinate $\tilde{x}$.

Approximate elasticity relation. Here we describe the procedure for the approximate calculation of stress, which follows the approach to non-local elasticity used in the EPKN model (Dontsov and Peirce, 2016a), and provides the elasticity relation for multiple interacting fractures.

In the EPKN model, the normal component of displacement discontinuity vector has the elliptical shape, according to (3.1). For the shear component, the relation between the shear displacement discontinuity and the shear stress in the limit of plane strain can be obtained by taking the corresponding limit of the elasticity equation (2.6) (see also Eq. (A.1) in Appendix A), which results in

$$\sigma_{13} - \sigma_{13}^g = -\frac{E}{2(1+\nu)} \frac{1}{4\pi} \int_{-H/2}^{H/2} \frac{D_1(x_2')dx_2'}{(x_2 - x_2')^2}. \tag{3.4}$$

Since the integral's kernel is identical to that for the normal stress expressed in terms of normal DD, then the application of a constant shear stress field leads to an elliptical shape of shear displacement discontinuity $D_1(x_2')$ along x_2, see for example (Adachi et al., 2010; Tada et al., 2000).

To summarize, the displacement discontinuity has the following expression in the EPKN model in terms of the local coordinates x_1, x_2, x_3

$$D_i(x_1, x_2) = \tilde{D}_i(x_1)\sqrt{1 - 4x_2^2/H^2}, \tag{3.5}$$

where $\tilde{D}_i$ denotes the maximum value of D_i at a cross-section. Here $D_3 \equiv w$ represents fracture opening, while $D_1 \equiv D_s$ corresponds to shear in the (x, z) plane. Another shear component D_2 is neglected.

The expression given by Eq. (3.5) is used to calculate stress given by Eq. (2.6). For convenience, we provide the expression for stress potential for a single fracture

element of length Δx_1 and height H as

$$\phi_i = \int_{-\Delta x_1/2}^{\Delta x_1/2} \int_{-H/2}^{H/2} \frac{\tilde{D}_i(x_1)\sqrt{1-4x_2^2/H^2}}{\sqrt{(x_1-x_1')^2+x_2'^2+x_3^2}}\, dx_2' dx_1', \quad i=1,2,3. \tag{3.6}$$

The latter expression can be analytically integrated over the height direction, resulting in

$$\phi_i = \int_{-\Delta x_1/2}^{\Delta x_1/2} \tilde{D}_i(x_1) I(x_1, x_2, x_3, x_1', H)\, dx_1', \tag{3.7}$$

where the exact expression for the function I is given in the Appendix B. It is worth mentioning that Eq. (3.7) requires one-dimensional numerical integration, while the equivalent integral for the fully 3D model is two-dimensional. This allows to significantly reduce computational costs. Once the potential is computed, all stress components can be evaluated, see Appendix A.

The traction boundary conditions (2.8) are slightly modified in the reduced-order model. Specifically, only a single point along the vertical direction at $\tilde{y} = 0$ takes part in the calculations, resulting in

$$\boldsymbol{\sigma}(\tilde{x}, \tilde{y}=0)\cdot \mathbf{n}(\tilde{x}) = -p_k(\tilde{x})\mathbf{n}(\tilde{x}), \qquad \tilde{x} \in \mathcal{A}_k, \quad k = 1 \dots N_f. \tag{3.8}$$

Such boundary conditions ensure continuity of the normal stress between fluid and solid as well as reflect the fact that fluid cannot sustain shear stress.

Flux balance and approximate lubrication equation. The distribution of fluxes entering each fracture depends on the perforation friction and the total flux

Q_0, which, following Eq. (2.9) and (2.10) can be written as

$$\sum_{k=1}^{N_f} Q_k = Q_0 \tag{3.9}$$

$$\text{and} \quad p_k\Big|_{\tilde{x}=0,\tilde{y}=0} + \Delta p_{k,\text{perf}} = p_0, \quad k = 1 \dots N_f. \tag{3.10}$$

Since we consider the fractures propagating horizontally along their length ($\tilde{x}$-direction) and restricted from vertical growth ($\tilde{y}$-direction), the fluid flow can be calculated based on Poiseuille flow of a Newtonian fluid in an elliptic DDM element of the k_{th} fracture as

$$\bar{q}_k = -\frac{12\bar{w}_k^3}{\pi^2\mu'}\frac{\partial p_k}{\partial \tilde{x}}, \tag{3.11}$$

where p_k is the fluid pressure in the k_{th} fracture that varies only with respect to the lateral coordinate $\tilde{x}$ according to the assumptions stated earlier. This expression is obtained by substituting elliptical width profile (3.3) into (2.14) and performing integration (3.2) analytically. The fluid balance in each fracture (2.12) can be averaged using (3.2) to obtain

$$\frac{\partial \bar{w}_k(\tilde{x})}{\partial t} + \frac{\partial \bar{q}_k(\tilde{x})}{\partial \tilde{x}} = \frac{Q_k}{H}\delta(\tilde{x}), \tag{3.12}$$

where we consider zero leak-off case.

Fracture propagation. The constant fracture height assumption of the PKN type models represents the influence of stress barriers of significant magnitude on the fracture propagation. The confining stress inside the barriers is considered large enough to prevent the vertical fracture growth. Consequently, it is not necessary to consider a propagation criterion in the vertical direction.

The lateral fracture front propagates according to the LEFM asymptotics (2.16) and the propagation condition (2.18). The LEFM asymptotics is formulated in terms

of $\bar{w}(\tilde{x})$ as

$$w_k(\tilde{x}, \tilde{y}=0) = \frac{4}{\pi}\bar{w}_k(\tilde{x}) = \sqrt{\frac{32}{\pi}}\frac{K_I}{E'}(\tilde{x}_{\text{tip}+} - \tilde{x})^{1/2}, \quad \tilde{x} \to \tilde{x}_{\text{tip}+} \tag{3.13}$$

$$\text{and} \quad w_k(\tilde{x}, \tilde{y}=0) = \frac{4}{\pi}\bar{w}_k(\tilde{x}) = \sqrt{\frac{32}{\pi}}\frac{K_I}{E'}(\tilde{x} - \tilde{x}_{\text{tip}-})^{1/2}, \quad \tilde{x} \to \tilde{x}_{\text{tip}-}. \tag{3.14}$$

Since the planar fractures are considered in this chapter, the turn criterion stemming from (2.17) is irrelevant and therefore the propagation is governed by $K_I = K_{Ic}$.

3.2.2 Near-tip asymptote

Propagation is determined by the near-front behavior, which involves complex stress singularities produced by the interaction of the fluid with the cracked solid. Many computational models of hydraulic fracturing do not consider these singularities, and instead, adopt only the square root-singular stress field that arises in the linear elastic fracture mechanics theory of (dry) cracks. The importance of incorporating the correct near-front behavior of hydraulic fractures was highlighted in recent works (Peirce and Detournay, 2008; Detournay and Peirce, 2014; Dontsov and Peirce, 2017). Specifically, the presence of fluid introduces viscosity and fluid leak-off in the vicinity of the crack front. Here we ignore the effect of fluid lag. The general form of the singular behavior in the near-front region involves the competition between the processes related to viscous energy losses, energy expenditure on breaking the rock and fluid leak-off. Therefore, depending on the parameters of the problem, LEFM asymptotic solution (Eq. (2.16)) may be valid only extremely close to the front, see, e.g., (Garagash et al., 2011).

Capturing this multiscale behavior near the fracture front using standard computational methods requires a very fine discretization and is therefore computationally expensive. The practical way to overcome this mesh requirement is considered

in (Dontsov and Peirce, 2015c), in which the approximate solution for the near-front region that captures the effects of toughness, viscosity, and leak-off, is developed. This allows the numerical discretization to use a coarser mesh near the fracture front. Note that the fracture opening for the aforementioned multiscale asymptotics follows LEFM solution (2.16) and propagation condition, given by (2.18), in the vicinity of the crack front, but it also extends it to account for the effects of leak-off and viscosity. For completeness, the details of the multiscale near-front asymptotics are presented in Appendix C.

3.2.3 Outline of numerical algorithm

Next, we provide a brief description of the numerical algorithm used in the model for multiple blade-like fractures, from now on called "mEPKN". The discretization strategy follows the fixed mesh approach, described in Appendix D. The extensive details of the algorithm are provided in Appendix E. Each fracture is discretized into elements along $\tilde{x}$, as illustrated in Fig. 5b. The total number of mesh elements of all fractures is denoted by N. The height of each element is constant and denoted by H due to the stress barrier limitation in the PKN model. The position and orientation of each mesh element, except for the tip elements, are fixed. The tip elements can extend representing the lateral fracture propagation. At each time step, the extension is computed to satisfy the fracture propagation condition (3.14). To decrease the discretization error, the algorithm splits the tip element into two new elements once its length exceeds a predefined value. The split procedure is done in agreement with the near-tip asymptotic solution. This procedure is also detailed in Appendix E.

The effective fracture opening $\bar{w}$ is discretized in a piece-wise constant fashion over the numerical mesh, so that $\bar{\boldsymbol{w}} = (\bar{w}^1, \ldots, \bar{w}^N)$ is the vector of the effective element

width. The tractions at midpoint of each element are computed from the elasticity relation given in Appendix A and the elastic potential in Eq. (3.7) integrated over the surface of each mesh element, see Appendix B. The stress tensor is then computed, and the traction boundary conditions (3.8) are applied. The normal tractions at each element, expressed in terms of $\bar{\boldsymbol{w}}$, are combined into the array $\boldsymbol{p} = (p^1, \ldots, p^N)$.

Next, the vector $\boldsymbol{p}$ is substituted into the lubrication equation (3.12) to obtain fluxes. The temporal and spatial derivatives are discretized using the backward and the central finite difference, respectively. The global fluid balance in the wellbore allows to compute the fluxes Q_k from the fluid pressure p using (3.9) and (3.10). Finally, the near-tip asymptotic solution in Eq. (3.14) is used to compute the tip element length based on its effective width, thus determining positions of the lateral fronts $\tilde{x}^{(k)}_{\text{tip}+}$ and $\tilde{x}^{(k)}_{\text{tip}-}$.

3.3 Numerical results

3.3.1 Plane strain hydraulic fracture

In order to examine the accuracy of the numerical algorithm, the results are compared to the existing solutions for plane strain fracture geometry. It is, therefore, important to briefly outline the governing equations for the plane strain (or Khristianovic-Geertsma-de Klerk (KGD)) hydraulic fracture. The first one is the lubrication equation, which is written as

$$\frac{\partial w}{\partial t} + \frac{\partial q_{\tilde{x}}}{\partial \tilde{x}} = \frac{Q_0}{H}\delta(\tilde{x}), \qquad q_{\tilde{x}} = -\frac{w^3}{\mu'}\frac{\partial p}{\partial \tilde{x}}. \tag{3.15}$$

Here, the expression for the fluid flux has a different numerical coefficient from the PKN model, and $\bar{w} = w$. The KGD elasticity equation is derived under plane strain

conditions, yielding

$$p(\tilde{x}) = -\frac{E'}{4\pi} \int\limits_{\tilde{x}_{\text{tip}-}}^{\tilde{x}_{\text{tip}+}} \frac{w(\tilde{x}')}{(\tilde{x} - \tilde{x}')^2} \, \mathrm{d}\tilde{x}'. \tag{3.16}$$

The boundary condition for the plane strain problem are derived from the LEFM asymptotics (2.16) and the propagation condition (2.18).

The results of the developed reduced-order model based on the EPKN method were computed for the KGD geometry by setting the fracture height $H = 500$ m, while the largest length among all cases considered is less than 130 m. In addition, as was stated before, we assume no leak-off for simplicity at this point. Solution with leak-off is examined in Chapter 4.

In the absence of leak-off, as considered in this study, the solution depends on a single dimensionless parameter (Hu and Garagash, 2010)

$$K_m = \left(\frac{K'^4}{\mu' E'^3 Q_0} \right)^{1/4}. \tag{3.17}$$

This parameter has a meaning of the dimensionless fracture toughness and determines the regime of propagation. In the situation of no leak-off, there are two regimes, the toughness dominated regime (denoted by K) and the viscosity dominated regime (denoted by M). As shown in (Dontsov, 2017), $K_m \gtrsim 4.8$ corresponds to the K regime and $K_m \lesssim 0.7$ corresponds to the M regime.

The obtained results were validated against the reference KGD model (Dontsov, 2017) for various problem parameters. The comparison between the numerical solution (black lines) and the reference solution (red lines) (Dontsov, 2017) is shown in Fig. 6. Two parameters are kept the same in all computations: the fracture toughness $K_{Ic} = 3$ MPa·m$^{1/2}$ and the injection rate $Q_0/H = 10^{-3}$ m^2/s. The top panel corresponds to the toughness dominated (K) regime, for which $E = 10$ GPa, $\mu = 10^{-3}$ Pa·s, and, as a result, $K_m = 4.8$. The middle panel examines the solution for the $M-K$

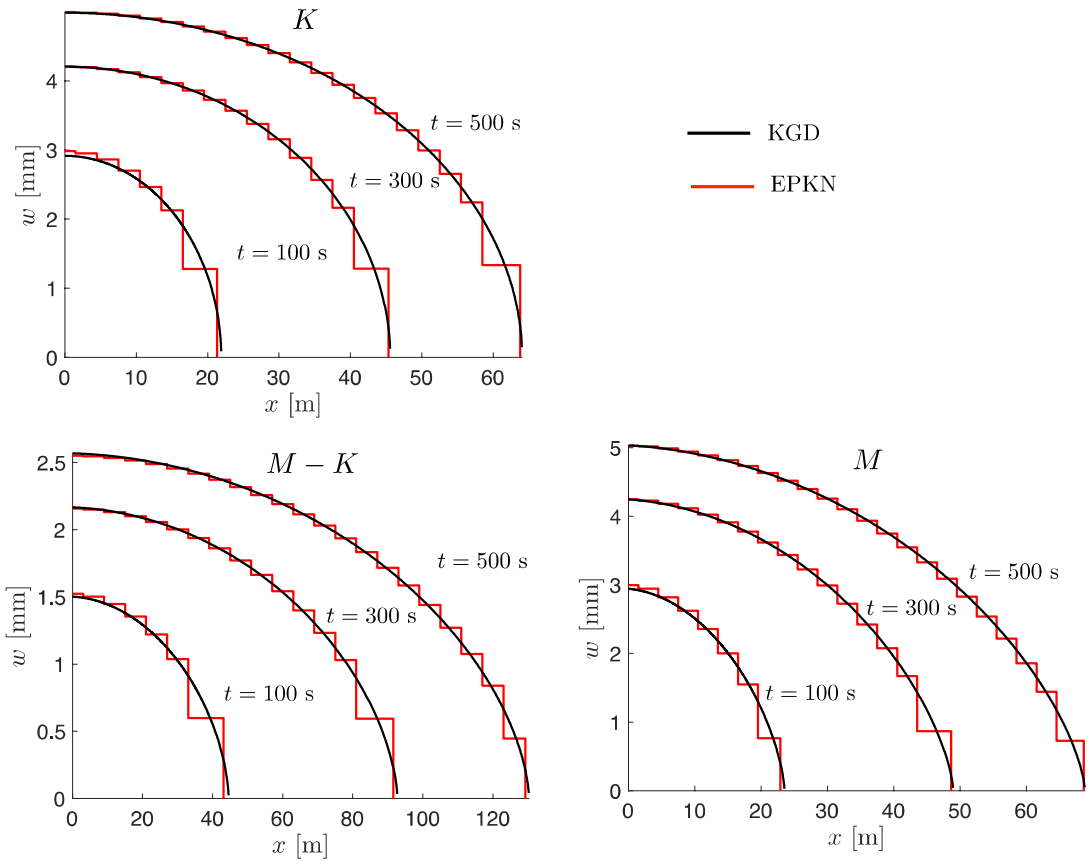

Figure 6: Comparison between the numerical solution (black lines) and the analytical solution (red lines) for the fracture width variation at different time instants for the K, $M-K$, and M regimes .

transition, for which $E = 35$ GPa, $\mu = 10^{-3}$ Pa·s, and, consequently, $K_m = 1.9$. The bottom panel compares the results for the viscosity dominated (M) regime, for which $E = 35$ GPa, $\mu = 10^{-1}$ Pa·s, and the corresponding dimensionless toughness is $K_m = 0.6$.

The numerical results show a good agreement with the reference solution for all regimes of propagation. In addition, the results corresponding to different time instants in Fig. 6 represent the effect of mesh discretization, because the propagation regime of the plane strain solution does not change with time and is self-similar. The numerical mesh has a different number of elements at early and later times. In particular, the $t = 100$ s solution corresponds to the course mesh, the $t = 300$ s represents a finer mesh, and the largest number of elements is used in the $t = 500$ s solution. Results in Fig. 6 verify the ability of the algorithm to accurately model the propagation condition (2.18) even on a coarse mesh, for which less than ten elements per fracture half-length is used to represent the solution.

3.3.2 Pressure estimation in models with non-local elasticity

There is also an alternative way to incorporate the non-local elasticity into the PKN model. The approach is based on the 2D displacement discontinuity method (2D DDM) (Kresse et al., 2013; Wu et al., 2017; Olson, 2008), in which the plane strain elasticity relation is used with height correction coefficients. To describe the method, we temporarily use x_i to denote the global coordinates x, y, z. The arising elasticity relation is often written in the discretized form as

$$p_i = C_{ij}^{2D} w_j, \qquad C_{ij}^{2D} = A_{ij} C_{ij}, \tag{3.18}$$

where C_{ij} are the plane strain influence coefficients

$$C_{ij} = -\frac{E'}{4\pi}\frac{\Delta x}{(x_i - x_j)^2 - \frac{\Delta x^2}{4}}, \tag{3.19}$$

and the height correction factor is given by

$$A_{ij} = 1 - \frac{|x_i - x_j|^\beta}{\left[(x_i - x_j)^2 + (H/\alpha)^2\right]^{\frac{\beta}{2}}}, \tag{3.20}$$

where $\alpha = 1$ and $\beta = 3.2$ are empirically derived constants. Two versions of this approach are implemented. In the first one, w_j represents the average width, i.e., $\bar{w}$. In the second version, w_j is taken to be the maximum width, i.e $w|_{z=0} = \frac{4}{\pi}\bar{w}$. Performance of both approaches is evaluated for completeness.

To better understand the difference between the EPKN and 2D DDM methods, this section compares the tractions produced by a single element with constant width. Fig. 7 plots the normalized pressure versus distance that is normalized by the element size a for different aspect ratios of $H/a = \{0.1, 1, 10\}$, where H is the fracture height. The origin is located in the middle of the fracture, and only $x > 0$ region is shown due to symmetry. The pressure due to the EPKN fracture is calculated using the approximate elasticity integral (3.6) and is shown by the solid black line. Two 2D DDM results are shown by the dashed and the dotted lines. In the first one, denoted by 2D DDM$-\bar{w}$, the averaged width $\bar{w}$ is used in (3.18). In the second one, denoted by 2D DDM$-w_{z=0}$, the maximum width $w|_{z=0} = \frac{4}{\pi}\bar{w}$ is substituted into (3.18).

First, let us approximate the whole PKN fracture by a single element, so that $a = 2l$, where l is the fracture half-length. Since the fracture length is much longer than the fracture height for the PKN model, then the result with $H/a = 0.1$ qualitatively represents the overall (average) pressure response. The pressure inside the fracture is substantially underestimated by both 2D DDM methods, which, as will be shown

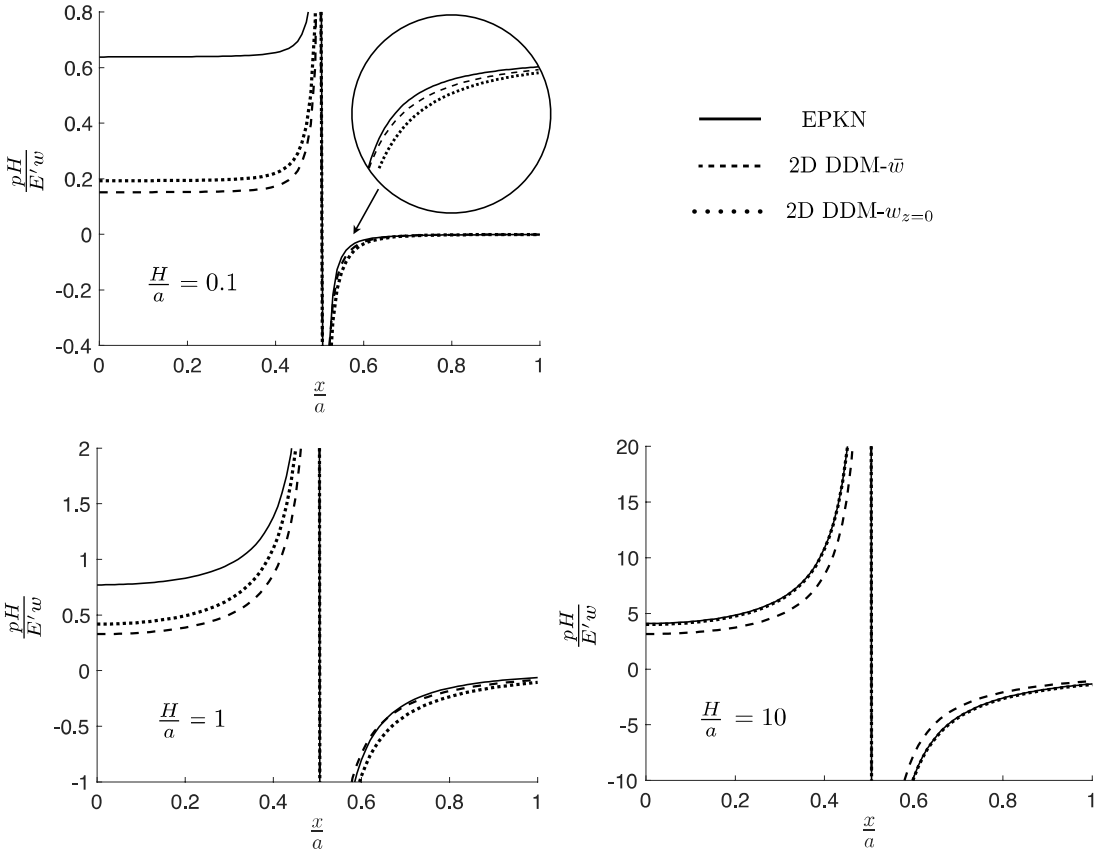

Figure 7: Pressure response from a single element for EPKN and 2D DDM numerical models for different ratios $H/a = \{0.1, 1, 10\}$, where H is fracture height and a is the element size.

later, translates into a smaller pressure for the corresponding PKN fractures. To investigate the mid-range elastic interactions, consider a fracture that consists of elements with the size $a = h$. The middle picture in Fig. 7 plots the pressure due to such an element. The self effect (i.e., $p(x = 0)$) is still underestimated by both 2D DDM models, and the elastic interaction between the elements at this length scale is also different from the EPKN model. This will lead to a different fracture shape and length predictions. The case $H/a = 10$ highlights the elastic interactions at a scale that is small compared to the fracture height, which is similar to a KGD fracture. As a result, the EPKN elastic integral (3.6) reduces to the KGD elasticity integral and the 2D DDM correction coefficients (3.20) reduce to unity, in which case the overall response is equivalent to the KGD model as well. Note that the maximum width should be used in the 2D DDM method to achieve a good match with the KGD solution.

Results in Fig. 7 demonstrate that the small scale elastic interactions incorporated into the EPKN and 2D DDM models are in a good agreement, but the mid-range and the long-range elastic interactions are substantially different. These qualitative observations will be verified in the next section, where the predictions of various PKN models will be compared to the reference solution.

In the next section, the non-local elasticity equation of the 2D DDM method is solved together with the lubrication equation in Eq. (3.12) and the boundary condition given by Eq. (2.18) to obtain the results for fracture propagation problem.

3.3.3 Single blade-like hydraulic fracture

This section evaluates the accuracy of different reduced-order models for blade-like of PKN hydraulic fracture. In particular, we show the results of the reduced-order models that utilize the classical PKN solution in its purest form, alongside the

more advanced methods, including the model under study. The reference solution is provided by ILSA. In addition, we include the previously published data in (Dontsov and Peirce, 2016a).

First, it is necessary to give a brief description of the reduced-order models in question. The classical PKN model uses the plane strain elasticity relation, written as

$$p(\tilde{x}) = \frac{2E'\bar{w}}{\pi H}, \tag{3.21}$$

which, when substituted into the lubrication equation in Eq. (3.12), results in

$$\frac{\partial \bar{w}}{\partial t} - \frac{6E'}{\pi^3 \mu' H}\frac{\partial^2 \bar{w}^4}{\partial \tilde{x}^2} = \frac{Q_0}{H}\delta(\tilde{x}), \tag{3.22}$$

where, for simplicity, we additionally assumed no leak-off. The corresponding boundary condition at the fracture tip is formulated for $\bar{w}$ or p through Eq. (3.21). In particular, the classical PKN model employs $\bar{w}=0$ at the tip, which does not account for the lateral fracture toughness. Different boundary conditions have been proposed to account for the fracture toughness, which can be written as

$$p_E\Big|_{\text{tip}} = \frac{2K_{Ic}}{\sqrt{\pi H}}, \qquad p_R\Big|_{\text{tip}} = \sqrt{\frac{\pi}{2H}}K_{Ic}, \tag{3.23}$$

where the first one is based on energy principles (Sarvaramini and Garagash, 2015), and the second one takes the pressure from an equivalent radial fracture with the diameter H (Nolte, 1991). These boundary conditions in Eq. (3.23) are rewritten in terms of $\bar{w}$ using Eq. (3.21), to yield

$$\bar{w}_E\Big|_{\text{tip}} = \frac{\sqrt{\pi H}K_{Ic}}{E'}, \qquad \bar{w}_R\Big|_{\text{tip}} = \Big(\frac{\pi}{2}\Big)^{3/2}\frac{\sqrt{H}K_{Ic}}{E'}. \tag{3.24}$$

In summary, the PKN model with local elasticity consists of solving the lubrication

equation given by Eq. (3.22) with either of the boundary conditions in Eq. (3.24) and (3.24).

Figures 8 and 9 compare the widths (at $y = 0$) and pressures variations for the following problem parameters: $K_{Ic} = \{0.47,\ 0.94,\ 1.57\}$ MPa$\cdot$ m$^{1/2}$ (different panels correspond to different values of fracture toughness), $E = 3.3$ GPa, $\nu = 0.4$, $Q_0 = 1.7$ mm^3/s, $H = 0.05$ m, and $\mu = 30.2$ Pa$\cdot$s. These parameters correspond to a laboratory experiment in (Jeffrey and Bunger, 2007). The Implicit Level Set Algorithm (ILSA) (see, e.g., (Peirce and Detournay, 2008)) is a fully planar hydraulic fracturing simulator and is therefore used in this study as the reference solution (shown by the solid grey lines). The "EPKN" (dashed black lines) represents the EPKN model for a single hydraulic fracture developed in (Dontsov and Peirce, 2016a), which implements the moving mesh technique and the curved lateral fracture tip. The "EPKN flat 1" (dotted black lines) refers to the same model, in which the curved fracture tip is replaced by the flat tip. The "EPKN flat 2" (solid red lines) represents the model under study that implements the fixed mesh approach required for modeling of multiple fractures. The "2D DDM$-\bar{w}$" (solid blue lines) denotes the 2D DDM model based on $\bar{w}$ described in Section 3.3.2, while the "2D DDM$-w|_{z=0}$" (solid green lines) refers to the $w|_{z=0} = \frac{4}{\pi}\bar{w}$ based 2D DDM model. Finally, the "PKN$-p_E$" (dashed red lines) and the "PKN$-p_R$" (dashed blue lines) represent the local elasticity models with pressure-based boundary conditions given by (3.24). It must be noted that the data for PKN$-p_E$ and PKN$-p_R$ models is adopted from (Dontsov and Peirce, 2016a).

As can be observed from Figs. 8 and 9, the "EPKN flat 1" and "EPKN flat 2" agree well between each other for all cases, which demonstrates that both algorithms (i.e., moving mesh and fixed mesh) provide consistently similar results. Because the EPKN model with curved lateral fracture tip matches the reference ILSA data for all cases, the curved fracture tip into the EPKN model. It is, therefore, important to

implement the curved fracture tip into the EPKN model. Both 2D DDM models are unable to provide accurate results and lead to the underestimation of fracture length by approximately 20%. The fluid pressure is substantially smaller than that for the reference solution. This agrees with previous observations in Fig. 7, where the single element self-effect pressure was several times smaller for the 2D DDM methods. The PKN$-p_E$ and PKN$-p_R$ models are able to estimate the overall fracture length and width while missing some details of the fracture width variation. The energy-based approach (PKN$-p_E$) provides estimates that are more accurate than the PKN$-p_R$ results. So, if a simple PKN model with local elasticity should be used, then the PKN$-p_E$ model is a more appropriate choice.

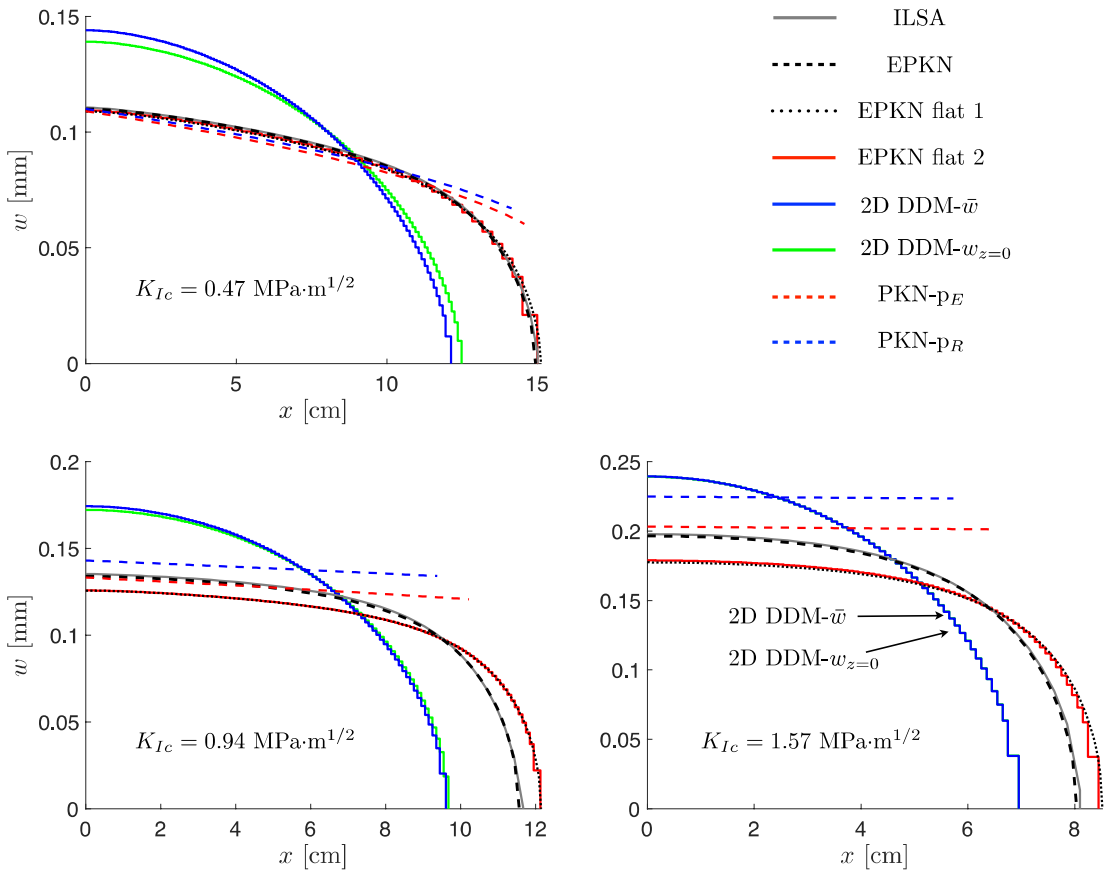

Figure 8: Comparison of different PKN models in terms of fracture width at $y=0$ for different values of fracture toughness.

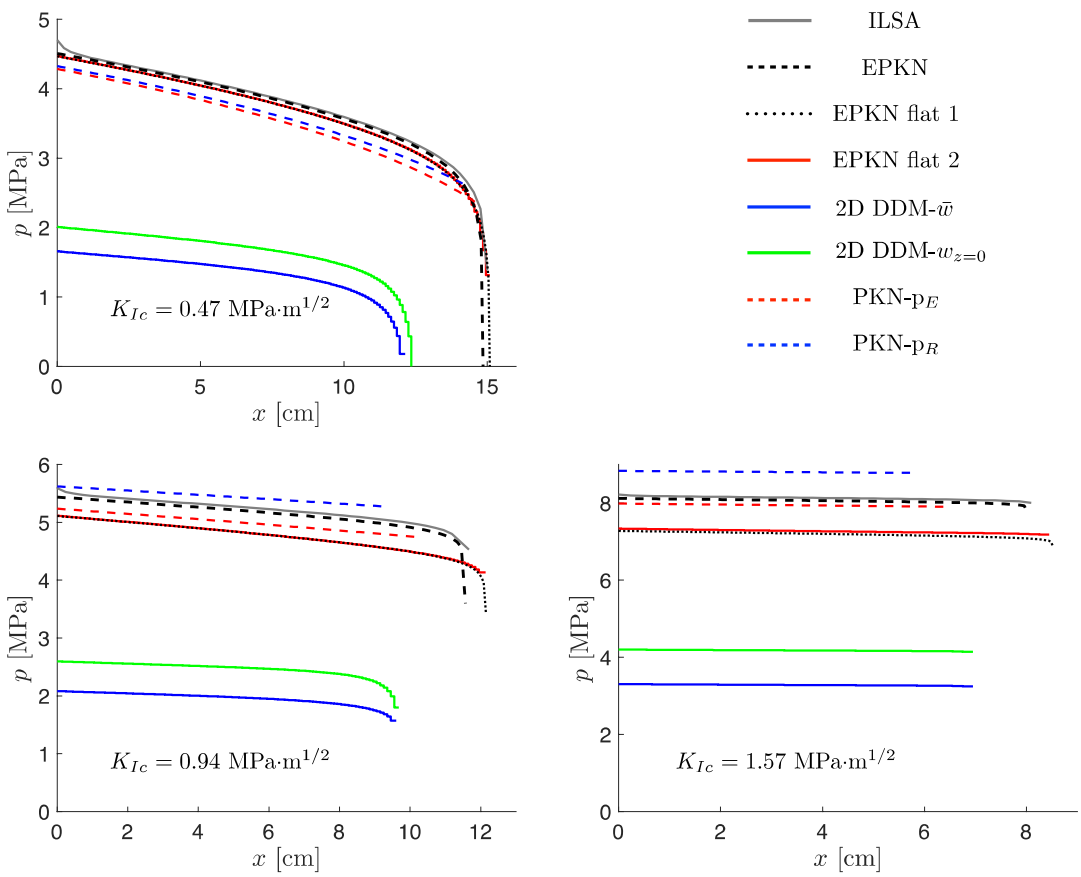

Figure 9: Comparison of different PKN models in terms of fluid pressure for different values of fracture toughness.

3.3.4 Multiple parallel blade-like hydraulic fractures

In this section, we present the results of the developed reduced-order model for multiple planar hydraulic fractures with constant height. The computed solution is compared to the reference solution obtained by ILSA for five equally spaced parallel hydraulic fractures.

The problem parameters in the simulation are the following: Young's modulus $E = 20$ GPa, Poisson's ratio $\nu = 0.2$, fracture toughness $K_{Ic} = 1.6$ MPa$\sqrt{\text{m}}$, fluid viscosity $\mu = 3 \cdot 10^{-3}$ Pa·s. In this simulation, we consider no fluid leak-off, but the mEPKN model is able to capture non-zero leak-off. Constant wellbore injection rate of $Q_0 = 0.03$ m^3/s is used, and the flux distribution between fractures depends on

the perforation friction. We present a series of simulations for different test cases without perforation friction and with large perforation friction. In addition, spacing S between fractures varied from 5 to 30 m. The fracture height is taken as 20 m in all cases.

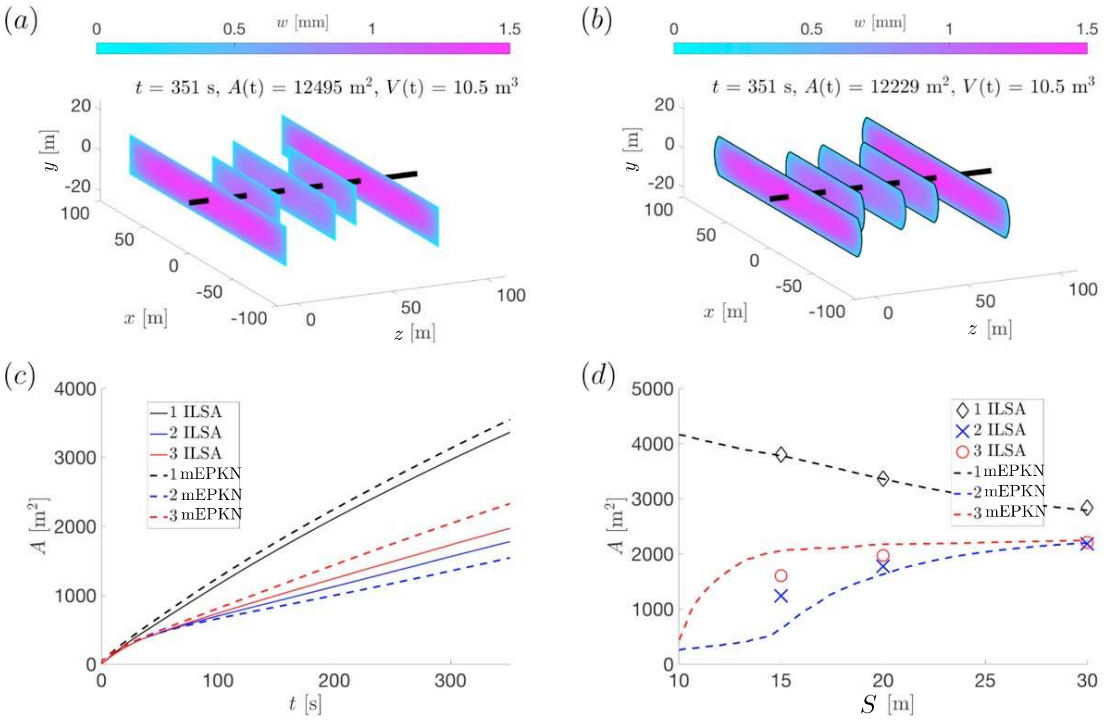

Figure 10: Numerical solution for five parallel constant height hydraulic fractures with low perforation friction. (a) mEPKN and (b) ILSA. (c) fracture surface area vs time for $S = 20$ m. (d) fracture surface area vs spacing at $t = 351$ s.

The results of the simulations for the case of no perforation friction are presented in Fig. 10. Figure 10a shows the final fracture geometry that is computed using the mEPKN model at time instant $t = 351$ s and for the spacing $S = 20$ m. The numerical solution can be visually compared to that obtained by ILSA in Fig. 10b. As can be seen from the figures, both solutions have similar behavior.

The black line around the fracture footprint in Fig. 10b denotes the exact position of the fracture front in ILSA. Because ILSA models 3D hydraulic fractures, the lateral fracture fronts are curved. In contrast, the mEPKN solution has flat lateral fronts,

which affects accuracy. It was shown that the inclusion of a curved fracture front increases the accuracy of the EPKN model (Dontsov and Peirce, 2016a).

The evolution of fracture surface area versus time is provided in Fig. 10c. The solutions of the mEPKN and ILSA are superimposed for comparison for spacing $S = 20$ m. The numbers in the legend denote fracture numbers starting from the outermost fracture at $z = 0$. Due to symmetry, fractures 5, 4 have the same properties as fractures 1, 2. Thus they are not present in the figure.

The dependence of the fracture surface area on spacing S between the fractures is given in Fig. 10d. Here, the results are compared at time instant $t = 351$ s. The ILSA results are shown by markers due to scarcity of the computed results, while mEPKN results are plotted by lines. This is dictated by the computational efficiency of the algorithms.

The discrepancy between the results in Fig. 10d for $S < 20$ m arises due to the inaccurate estimation of the fluid pressure at the injection points by the mEPKN model. In particular, the mEPKN model does not account for logarithmic pressure singularity at the injection point. Inaccurate calculation of fluid pressure leads to error in the fluid flux distribution, which, in turn, causes the discrepancy in the fracture area. Lower values of spacing correspond to the stronger interaction between fractures causing a larger error, while larger spacings have a low error. Even without accounting for the logarithmic pressure singularity at the injection points, the computationally efficient mEPKN model captures the behavior of the fracture propagation for the case of zero perforation friction.

The results of simulations for the case of large perforation friction (which leads to a uniform flux distribution) are presented in Fig. 11. Figures 11a and 11b show the fracture footprints for spacing $S = 20$ m computed with the mEPKN and ILSA, respectively. The evolution of fracture surface area versus time for spacing $S = 20$ m

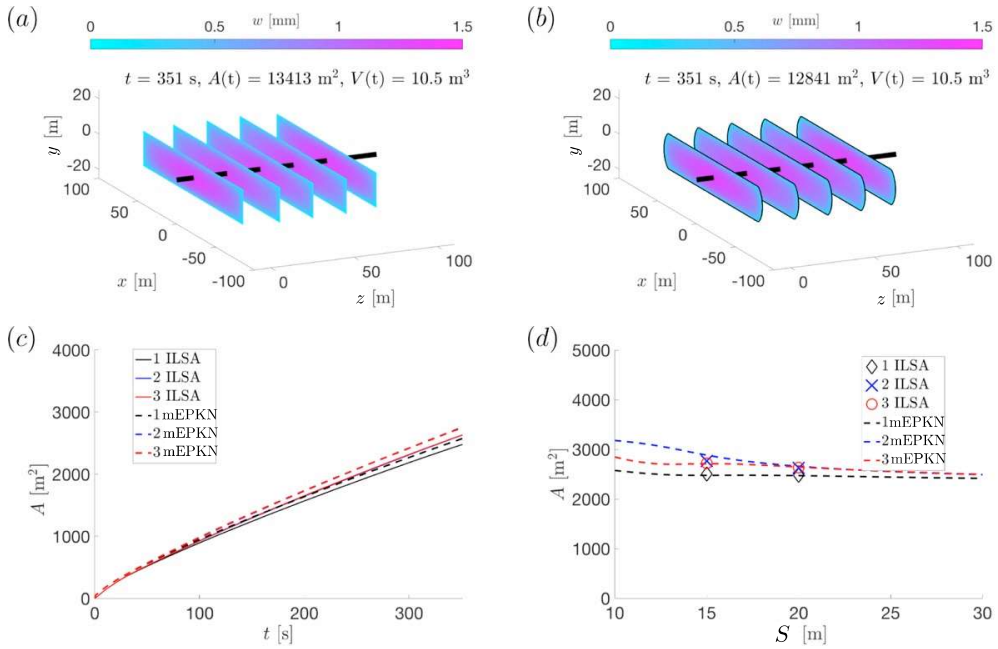

Figure 11: Numerical solution for five parallel constant height hydraulic fractures with limited entry. (a) mEPKN and (b) ILSA. (c) fracture surface area vs time for $S = 20$ m. (d) fracture surface area vs spacing at $t = 351$ s.

is shown in Fig. 11c, where the mEPKN and ILSA solutions are put together for comparison. The variation of fracture area versus spacing S is given in Fig. 11d for time instant $t = 351$ s. Large perforation friction results in a uniform flux distribution among the fractures and, given zero leak-off, all fractures have the same volume. However, the outer cracks exert additional pressure on the inner fractures, decreasing their fracture opening and increasing their surface area. The mEPKN model shows a good agreement with the reference solution for the case of large perforation friction, as can be seen from the evolution of the fracture surface area versus time in Fig. 11c. Variation of the fracture surface area versus spacing S, shown in Fig. 11d, indicates that the mEPKN agrees with the reference ILSA solution for the various spacings considered. The fact that the mEPKN model gives more accurate results for large perforation friction than zero perforation friction shows that the estimation of fluid pressure plays an important role in the flux distribution.

3.4 Summary

In this section, we presented the developed reduced-order model for multiple planar hydraulic fractures with constant height. The model is referred to as mEPKN. We chose to develop the model for multiple hydraulic fractures based on the EPKN model, after the analysis of several reduced-order models.

The EPKN model was originally implemented for a single symmetric fracture as an extension of the classical Perkins-Kern-Nordgren (PKN) model. To model multiple fractures, we implement several modifications to the EPKN model. First, the fixed mesh replaces the moving mesh, which is necessary for multiple fractures and allows further extension to non-planar configurations. Due to the fixed mesh approach, this study implements a different propagation algorithm from the one in the EPKN model. The second modification is related to the approximate elasticity equation that has to account for both normal and shear stress components as well as out-of-plane configurations. In addition, the developed algorithm utilizes the multiscale tip asymptotic solution, which relaxes the mesh size requirement.

We analyzed different approaches for reduced-order modeling that use the PKN model, including models with local elasticity and models with non-local elasticity. The PKN models with local elasticity utilize the pressure boundary condition, derived either from the energy analysis of the problem or from the equivalent radial fracture problem. Two PKN models with non-local elasticity are: i) enhanced PKN (EPKN) model, which uses the first-order approximation of the elasticity equation obtained by considering the plane strain limit of the problem; ii) 2D displacement discontinuity method (2D DDM), which derived the approximate elasticity equation by adding an empirically derived height correction factor to the plane strain elastic solution.

To evaluate the qualitative difference between the models, we compare pressure responses from a single fracture element (with constant width). The single element

pressure comparison between the EPKN and 2D DDM methods highlighted the differences in the pressure response, which is especially noticeable inside the element for long fractures, for which 2D DDM predicts smaller pressure values. Next, the accuracy of the models is determined by comparing the results with the reference solution for plane-strain and blade-like hydraulic fractures. This analysis showed great accuracy of the EPKN model in a single fracture case and its potential for modeling of multiple fractures.

Finally, the developed model is validated against the reference solution for a case of multiple parallel hydraulic fractures with constant height. In particular, we consider five uniformly spaced parallel fractures. We investigate the effect of perforation friction and spacing on the results. The mEPKN model agrees with the reference solution when the spacing between fractures is greater than the fracture height. A discrepancy in the flux distribution was observed for the zero perforation friction case, which happens due to inaccurate flux distribution. However, the mEPKN model still captures the qualitative behavior of the problem. The method for accurate calculation of flux distribution is introduced in the next chapter.

The reduced-order model for multiple planar hydraulic fractures with constant height, developed in this study, is a promising method for modeling complex fracture problems as it permits a generalization to multiple curved fractures, possess high computational efficiency, and is shown to have a reasonable accuracy for a wide set of problem parameters.

4 Reduced-order model for multiple non-planar hydraulic fractures

4.1 Background

This chapter presents the reduced-order model for multiple non-planar hydraulic fractures. Figure 12 shows the geometry of the problem. The model is based on the enhanced pseudo-3D (EP3D) model (Dontsov and Peirce, 2015a), which is, in turn, extends the classical pseudo-3D (P3D) solution. The P3D models consider vertically oriented hydraulic fractures propagating inside the reservoir layer, which is surrounded by layers with larger confining stress. The vertical fracture growth outside of the reservoir layer is limited because of the additional confining stress. The P3D solution allows the problem to be reduced to one-dimension, similar to the PKN models. At the same time, the P3D formulation differs from the PKN one in that the fracture height is not constant.

The classical solution has been extensively studied and applied in hydraulic fracture models (Settari and Cleary, 1986; Palmer, 1983; Palmer and Carroll, 1983; Adachi et al., 2010). However, due to the inability to fully characterize the effects associated with fluid viscosity and fracture toughness by using the classical P3D solution, several attempts have been made to improve it (Adachi and Peirce, 2008; Weng, 1992; Dontsov and Peirce, 2015a). To address the known drawbacks of the classical P3D model, the enhanced pseudo-3D model (EP3D) (Dontsov and Peirce, 2015a) introduces non-local elasticity interactions, a correction for viscous resistance in the vertical direction of the fracture, a curved crack front, and the near-front asymptotic solutions. It is shown that these modifications allow the accurate modeling of a single planar fracture under both viscosity-dominated and toughness-dominated conditions,

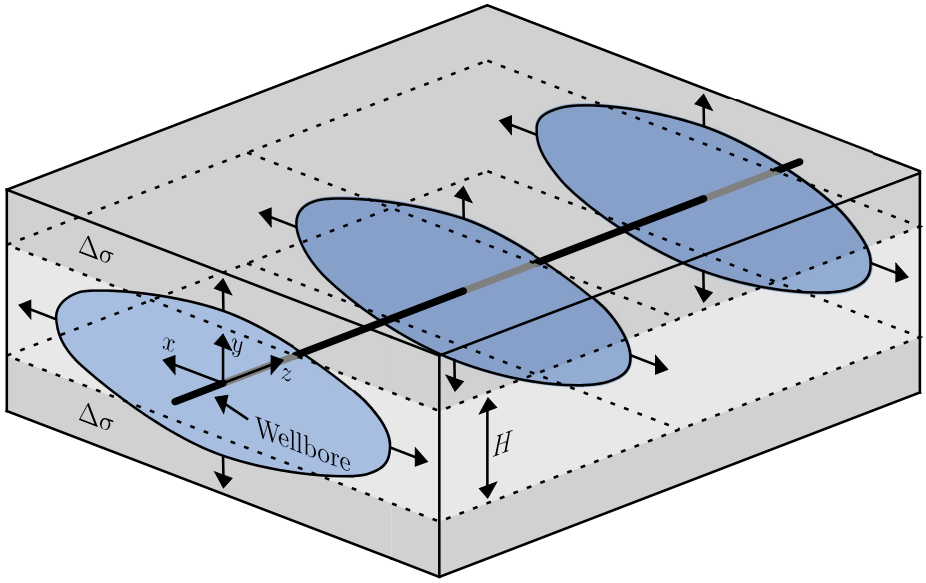

Figure 12: Problem geometry for P3D type models.

i.e., they capture the effects of fluid viscosity and toughness for the lateral and vertical growth. Further extension of the model to account for the effect of leak-off and coupling with proppant transport has been addressed in (Skopintsev et al., 2020) for the case of a planar fracture.

In extending the EP3D approach to the case of multiple non-planar hydraulic fractures, the formulation differs in many significant ways to the existing enhanced pseudo-3D formulation for a single fracture. First, it involves a fixed mesh instead of a moving mesh, similar to the reduced-order model based on the EPKN method presented in the previous chapter. Here, the numerical mesh is additionally modified to account for non-planar cracks and vertical crack growth. Second, the method employs the approximate non-local elasticity relation of the EPKN based model and combines it with the EP3D approach. Third, this work pioneers the use of tip asymptotic solutions for the problem of non-planar fractures. Finally, the formulation more accurately estimates the fluid pressure on the portions of the crack surfaces near the wellbore, which is especially important for computing the flux distribution between the fractures.

To evaluate the accuracy of the numerical algorithm, we compare the results with the analytical models for plane strain and radial fractures, and with a numerical reference model for a planar fracture. For the latter, we use the Implicit Level Set Algorithm (ILSA) (Peirce and Detournay, 2008; Dontsov and Peirce, 2017), which provides accurate solutions of three-dimensional configurations involving arbitrarily shaped planar fractures. The choice of the reference model was also driven by its mathematical formulation, which is similar to the EP3D model but, in contrast, solves the exact three-dimensional equations numerically while the EP3D model approximates them for faster computations.

4.2 Governing equations

To ensure completeness and to demonstrate that the model extension to multiple cracks involves significant challenges, we examine the necessary modifications to the EP3D model (Dontsov and Peirce, 2015a) in the following sections. It will become apparent that the extension requires careful treatment of the elastic interaction between the cracks, the pressure distribution in the fluid phase, and fluid leak-off phenomena.

This section is organized in the following order. We first outline the EP3D model's plane strain approximation. Next comes the application of the approximation procedure on the governing equations that leads to a reduced-order model for multiple cracks, which will henceforth be referred to as mEP3D. Then, derivation of the approximate stress tensor is performed, in which both normal and shear components are considered. Afterward, derivation of the approximate lubrication equation is presented, and followed by the propagation and crack-turning criteria for the vertical and the lateral fracture fronts. Finally, derivation of a more accurate value for the fluid pressure inside the fracture near the injection point is presented.

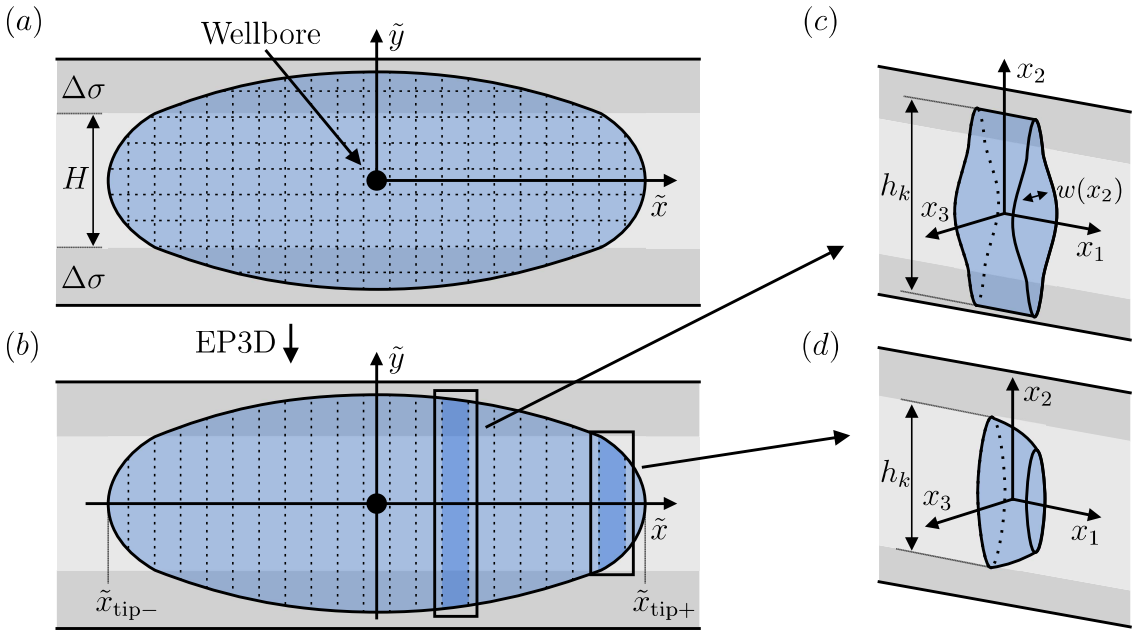

Figure 13: (a) 2D mesh over the fracture used in DDM. (b) 1D mesh used in EP3D method. (c)-(d) EP3D mesh element representing a fracture cross-section, following the plane strain (c) and the radial (d) solutions, see Eq. (4.1).

4.2.1 Model order reduction

This section applies the model order reduction based on the EP3D method to the problem of multiple hydraulic fractures formulated in Chapter 2. We start by describing the approximation procedure developed in the EP3D model (Dontsov and Peirce, 2015a).

Fracture opening and approximation procedure. Consider the k_{th} fracture in a rock formation with symmetric stress layers. It is convenient to represent the fracture in the planar view, whereby it is parametrized by the coordinates $\tilde{x}$ and $\tilde{y}$, where the former is the distance from the wellbore to the center of the mesh element and the latter is the vertical coordinate, as illustrated in Fig. 13a. The 2D mesh reflects typical discretization that is used for fully 3D numerical computations. The EP3D model reduces the discretization to 1D, as illustrated in Fig. 13b, where $\tilde{x}_{\text{tip}+}$

and $\tilde{x}_{\text{tip}-}$ denote the coordinates of the lateral fronts. The lack of discretization in the vertical direction is compensated by using an approximate analytical solution for the vertical cross-section, schematically shown in Fig. 13c, where $h_k(\tilde{x})$ is the height of its cross-section at $\tilde{x}$. Here, the local coordinate system x_1, x_2, x_3 is used in addition to the coordinates $\tilde{x}$ and $\tilde{y}$ for the computation of stress for curved fractures. These approximate expressions are derived from the plane strain solution under the assumption that $l_k \gg h_k(\tilde{x})$ for the vertical cross-sections far from the lateral front, and from the radial solution, for the ones close to the lateral front. Both analytical solutions correspond to a uniformly pressurized fracture and satisfy the toughness propagation criterion. It is also assumed that for any cross-section the fluid flux $\mathbf{q}_k$ is predominantly horizontal, and, consequently, that the fluid pressure p_k does not depend on the vertical coordinate, i.e., $q_{k,\tilde{y}} = 0$ and $p_k = p_k(\tilde{x})$.

While the fracture is growing in the middle layer and has not yet reached the stress barriers, the radial approximation is applied. After the crack has extended through the stress barriers, the opening of the vertical cross-section is approximated as that corresponding to a plane strain crack. Thus, for the k_{th} fracture, we have

$$w_k(\tilde{x}, \tilde{y}) = \begin{cases} w_{k,\text{radial}}(\tilde{x}, \tilde{y}), & h_k(\tilde{x}) \leq H, \\ w_{k,\text{plane strain}}(\tilde{x}, \tilde{y}), & h_k(\tilde{x}) > H. \end{cases} \tag{4.1}$$

The crack opening for a uniformly pressurized radial crack of diameter d can be written as

$$w_{\text{radial}}(\tilde{x}, \tilde{y}) = \frac{4K_I(\tilde{x})}{E'\sqrt{2\pi d}}\chi(\tilde{x}, \tilde{y}), \tag{4.2}$$

and for a plane strain fracture as

$$w_{\text{plane strain}}(\tilde{x},\tilde{y}) = \frac{4K_I(\tilde{x})}{E'\sqrt{2\pi h_k(\tilde{x})}}\chi(\tilde{x},\tilde{y}) + \frac{4\Delta\sigma}{\pi E'}\left[-\tilde{y}\ln\left|\frac{H\chi(\tilde{x},\tilde{y})+2\tilde{y}\psi(\tilde{x})}{H\chi(\tilde{x},\tilde{y})-2\tilde{y}\psi(\tilde{x})}\right| + \frac{H}{2}\ln\left|\frac{\chi(\tilde{x},\tilde{y})+\psi(\tilde{x})}{\chi(\tilde{x},\tilde{y})-\psi(\tilde{x})}\right|\right], \tag{4.3}$$

where $\chi(\tilde{x},\tilde{y}) = \sqrt{h_k(\tilde{x})^2 - 4\tilde{y}^2}$, $\psi(\tilde{x}) = \sqrt{h_k(\tilde{x})^2 - H^2}$, and $d = \sqrt{h_k(\tilde{x})^2 + 4\tilde{x}^2}$.

In addition to approximating the fracture opening by (4.1), the model order reduction utilizes the vertical averaging, which for an arbitrary function, f, is given by

$$\bar{f}(\tilde{x}) = \frac{1}{H}\int_{-h_k(\tilde{x})/2}^{h_k(\tilde{x})/2} f(\tilde{x},\tilde{y})\ d\tilde{y}. \tag{4.4}$$

The purpose of vertical averaging is to replace the vertical variation of any quantity by a single value. Note that the result is not strictly the average because it is normalized by H and not by $h_k(\tilde{x})$. First, the averaging procedure is applied to the approximate fracture opening given by (4.1). The expressions for the radial (4.2) and plane strain (4.3) solutions, averaged by (4.4), yield the following relations for the k_{th} fracture

$$\bar{w}_k(\tilde{x}) = \begin{cases} \dfrac{\pi K_I(\tilde{x})}{HE'\sqrt{2\pi d}}(h_k(\tilde{x}))^2, & h_k(\tilde{x}) \le H, \\ \dfrac{\pi K_I(\tilde{x})}{HE'\sqrt{2\pi h(\tilde{x})}}(h_k(\tilde{x}))^2 + \dfrac{\Delta\sigma}{E'}\sqrt{(h_k(\tilde{x}))^2 - H^2}, & h_k(\tilde{x}) > H, \end{cases} \tag{4.5}$$

which does not depend on the vertical coordinate $\tilde{y}$ and gives a direct relation between the height $h_k(\tilde{x})$ and the effective fracture opening $\bar{w}_k(\tilde{x})$.

Approximate elasticity relation. Next, we consider the elastic interaction between fractures. Specifically, the approximation of the elasticity relation (2.6) is

described. As was mentioned, the stress relations are considered in the local coordinate system x_1, x_2, x_3, shown in Fig. 2c, due to the curved fractures. Following the approach of EP3D, where the width is approximated by two ellipses for the purpose of elasticity computations, we extend this methodology for all DD components and for non-planar geometry. First, both the normal and the shear components must be considered in computations. Second, in contrast to the case of a single planar fracture for which stresses are computed only along the fracture plane, multiple fractures require computation of the stresses at generic locations in space x_1 and x_3 where the neighboring fractures are located. Note that we still take $x_2 = 0$ since we consider that all fractures propagate from the wellbore at the same vertical coordinate.

In order to compute the stresses, we employ a similar procedure as in (2.6), but extend it for the problem under consideration as discussed above. In particular, the following approximation is used for the displacement discontinuity vector, expressed in the local coordinate system,

$$D_i(x_1, x_2) \approx D_i^h(x_1)\sqrt{1 - 4x_2^2/h^2} + D_i^{h_{\Delta\sigma}}(x_1)\sqrt{1 - 4x_2^2/h_{\Delta\sigma}^2}, \tag{4.6}$$

where h is the fracture height at the considered point and $h_{\Delta\sigma}$, D_i^h, and $D_i^{h_{\Delta\sigma}}$ are defined below. The normal component and the shear components are considered separately. First, the term with D_3^h is matched with the elliptic part of the displacement discontinuity given by (4.1). Then, $D_3^{h_{\Delta\sigma}}$ and $h_{\Delta\sigma}$ are calculated to satisfy the following two conditions: the approximate expression with two ellipses yields the same effective cross-sectional area as (4.1), and in the plane strain limit, described in Appendix B, the solution matches the exact relation.

Because the shear confining stress is uniform in the EP3D model, the shear component of displacement discontinuity has the elliptic shape similar to the EPKN model, see Chapter 3 for details. Therefore, $D_{1,2}^{h_{\Delta\sigma}} = 0$ and $D_{1,2}(x_1, x_2) = D_{1,2}^h(x_1)\sqrt{1 - 4x_2^2/h^2}$.

The approximation for the displacement discontinuity vector is substituted into the elasticity integral in (2.6), where integration over the fracture surface can be separated into the integration over the fracture length and height. It is more convenient to consider the integration over a single fracture element in terms of the potential ϕ_i in the local coordinate system:

$$\phi_i = \int_{-\Delta x_1/2}^{\Delta x_1/2} \int_{-h(x_1')/2}^{h(x_1')/2} \frac{D_i}{\sqrt{(x_1 - x_1')^2 + x_2'^2 + x_3^2}} \, dx_2' dx_1', \quad i = 1, 2, 3. \tag{4.7}$$

By substituting (4.6) into (4.7) and performing integration analytically over the height direction, we have

$$\phi_i = \int_{-\Delta x_1/2}^{\Delta x_1/2} D_i^h(x_1) I(x_1, x_2, x_3, x_1', h) + D_i^{h_{\Delta\sigma}}(x_1) I(x_1, x_2, x_3, x_1', h_{\Delta\sigma}) \, dx_1', \tag{4.8}$$

where the exact expression for the function I is given in Appendix B. Note that the elasticity integral in (4.7) in the fully 3D model requires two-dimensional numerical integration, while the numerical integral in (4.8) after the EP3D model's reduction is one-dimensional.

The reduced model follows the stress boundary condition given by (2.8) of the full problem. However, only a single point along the vertical direction, $\tilde{y} = 0$, is considered, similar to the mEPKN model. However, because of the horizontal fluid flux assumption of the mEP3D model, the traction boundary condition is formulated in terms of the effective fluid pressure $\bar{p}_k(\tilde{x})$, which is defined in the next paragraph. The boundary condition is written as

$$\boldsymbol{\sigma}(\tilde{x}, \tilde{y} = 0) \cdot \mathbf{n}(\tilde{x}) = -\bar{p}_k(\tilde{x}) \mathbf{n}(\tilde{x}), \qquad \tilde{x} \in \mathcal{A}_k, \quad k = 1 \ldots N_f. \tag{4.9}$$

As will be explained in Section 4.2.3, is important to differentiate the local fluid pressure and the effective fluid pressure in the equation for the global fluid balance.

Flux balance and approximate lubrication equation. In the following discussion of the EP3D model, we refer to p as to the local pressure that can vary in both $\tilde{x}$ and $\tilde{y}$ directions, while $\bar{p}$ is the average pressure along the height direction. It should be noted that the effective pressure is approximately equal to the local pressure in the majority of the fracture due to the horizontal flux assumption. However, an exception occurs near the wellbore, where the point injection source is used. Therefore, the fluid flux distribution (2.9) and pressure equilibrium (2.10) are formulated in terms of the local pressure, yielding

$$\sum_{k=1}^{N_f} Q_k = Q_0, \tag{4.10}$$

$$\text{and} \quad p_k\Big|_{\tilde{x}=0,\tilde{y}=0} + \Delta p_{k,\text{perf}} = p_0, \qquad k = 1 \dots N_f. \tag{4.11}$$

A method to estimate the local pressure based on its effective counterpart is presented in Section 4.2.3.

The expression for the effective fluid flux based on the Poiseuille's law is given by

$$\bar{q}_k(\tilde{x}) = -\frac{1}{H\mu'} \int_{-h_k/2}^{h_k/2} \frac{\partial p_k(\tilde{x},\tilde{y})}{\partial \tilde{x}} w_k^3 \, d\tilde{y} \approx -\frac{1}{H\mu'} \frac{\partial \bar{p}_k(\tilde{x})}{\partial \tilde{x}} \int_{-h_k/2}^{h_k/2} w_k^3 \, d\tilde{y}, \tag{4.12}$$

which utilizes the average pressure $\bar{p}(\tilde{x})$ in the EP3D model. The integral on the right-hand side of (4.12) is calculated numerically.

The lubrication equation for the k_{th} fracture in Eq. (2.15) is reduced to one dimension by applying the vertical averaging given by Eq. (4.4) on Eq. (2.15), yielding

$$\frac{\partial \bar{w}_k(\tilde{x})}{\partial t} + \frac{\partial \bar{q}_k(\tilde{x})}{\partial \tilde{x}} + \frac{1}{H} \int_{-h_k/2}^{h_k/2} \frac{C'}{\sqrt{t - t_{0,k}(\tilde{x},\tilde{y})}} \, d\tilde{y} = \frac{Q_k}{H} \delta(\tilde{x}). \tag{4.13}$$

It is worth mentioning that the latter expression accounts for leak-off, in contrast to Eq. (3.12) in the mEPKN model.

Fracture propagation. The position of the vertical fracture front is determined by Eq. (4.5), which relates the height and the effective width. The effect of fluid viscosity on this relation is taken into account by modifying the propagation condition in the vertical direction

$$K_I = K_{Ic} + \Delta K_{Ic}^{\text{viscous}}, \tag{4.14}$$

where $\Delta K_{Ic}^{\text{viscous}}$ accounts for the viscous resistance on the fracture propagation, see the details in Appendix F. The lateral fracture front, however, uses the LEFM asymptotics given by Eq. (2.16) for the fracture opening at the tip, and the propagation condition in Eq. (2.18). It should be noted that, while the EP3D model is formulated in terms of the effective fracture opening $\bar{w}(\tilde{x})$, the LEFM asymptotics is applied to the fracture opening $w(\tilde{x}, \tilde{y})$ at $\tilde{y} = 0$, yielding

$$\begin{aligned} w_k(\tilde{x}, \tilde{y} = 0) &= \frac{4}{\pi}\bar{w}_k(\tilde{x}) = \sqrt{\frac{32}{\pi}}\frac{K_I}{E'}(\tilde{x}_{\text{tip}+} - \tilde{x})^{1/2}, \quad \tilde{x} \to \tilde{x}_{\text{tip}+}, \\ w_k(\tilde{x}, \tilde{y} = 0) &= \frac{4}{\pi}\bar{w}_k(\tilde{x}) = \sqrt{\frac{32}{\pi}}\frac{K_I}{E'}(\tilde{x} - \tilde{x}_{\text{tip}-})^{1/2}, \quad \tilde{x} \to \tilde{x}_{\text{tip}-}. \end{aligned} \tag{4.15}$$

The Mode II solution given by Eq. (2.17) and the local symmetry condition can be formulated as

$$D_s = 0, \quad \tilde{x} \to \tilde{x}_{\text{tip}+}, \text{ or } \tilde{x} \to \tilde{x}_{\text{tip}-}. \tag{4.16}$$

The direction of the lateral fracture front propagation is determined by the turning criteria in Eq. (4.16).

4.2.2 Near-tip asymptote and fracture turning

The motivation for using the near-tip asymptote in hydraulic fracture modeling was presented in Chapter 3. In the context of the original EP3D model (Dontsov and Peirce, 2015a), it used either LEFM or viscous asymptote depending on the problem parameters. Subsequently, the model was upgraded in (Dontsov and Peirce,

2015b) with the two-process asymptote that simultaneously captures the effects of toughness and viscosity, while neglecting leak-off. In contrast to the previous studies, in this paper, we utilize the complete crack-front asymptotes, in which all three primary physical mechanisms are included. The details of the multi-scale near-front asymptotics are presented in Appendix C.

4.2.3 Near-wellbore pressure correction

The EP3D model's lubrication equation is the reduced version of the full lubrication equation. The full equation corresponds to a two-dimensional fluid flow inside the fracture, while its reduced counterpart considers only the one-dimensional flow in the lateral direction. As a result of this reduction, the approximate pressure represents the effective cross-sectional pressure, which depends only on $\tilde{x}$ and is constant along $\tilde{y}$. This approximation is accurate throughout the fracture length as long as the pressure does not vary significantly along the vertical direction. However, the pressure stemming from the fully 2D solution is singular at the injection point (or wellbore). Panels (a) and (b) in Fig. 14 show schematics of the two-dimensional and the reduced one-dimensional problems, respectively. The fluid flux at the injection point (wellbore) has a vertical component, Fig. 14a, while the EP3D approach assumes a horizontal fluid flux, as shown in Fig. 14b. This leads to different pressure profiles for the 1D model's solution and the 2D model's solution (evaluated along $y = 0$), which are illustrated in Fig. 14c. The results shown are computed with the EP3D model for the 1D flow, and EP3D model with pressure correction accounting for the 2D flow, as discussed below. The problem parameters correspond to the M regime (see Table 3) for a single fracture at $t = 2000$ s. The 1D flow model underestimates the fluid pressure at the wellbore compared to the 2D flow model. At the same time, they agree further away from the source.

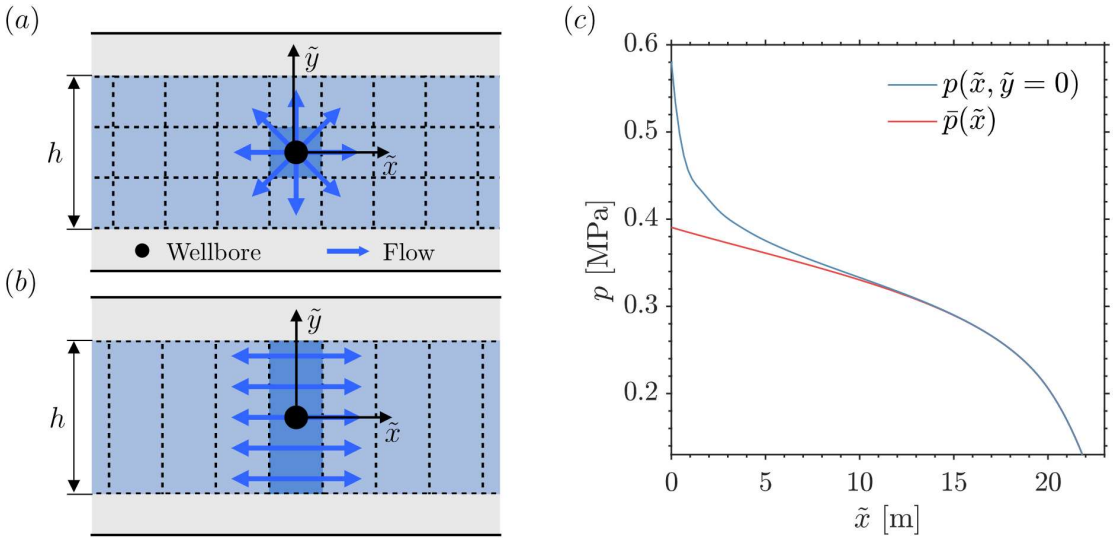

Figure 14: Scheme of the fluid flow inside a fracture. (a) Two-dimensional model (b) One-dimensional model used in P3D fracture. (c) The comparison of the effective pressure $\bar{p}$ and the local pressure $p(x)$ for the corresponding 1D and 2D flow problems where $\tilde{x} = 0$ is the position of the wellbore.

Next, we propose a solution to this problem by analyzing the 2D flow problem separately near the wellbore and far from the wellbore. In addition, since the near-wellbore behavior is under investigation, we focus only on the flux and the source terms in the lubrication Eq. (2.12), while neglecting the effects of leak-off and fracture width change.

With the reference to Fig. 14a and the assumptions outlined above, the problem under consideration can be formulated as

$$\nabla \cdot q(\tilde{x}, \tilde{y}) = Q\delta(\tilde{x}, \tilde{y}), \qquad q = -\frac{w^3}{\mu'}\nabla p, \tag{4.17}$$

which is subject to boundary conditions

$$q_{\tilde{y}}(\tilde{x}, \pm h/2) = -\frac{w^3}{\mu'}\frac{\partial p\,(\tilde{x}, \tilde{y})}{\partial \tilde{y}}\bigg|_{\tilde{y}=\pm h/2} = 0. \tag{4.18}$$

By integrating (4.17) in the vertical and horizontal directions, as well as using (4.18),

we can compute the effective flux as

$$\bar{q}_{\tilde{x}}(\tilde{x}) = \frac{1}{H}\int_{-h/2}^{h/2} q_{\tilde{x}}(\tilde{x},\tilde{y})\,dy = \frac{Q}{2H}, \tag{4.19}$$

which is constant along the $\tilde{x}$ axis. At the same time, assuming that w is constant, the above equations can be solved analytically using the method of images. Consequently, the flux along the central line ($\tilde{y}=0$) is given by

$$q_{\tilde{x}}(\tilde{x},0) = \frac{Q}{2h}\coth\left(\frac{\pi\tilde{x}}{h}\right). \tag{4.20}$$

The above expression asymptotically behaves as $\frac{Q}{2\pi\tilde{x}}$ near the wellbore and $\frac{Q}{2h}$ far away from the injection point. To incorporate the effect of variable fracture width, approximately, note that the far field behavior for the flux along the central line is given by

$$q_{\tilde{x}}(\tilde{x},0) = \frac{Q}{2H}\frac{w^3_{\tilde{y}=0}}{\overline{w^3}}, \qquad \tilde{x} \gg H. \tag{4.21}$$

Therefore, in order to correct for the width variation, we change (4.20) with

$$q_{\tilde{x}}(\tilde{x},0) = \frac{Q}{2H}\frac{w^3_{\tilde{y}=0}}{\overline{w^3}}\coth\left(\frac{\pi\tilde{x}}{H}\frac{w^3_{\tilde{y}=0}}{\overline{w^3}}\right). \tag{4.22}$$

This expression accurately captures both the near wellbore behavior, as well as the far field solution. Finally, by substituting the expression for the flux in terms of pressure into (4.19) and (4.22), we obtain

$$\frac{\partial\bar{p}}{\partial\tilde{x}} = \tanh\left(\frac{\pi\tilde{x}}{H}\frac{w^3_{\tilde{y}=0}}{\overline{w^3}}\right)\frac{\partial p_l(\tilde{x})}{\partial\tilde{x}}, \tag{4.23}$$

where $p_l(\tilde{x}) = p(\tilde{x},0)$ is denotes variation of the local pressure along the $\tilde{x}$ axis.

The EP3D model uses the radial crack solution to approximate segments of the

crack for which $h < H$. Since at the early time the whole crack follows the radial solution, here we compare the effective and the local pressures for the case of radial symmetry. The lubrication Eq. (4.17) can be solved assuming radial symmetry. The flux along the central line is

$$q_{\tilde{x}} = \frac{Q}{2\pi\tilde{x}}. \tag{4.24}$$

The effective flux at the vertical cross-section of height h corresponding to $\tilde{x}$ can be found by considering the flux through radial sector, yielding

$$\bar{q}_{\tilde{x}} = \frac{Q}{\pi H} \arctan\left(\frac{h}{2\tilde{x}}\right). \tag{4.25}$$

By following the same logic as before, Eq. (4.24) and (4.25) can be used to obtain the relation between the effective pressure and the local pressure as

$$\frac{\partial \bar{p}}{\partial \tilde{x}} = \frac{2x}{H} \frac{w^3_{\tilde{y}=0}}{\overline{w^3}} \arctan\left(\frac{h}{2x}\right) \frac{\partial p_l}{\partial \tilde{x}}. \tag{4.26}$$

This relation is similar to Eq. (4.23) near the injection point. However, far from the injection point this equation yields a different result.

The above Eq. (4.23) and (4.26) relate $p_l(\tilde{x})$ to $\bar{p}(\tilde{x})$ up to a constant. The constant can be determined by considering $p(\tilde{x}, 0)$ and $\bar{p}(\tilde{x})$ near the lateral crack front, where the fluid flux is mostly horizontal, and the difference between the local and the effective pressure vanishes. However, on the basis of the zero fluid lag assumption, the numerical algorithm equates the effective fluid pressure to the normal component of elastic stress tensor throughout the crack surface up to the tip. The stress tensor at the crack tip is known to be singular. Due to this singularity, the numerical error in the effective fluid pressure near the tip is large. Particularly, a small variation in the size of the tip mesh element affects the tip element's effective pressure. Alternatively, the local pressure can be estimated by considering the average characteristic

of the local pressure and the effective pressure. The elasticity relation based on the approximate potential in Eq. (4.8) can be inverted and integrated to obtain the integral condition on the effective pressure based on the crack volume. Recall that the approximate potential considers constant pressure at each vertical cross-section. While not an exact analysis of the local pressure, the inverted elasticity relation can be applied to the local pressure to estimate the crack volume. This method provides a robust approach for the local pressure estimation since it is stable with respect to mesh variations. The numerical solution shows that when the crack volume condition is applied to Eq. (4.23) and (4.26), both result in very similar flux distributions. This happens because both equations yield the correct singularity of pressure at the injection point, and the crack volume condition ensures equal average values.

4.2.4 Outline of numerical algorithm

In this section, we provide a brief description of the numerical algorithm, leaving the details to Appendix G. The algorithm is similar to the one used in the mEPKN model in Chapter 3 and involves the fixed mesh approach, which is detailed in Appendix D. The fracture is divided into multiple elements along its length ($\tilde{x}$-direction) as shown in the discretization scheme in Fig. 13b. The position and orientation of each mesh element, except for the tip elements, are fixed. At each time step, the tip elements extend to satisfy the fracture propagation condition given by Eq. (3.14). The tip element is split into two when its length grows past the control value. However, the procedure differs from the one in the mEPKN model. To account for non-planar fractures considered in the mEP3D model, the variable direction of the tip elements represents fracture curving according to the turn criteria given (4.16). In contrast to the mEPKN model, the height of each element is not constant and depends on

the stress barrier magnitude and the effective width through the approximate relation (4.5).

The effective fracture opening $\bar{w}$ is combined into the vector $\bar{\boldsymbol{w}} = (\bar{w}^1, \ldots, \bar{w}^N)$. Then, the vector of fracture height values $\boldsymbol{h} = (h_1, \ldots, h^N)$ is computed from $\bar{\boldsymbol{w}}$ using Eq. (4.5), allowing the system of equations to be written in terms of the effective width $\bar{\boldsymbol{w}}$ only. The tractions are computed from the approximate elasticity relation given in Appendix A and Appendix B and the traction boundary conditions (Eq. (4.9)). The effective pressure values at each element are combined into the vector $\bar{\boldsymbol{p}} = (\bar{p}^1, \ldots, \bar{p}^N)$. Next, the vector $\bar{\boldsymbol{p}}$ is used in the lubrication equation (3.12) to solve for $\bar{w}$.

Before computing the global fluid balance in the wellbore, the local pressure $p_l(0)$ at the wellbore is obtained from the effective pressure $\bar{p}$ using Eq. (4.23). The global fluid balance in the wellbore, given by Eq. (2.9) and (2.10), is solved using the local pressure, which provides the accurate flux distribution Q_k.

The near-tip asymptotics (3.14) provides the tip element length based on $\bar{w}$, which trasnfers to the position of the lateral fracture fronts $\tilde{x}^{(k)}_{\text{tip}+}$ and $\tilde{x}^{(k)}_{\text{tip}-}$. The angle of the tip elements is computed according to Eq. (4.16).

4.3 Numerical results

The mEP3D model's capabilities are illustrated in this section through several examples. Since mEP3D is a reduced-order model, it is first benchmarked against existing analytical and numerical solutions for different fracture geometries. In particular, we consider the following cases: plane strain and radial hydraulic fractures, a single planar hydraulic fracture with symmetric stress barriers, and multiple hydraulic fractures under symmetric stress barriers. In contrast to Chapter 3, here, the plane strain hydraulic fracture is validated for a more general case with leak-off.

4.3.1 Plane strain hydraulic fracture

We start the analysis by considering the simplest case of a plane strain hydraulic fracture. Such a problem has been thoroughly studied in (Adachi and Detournay, 2002; Garagash and Detournay, 2005; Garagash, 2006; Adachi and Detournay, 2008; Detournay, 2004; Dontsov, 2017). It is known to have four different fracture propagation regimes: toughness-storage (K), viscosity-storage (M), toughness-leak-off ($\tilde{K}$), and viscosity-leak-off ($\tilde{M}$). The propagation regime of plane strain fracture is characterized by the following two dimensionless parameters (Dontsov, 2017),

$$K_m = \left(\frac{hK'^4}{\mu' E'^3 Q_0}\right)^{1/4}, \quad \tau = t\frac{h^3 E' C'^6}{\mu' Q_0^3}, \tag{4.27}$$

referred to as dimensionless toughness and time for plane strain fracture. Note that in this paper Q_0 has the dimensions of m^3/s.

In order to model the plane strain hydraulic fracture propagation with mEP3D, we consider a crack with a constant height that is much larger than its length, and whose width is constant along the height direction. The accuracy of the developed mEP3D model in the plane strain case is then determined by comparison with the reference solution. The complete solution of the plane strain problem that accounts for different propagation regimes has been obtained numerically in (Hu and Garagash, 2010; Dontsov, 2017). As a reference solution, we used a fast solution for plane strain fracture from (Dontsov, 2017).

Figure 15a shows the parameter space of K_m and τ on a logarithmic scale. The colored lines show the boundaries of the propagation regimes. The colored circles show the location of the five parameter sets provided in Table 1 and used in calculations. Red, blue, green, and purple circles in Figure 15a are located close to K, M, $\tilde{M}$, and $\tilde{K}$ propagation regimes, respectively, and therefore are referred to by the regime name

and notation. The yellow circle corresponds to the intermediate (or mixed) regime. This choice of parameters allows us to cover the parametric space, thus ensuring the validity of the numerical solution in a wide range of parameters.

Other plots in Figure 15 show the fracture opening at time instants $t = \{100, 500, 1000\}$ s for the propagation regimes consistent with Figure 15a. The mEP3D numerical solution is shown by the colored lines with a staircase-type behavior resulting from the finite grid size, while the reference solution is shown by the black lines. The numerical results show a good agreement with the reference solution for all regimes of propagation. The results that correspond to different $t = \{100, 500, 1000\}$ s can be used to judge the effect of mesh size on the accuracy of the algorithm. The numerical solution has a good accuracy even for the coarse mesh of seven elements per total fracture length at $t = 100$ s.

Table 1: Problem parameters for a **plane strain** hydraulic fracture and the corresponding regimes of propagation: toughness-storage (K), viscosity-storage (M), toughness-leak-off ($\tilde{K}$), viscosity-leak-off ($\tilde{M}$), and the mixed regime.

	K_{Ic} [MPa·m$^{1/2}$]	E [GPa]	ν	μ [cP]	C_L [m/s$^{1/2}$]	Q_0 [m^3/s]	H [m]
K	1	9.5	0.2	3	$3 \cdot 10^{-7}$	$5 \cdot 10^{-4}$	50
M	1	15	0.2	200	$3 \cdot 10^{-7}$	10^{-3}	50
$\tilde{K}$	1	3	0.2	3	$5 \cdot 10^{-4}$	$2 \cdot 10^{-2}$	50
$\tilde{M}$	1	15	0.2	10	10^{-4}	10^{-2}	50
Mixed	1	15	0.2	20	$3 \cdot 10^{-6}$	$4 \cdot 10^{-4}$	50

To compare the numerical algorithm with the reference solution from a different perspective, in Fig. 16 we consider the evolution of the following parameters in time: the fracture width w, the fluid pressure p in the middle between the fracture center and the fracture tip, the fracture length l, and the efficiency η defined as the ratio between fracture volume and the total pumped fluid volume. The efficiency is the lowest for high leak-off as the fracture volume is reduced in this case, as in $\tilde{K}$ and $\tilde{M}$ regimes in Fig. 16d. The numerical algorithm has a good agreement with the

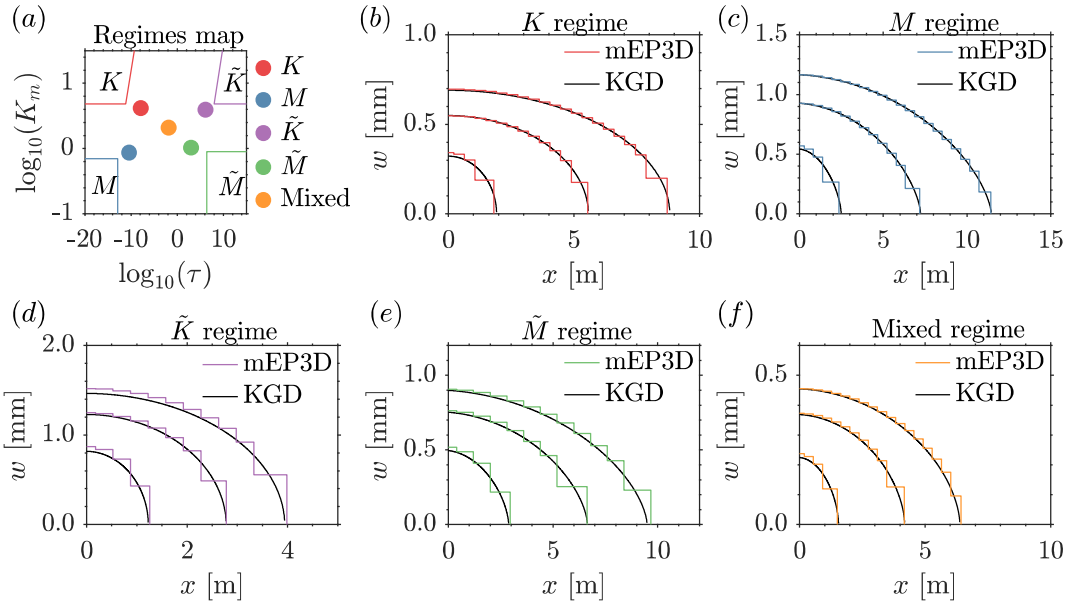

Figure 15: Comparison between the numerical solution (colored lines) and the reference solution (black lines) for plane strain hydraulic fracture. Fracture opening for plane strain hydraulic fracture (b)–(f) at $t = \{100, 500, 1000\}$ s for different propagation regimes from (a).

reference solution at $0 < t < 1000$ s. The $\tilde{K}$ regime tends to have a more pronounced step-wise behavior of the fracture width and pressure caused by high leak-off and high fracture toughness.

4.3.2 Radial hydraulic fracture

This section presents the verification of the mEP3D numerical model for the case of a single radial hydraulic fracture. The problem of radial (or penny-shaped) hydraulic fracture has also been extensively studied in (Detournay, 2004; Savitski and Detournay, 2002; Bunger et al., 2005; Bunger and Detournay, 2007; Madyarova, 2003). The complete numerical solutions have been obtained in (Madyarova, 2003; Dontsov, 2016).

Similarly to the plane strain case, the radial hydraulic fracture propagation has four limiting regimes: toughness-storage (K), viscosity-storage (M), toughness-leak-off ($\tilde{K}$), and viscosity-leak-off ($\tilde{M}$) determined by the following parameters (Dontsov,

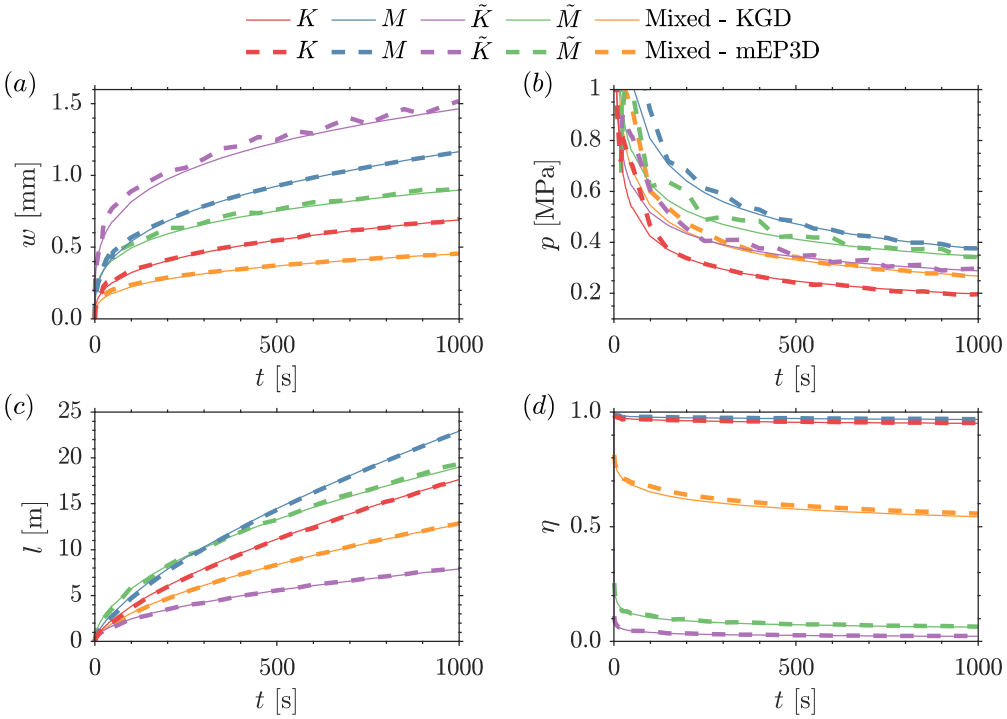

Figure 16: Comparison between the numerical solution (dashed lines) and the reference solution (solid lines) for plane strain hydraulic fracture. Fracture opening, (a), fluid pressure, (b), fracture length, (c), and storage efficiency, (d).

2016),

$$\phi = \frac{\mu'^3 E'^{11} C'^4 Q_0}{K'^{14}}, \quad \tau = t \left(\frac{K'^{18}}{\mu'^5 E'^{13} Q_0^3} \right)^{1/2}, \tag{4.28}$$

referred to as dimensionless leak-off and time for a radial fracture. The comparison covers all the limiting regimes of propagation and an additional intermediate (mixed) regime. The parameters for radial fracture simulation are listed in Table 2.

Figure 17a shows the parameter space with the regions of the dominance of the limiting regimes and the circles closely corresponding to these regimes. Figures 17b-f show the comparison of the numerical mEP3D (colored lines) and the reference (black lines) solutions (Dontsov, 2016) for a HF in isotropic medium in terms of fracture footprint at $t = \{100, 500, 1000\}$ s. Note that the staircase behavior of the mEP3D

solution emphasizes that the fracture height follows the same piece-wise constant discretization as the width. The numerical results show a good agreement with the reference solution for all regimes of propagation. The results show that, while the EP3D numerical solution is not forced to be radially symmetric, its length and height follow the radial fracture solution for all regimes of propagation and the intermediate case.

Table 2: Problem parameters for a **radial** hydraulic fracture and the corresponding regimes of propagation: toughness-storage (K), viscosity-storage (M), toughness-leak-off ($\tilde{K}$), viscosity-leak-off ($\tilde{M}$), and the mixed regime.

	K_{Ic} [MPa·m$^{1/2}$]	E [GPa]	ν	μ [cP]	C_L [m/s$^{1/2}$]	Q_0 [m^3/s]
K	1	9.5	0.2	3	$3 \cdot 10^{-7}$	$5 \cdot 10^{-4}$
M	1	9.5	0.2	200	$3 \cdot 10^{-7}$	10^{-3}
$\tilde{K}$	1	3	0.2	3	10^{-4}	$2 \cdot 10^{-2}$
$\tilde{M}$	1	9.5	0.2	10	10^{-4}	10^{-2}
Mixed	1	9.5	0.2	10	$5 \cdot 10^{-6}$	10^{-3}

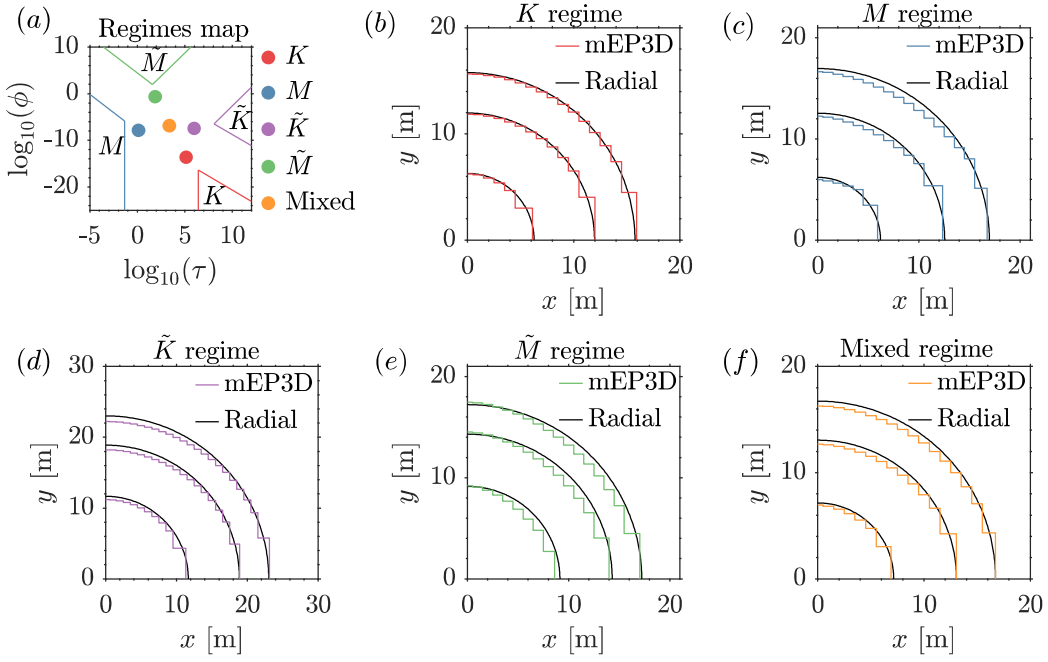

Figure 17: Comparison between the numerical solution (solid colored lines) and the reference solution (solid black lines) for radial hydraulic fracture. Propagation regimes in parameter space, (a), and fracture footprint, (b)–(f) at $t = \{100, 500, 1000\}$ s.

Fig. 18 shows time histories of the fracture opening w at the wellbore, fluid pressure p halfway between the injection point and the lateral tip, fracture length l, and efficiency η. The solid lines show the reference solution (Dontsov, 2016), while the dashed lines show mEP3D result. As can be seen from the figure, the mEP3D algorithm has a good agreement with the reference parameters at $0 < t < 1000$ s in all regimes of propagation as well as for the intermediate case.

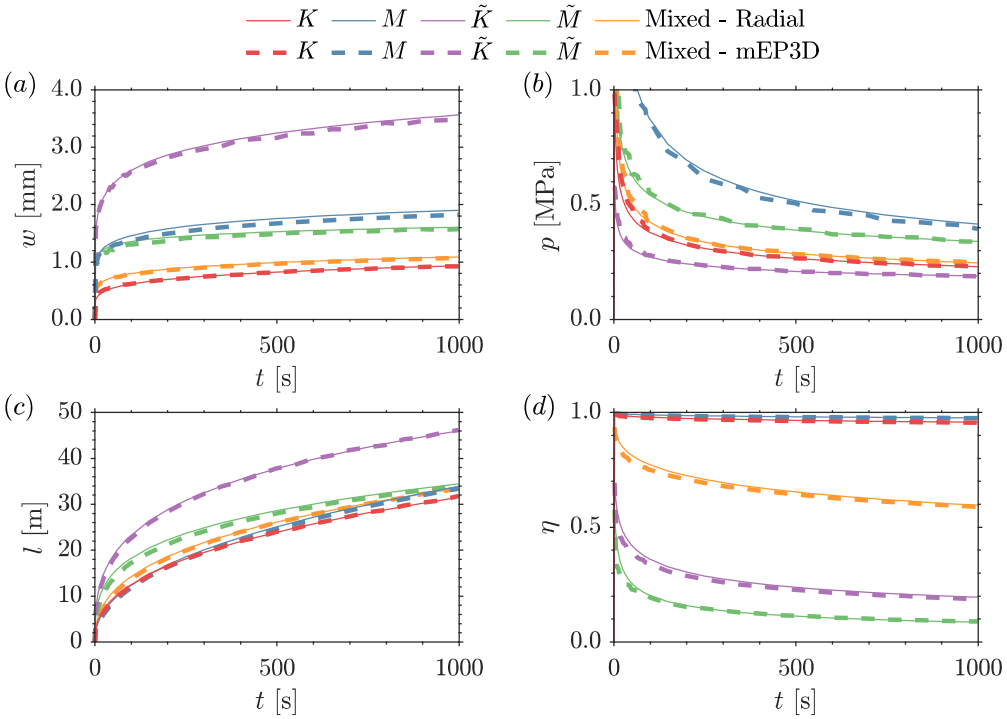

Figure 18: Comparison between the numerical solution (dashed lines) and the reference solution (solid lines) for radial hydraulic fracture. Fracture opening, (a), fluid pressure, (b), fracture length, (c), and storage efficiency, (d).

4.3.3 Hydraulic fracture in presence of symmetric stress barriers

In this section, we quantify the accuracy of the EP3D model for a planar hydraulic fracture propagating through symmetric stress barriers. In this case, the fracture shape remains radial until it reaches the stress barriers. Afterward, propagation in the vertical direction is diminished by stress barriers, and the fracture elongates in the horizontal direction.

The reference solution for this case was obtained using a fully planar hydraulic fracture simulator based on the Implicit Level Set Algorithm, ILSA (Peirce and Detournay, 2008; Dontsov and Peirce, 2017). Note that comparison for the case of one hydraulic fracture with no leak-off was performed between EP3D and ILSA in (Dontsov and Peirce, 2015a). In this section, we perform a similar comparison of mEP3D and ILSA but for the more general case of non-zero fluid leak-off.

To demonstrate the accuracy of the mEP3D model for a wide range of parameters in parameter space, we consider different regimes of propagation. However, different regions of the P3D fracture front can propagate in distinct regimes. Therefore, the problem parameters are chosen with respect to the propagation regimes of a radial fracture at the moment it reaches the stress barriers and summarized in Table 3.

Table 3: Problem parameters for a planar hydraulic fracture in a formation with symmetric stress barriers and the corresponding regimes of propagation: toughness-storage (K), viscosity-storage (M), toughness-leak-off ($\tilde{K}$), viscosity-leak-off ($\tilde{M}$), and the mixed regime.

	K_{Ic} [MPa·m$^{1/2}$]	E [GPa]	ν	μ [cP]	C_L [m/s$^{1/2}$]	Q_0 [m^3/s]	H [m]	$\Delta\sigma$ [MPa]
K	1	9.5	0.2	3	$3 \cdot 10^{-7}$	$5 \cdot 10^{-4}$	20	0.15
M	1	9.5	0.2	200	$3 \cdot 10^{-7}$	10^{-3}	20	0.2
$\tilde{K}$	1	3	0.2	3	10^{-4}	$2 \cdot 10^{-2}$	20	0.1
$\tilde{M}$	1	9.5	0.2	10	10^{-4}	10^{-2}	20	0.2
Mixed	1	9.5	0.2	10	$5 \cdot 10^{-6}$	10^{-3}	20	0.2

Figure 19 shows a footprint of a hydraulic fracture in a formation with symmetric stress barriers in different propagation regimes (described above) and at time instants $t = \{100, 900, 3600\}$ s. The results of the mEP3D model (colored lines) are in a good agreement with ILSA (black lines) except for minor deviations of the crack shape. While the model supports radial fractures with equal height and length, once the fracture reaches the stress barriers, its propagation is based on the plane strain assumption. The deviations of the fracture shape from ILSA's results are visible for cases when the height and the length of fractures are comparable. The EP3D model

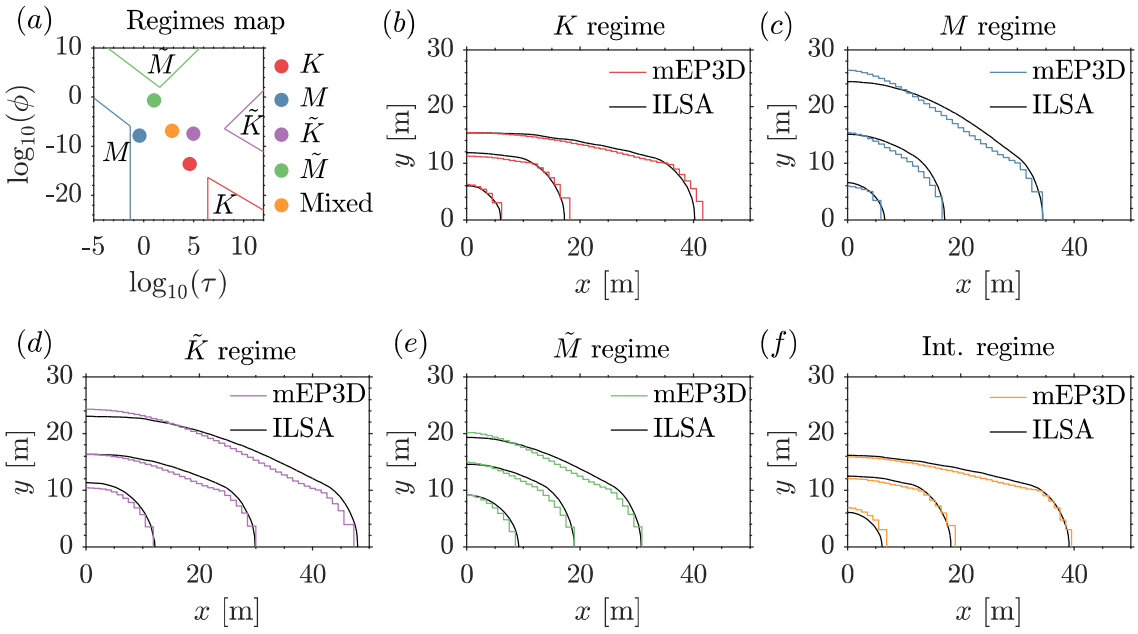

Figure 19: Comparison between the numerical mEP3D solution (colored lines) and the reference ILSA solution (black lines) for a planar hydraulic fracture in a formation with symmetric stress barriers. Propagation regimes in parameter space, (a), and fracture footprint, (b)-(f), at $t = \{100, 900, 3600\}$ s.

produced a similar fracture shape (Dontsov and Peirce, 2015a). Figure 20 shows the expanded numerical results in terms of fracture opening (a), height (b), length (c), and storage efficiency (d) versus time. Note that the discrepancies in M and $\tilde{K}$ regimes at larger times are mostly in the fracture height, while the length and the width are more accurate. This shows that the averaged lubrication equation(4.13), the approximate elasticity potential (4.8), and the asymptotic near-tip solution (C.3) are accurate. The relation between the height and the effective width (4.5) relies on the plane strain assumption and results in the discrepancy. Otherwise, the results have a good agreement.

4.3.4 Multiple parallel hydraulic fractures

This section presents the results of the mEP3D model for multiple hydraulic fractures. As for the single P3D fracture, we use ILSA numerical results as a reference

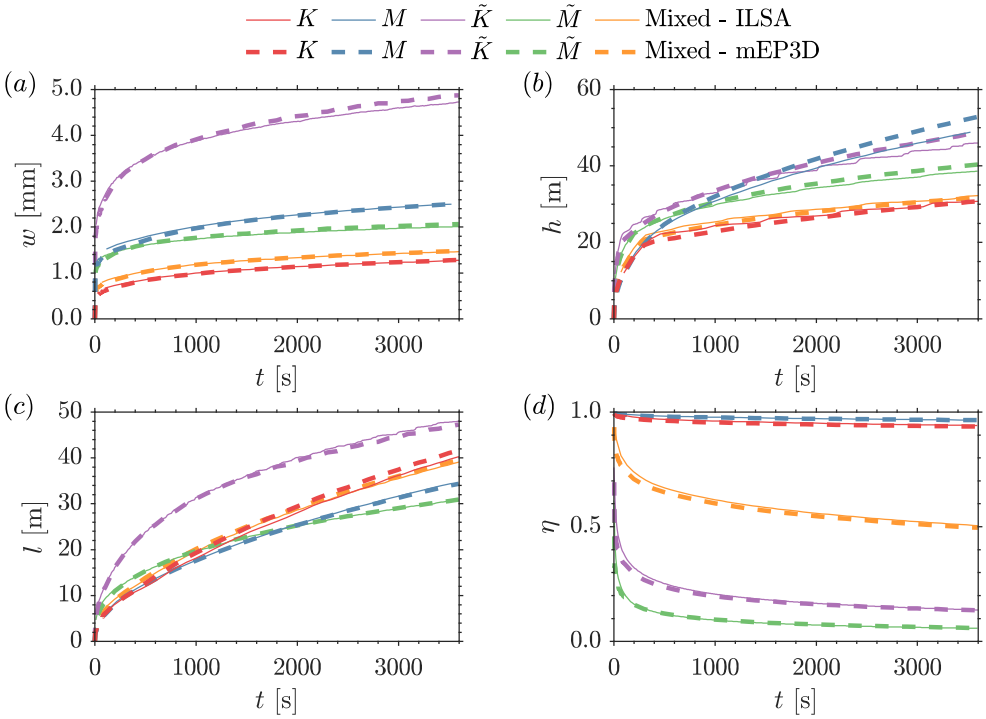

Figure 20: Comparison between the numerical mEP3D solution (dashed lines) and the reference ILSA solution (solid lines) for hydraulic fracture under the condition of symmetric stress barriers for different propagation regimes. Fracture opening (a), height (b), length (c), and storage efficiency (d) vs time.

solution (Dontsov and Peirce, 2016b). ILSA is limited to the analysis of multiple parallel hydraulic fractures, which remain planar as the result of high confining stress. Therefore, in this section, we present the results for planar fractures even though mEP3D allows fracture turning. The calculations were performed for different regimes of propagation and values of spacing between the fractures to cover different possible scenarios. Most of the results are presented for the case of no perforation friction when the pressure is equal at the wellbore for each fracture. In some cases, the so-called limited entry condition was enforced by increasing the perforation friction so that equal fluxes result in each fracture. The problem parameters used for the examples in this section are the same as for a single P3D fracture, whose parameters are given in Table 3, except the fluid flux Q_0 which is here prescribed five times larger

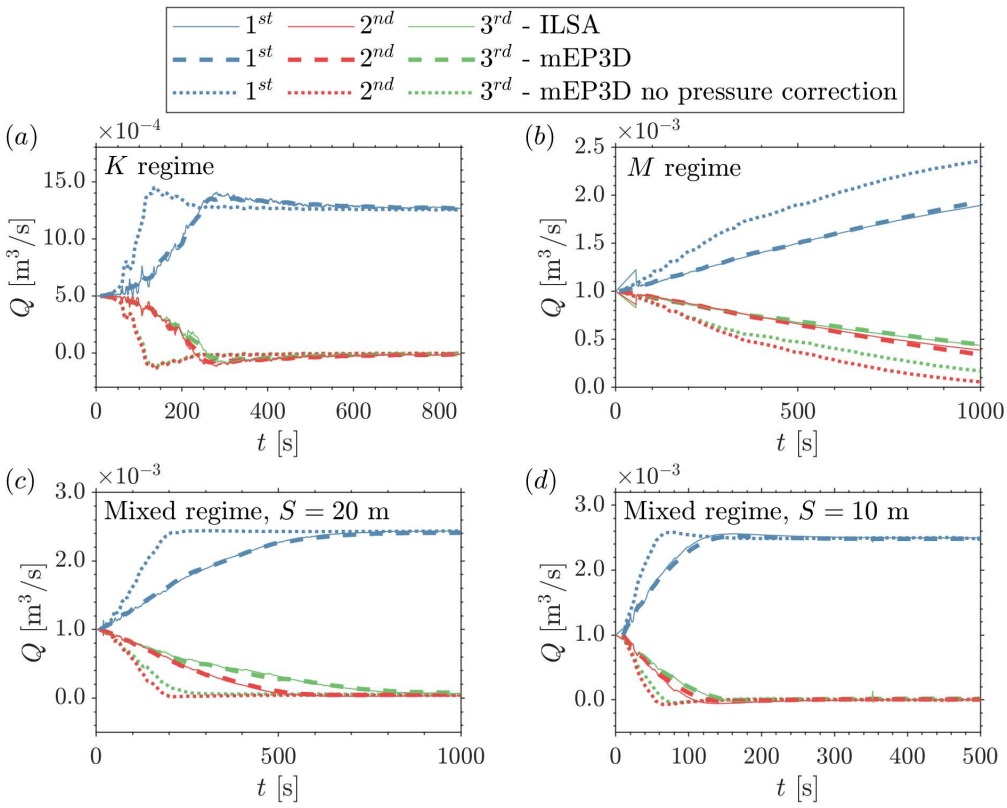

Figure 21: Distribution of fluid flux between multiple parallel hydraulic fractures propagating under the condition of symmetric stress barriers for different fracture spacing S and propagation regimes under the condition of symmetric stress barriers.

than in Table 3 since five fractures are simulated.

The results are presented for the case of no perforation friction for K regime at spacing $S = 30$ m, M regime at $S = 20$ m, the mixed regime at $S = 20$ m and $S = 10$ m. The results are presented for different values of fracture spacing to demonstrate code the accuracy of the reduced-order model. Additionally, the results for $\tilde{M}$ regime are provided for the case of limited entry, i.e., when the flux distribution is equal between all fractures. The latter condition is often encountered in the field and is used to promote more uniform fracture growth. The results for $\tilde{K}$ regime are not presented as the reference solution for this regime was not available, as this regime is known to be very difficult to represent in numerical computations.

Figure 21 shows the distribution of fluxes between fractures under the assumption

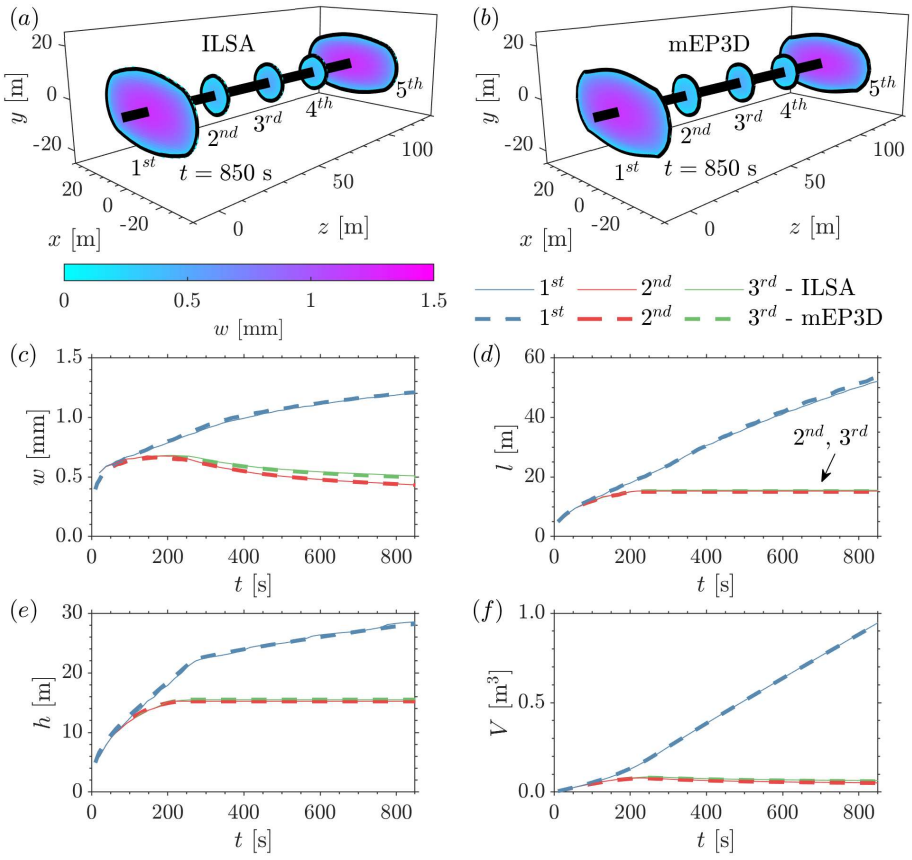

Figure 22: Numerical solution for multiple parallel hydraulic fractures propagating in a formation with symmetric stress barriers for K regime and spacing $S = 30$ m. Fracture footprint, (a)-(b), opening, (c), length, (d), height, (e), and volume, (f).

of no perforation friction. In this case, the pressure at the wellbore at each fracture is the same, which results in an uneven fluid flux distribution between fractures. The results are shown for K, M, and mixed regimes defined as in Table 3 but for larger Q_0, as mentioned above. Also, the flux distribution for a mixed regime is shown for different fracture spacing $S = 20$ m (Fig. 21c) and $S = 10$ m (Fig. 21d). Due to the symmetry of the problem, for this and the following cases, we present the results only for the first, second, and third fractures. The results for the mEP3D model without pressure correction (dotted lines) are based on the reduced one-dimensional model that does not capture the near-wellbore pressure singularity, see Section 4.2.3. As a result, the flux distribution based on this model shows a poor agreement with the reference ILSA solution (solid lines). The largest deviation is observed when the viscous effects dominate the solution. In M regime, it occurs throughout the whole fracture propagation, while for K and mixed regimes, the viscous effects are observed at the early time of propagation but fade afterward. As the fracture grows, the velocity of the fracture tip decreases and the effects of fracture toughness and rock elasticity become more prominent compared to viscous effects. Therefore, the agreement improves at larger times for K and mixed regimes. To improve the model, the pressure correction introduced for as detailed in Section 4.2.3 leads to accurate predictions of pressure at the wellbore and, therefore, flux distributions (dashed lines), which are in good agreement with ILSA.

Figures 22-25 show the full numerical results for K, M, and mixed regimes at $S = 20$ m and $S = 10$ m, respectively, which correspond to the cases for which flux distributions in Figure 21 were illustrated.

Figure 22a-b show the footprints of the five fractures propagating in K regime for ILSA and mEP3D. The thick black lines denote the horizontal wellbore. The fractures propagate radially from the wellbore, but upon reaching the stress barriers,

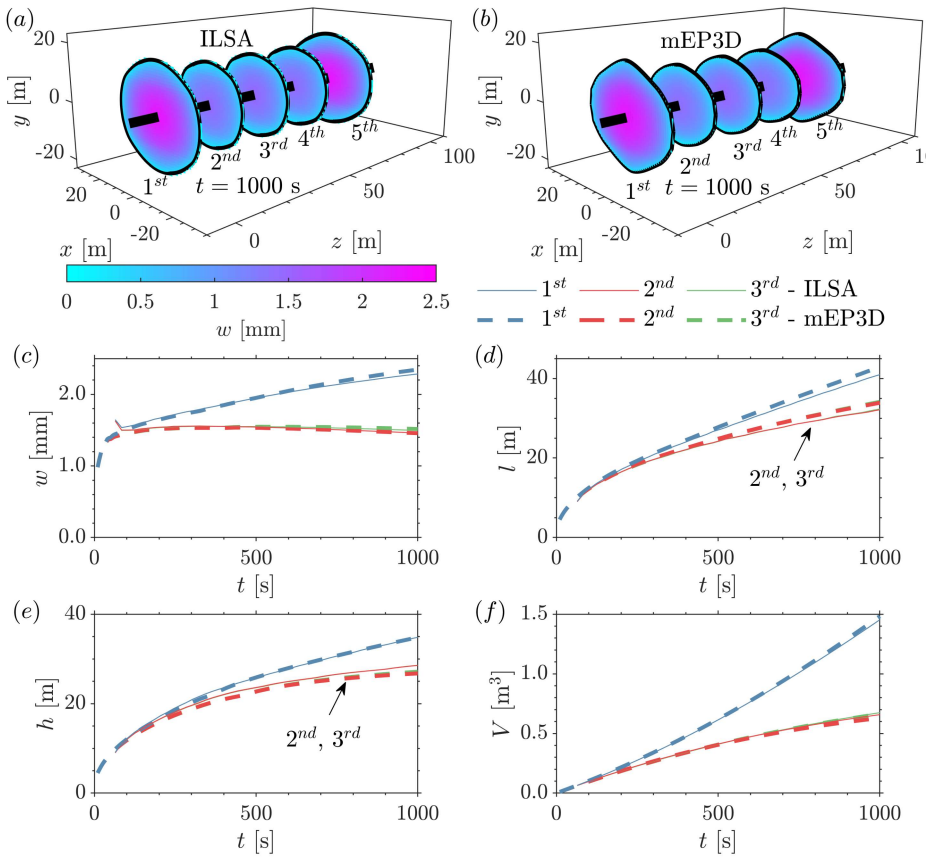

Figure 23: Numerical solution for multiple parallel hydraulic fractures propagating in a formation with symmetric stress barriers for M regime and fracture spacing $S = 20$ m. Fracture footprint, (a)-(b), opening, (c), length, (d), height, (e), and volume, (f).

they become elongated in the x direction.

Figure 22c-f show the opening, the length, the height, and the volume of the first, second, and third fractures for the set of parameters corresponding to M regime. The solution for the fourth and fifth fractures is identical to the one for the second and the first fractures due to problem symmetry. The height of the fracture is the maximum height of the fracture, which corresponds to the element at the wellbore. The fracture opening corresponds to the maximum fracture opening at the wellbore. To cater for a possibility of non-planar behavior, we define the maximum length of the fracture as a sum of the lengths of the individual elements of the one-dimensional mesh. All the mEP3D numerical results (dashed lines) are in a good agreement with ILSA (solid

lines) for all fractures for K regime.

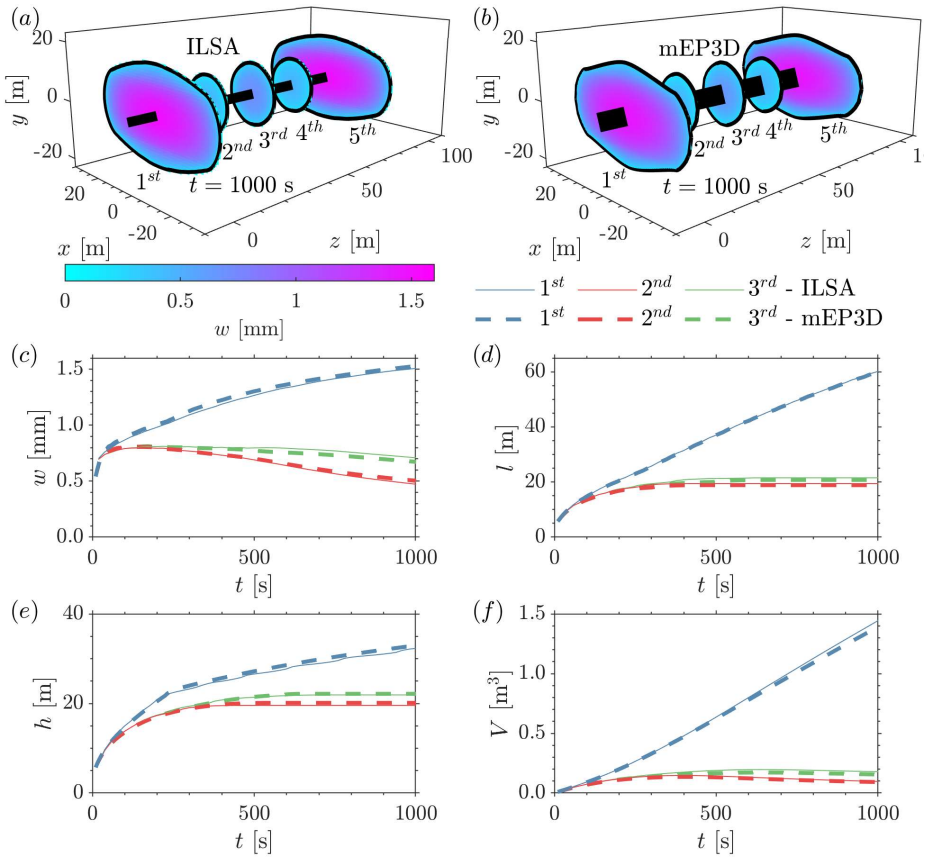

Figure 24: Numerical solution for multiple parallel hydraulic fractures propagating in a formation with symmetric stress barriers for the mixed regime and fracture spacing $S = 20$ m. Fracture footprint, (a)-(b), opening, (c), length, (d), height, (e), and volume, (f).

Figure 23 shows the numerical results for five fractures propagating in M regime at spacing $S = 20$ m. The results are presented in the same form as in Figure 22. For the M regime, the three inner fractures are only slightly smaller than the two outer fractures compared to K regime where inner fractures are significantly suppressed. Note that the fracture spacing used for M regime is 20 m and for K regime is 30 m, i.e., even when the fractures are close enough in M regime, the inner fractures are not suppressed compared to K regime where suppression occurs even at the larger spacing between the fractures. This happens because the M regime is known to make the flux distribution among fractures more even and, in turn, leads to equal fracture

sizes. Note that for M regime, the fractures are much less elongated in a horizontal direction so that fracture height becomes comparable to the fracture length. The mEP3D results show that the fractures have a peak in height above and below the wellbore, which introduces a noticeable difference from the ILSA results. This peak can be explained by the inaccuracy of the plain strain assumption used in the mEP3D model, which becomes invalid when the fracture height becomes comparable to the fracture length. This is also why the mEP3D results slightly overestimate the height of the fractures (Fig. 23e). At the same time, other fracture dimensions and volume are predicted accurately.

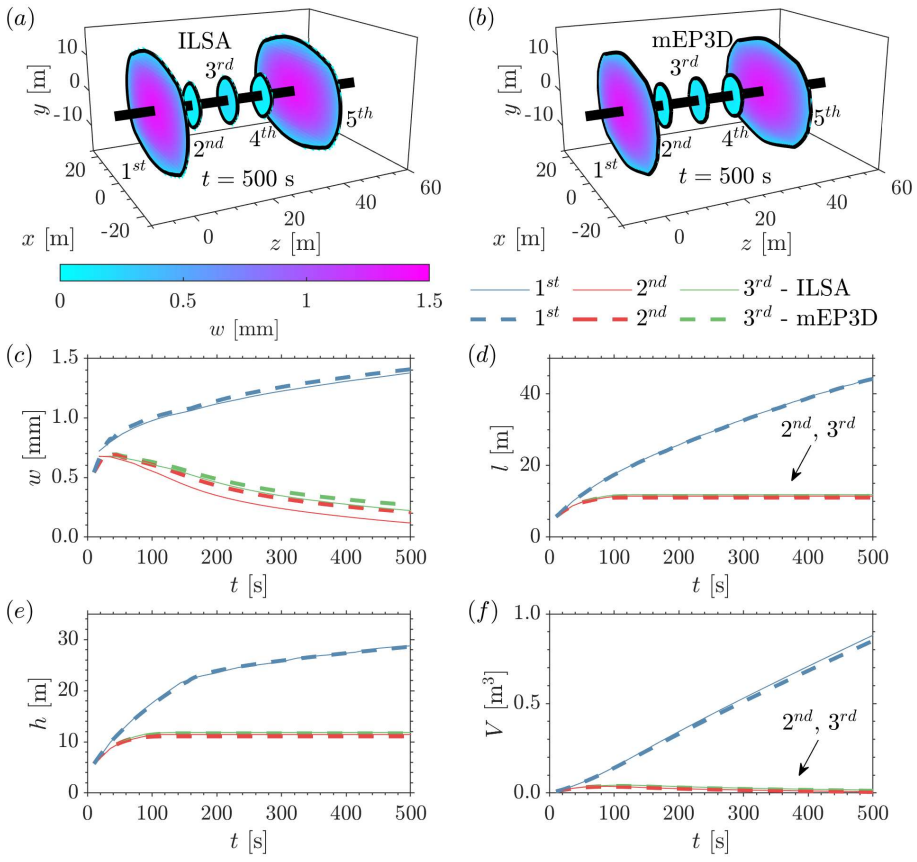

Figure 25: Numerical solution for multiple parallel hydraulic fractures propagating in a formation with symmetric stress barriers for mixed regime and spacing $S = 10$ m. Fracture footprint, (a)-(b), opening, (c), length, (d), height, (e), and volume, (f).

Figures 24, 25 show similar numerical results for the mixed regimes at fracture

spacing $S = 20$ m and $S = 10$ m, respectively. For mixed regimes, in contrast to M regime, the inner fractures are significantly suppressed and the outer fractures have the largest volume and dimensions compared to the inner fractures. This means that the fluid viscosity effects are not sufficient to make the flux distribution equal for the considered combinations of problem parameters. At smaller spacing (Fig. 25), the three inner fractures are suppressed in higher degree compared to the case of larger spacing (Fig. 24). The agreement between mEP3D and ILSA is reasonably good for larger spacing, while for smaller spacing the fracture openings of inner fractures are slightly overestimated by mEP3D.

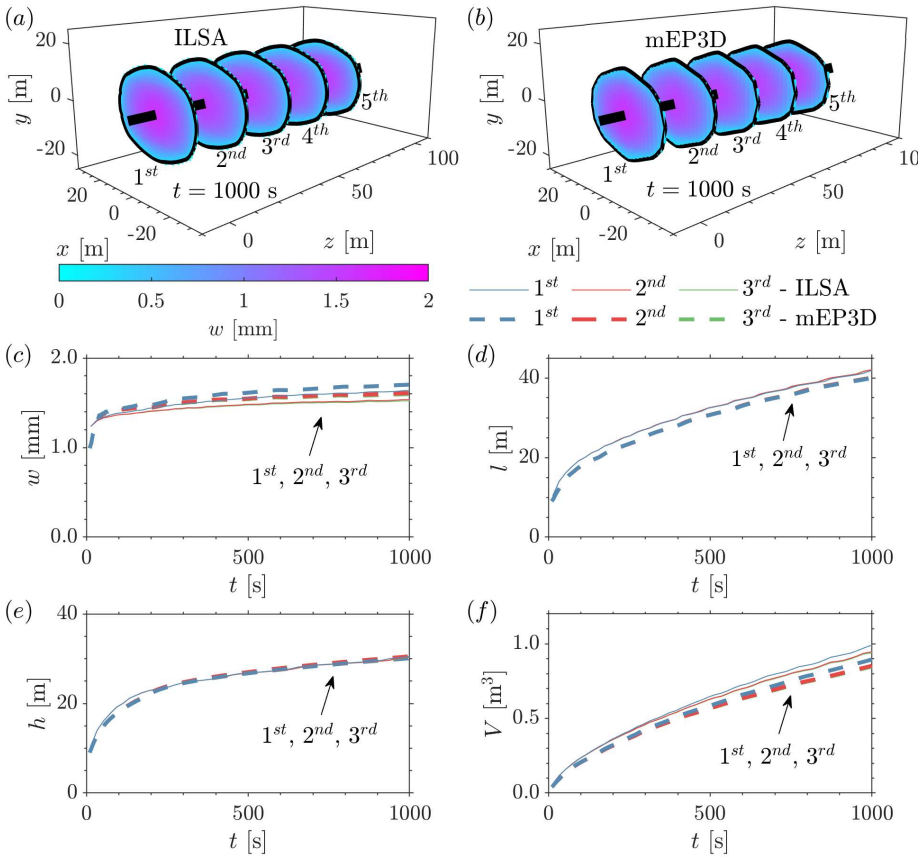

Figure 26: Numerical solution for multiple parallel hydraulic fractures propagating in a formation with symmetric stress barriers for $\tilde{M}$ regime and fracture spacing $S = 20$ m and limited entry. Fracture footprint, (a)-(b), opening, (c), length, (d), height, (e), and volume, (f).

We also present the results for $\tilde{M}$ regime in Figure 26. For this regime, instead

of applying the no perforation friction assumption, the fluxes for each fracture are equal as a result of imposing the limited entry condition. The reason for selecting this case is because the assumption of no perforation friction results in the total suppression of the three inner fractures and therefore is trivial. Under limited entry, all the fractures have similar size, a result that may appear trivial but at the same time is qualitatively different from previously shown results. The developed mEP3D model slightly overestimates fracture lengths and underestimates the fracture width but generally provides good approximations for this case. Note that the fracture volume is much less than the injected fluid volume, so the error normalized by the injection volume is practically negligible.

4.3.5 Non-planar fracture growth

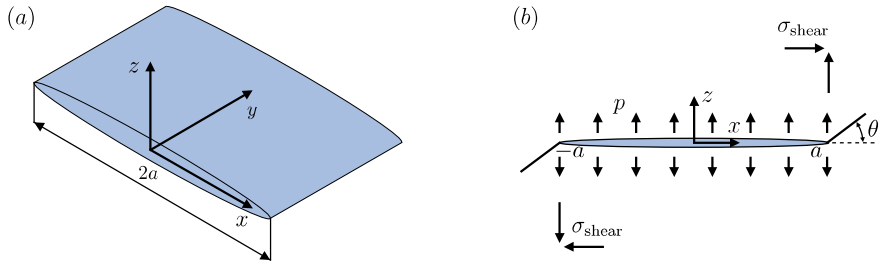

Figure 27: (a) Scheme of a plane strain fracture with respect to x, y, z. (b) Scheme of a plane strain fracture turning under applied fluid pressure and far-field shear stress.

To validate the fracture turning algorithm, we consider a hydraulic fracture of length $2a$ under plane strain conditions in the xz-plane, see Figure 27. The fracture is subjected to a uniform shear in the far-field, σ_{shear}, and an internal fluid pressure p. Due to the shear stress, the direction of propagation deviates from the fracture plane by the angle θ.

First, the turn angle θ is computed numerically with the mEP3D model for the following problem parameters: $E' = 9.5$ GPa, $\nu = 0.2$, $\mu = 0.2$ Pa·s, $C_L = 3 \cdot$

10^{-7} m/s$^{1/2}$, $Q_0 = 10^{-3}$ m^3/s, $a = 3.5$ m, and $h = 100$ m. Here, h is the height of the fracture in the y direction, which is prescribed sufficiently large compared to the fracture length a ($h \gg a$) to ensure plane strain conditions. The parameters used correspond to the intermediate propagation regime. The Mode I stress intensity factor is prescribed to be $K_I = 1$ MPa·m$^{1/2}$ before the turn. The value of the shear stress σ_{shear} is varied to cover different values of angle θ. The numerical algorithm does not compute the value of K_{II} to determine the turn direction. Instead, it seeks the direction in which the shear displacement at the tip is zero, which corresponds to $K_{II} = 0$.

The results of the numerical simulation are compared to the analytical solution. The latter is based on the zero Mode II theory (Cotterell and Rice, 1980), where the local stress intensity factors (those of the extended crack) are given to first order as

$$\begin{aligned} K_I^{\text{local}} &= \frac{K_I}{4}\left[3\cos\left(\frac{\theta}{2}\right) + \cos\left(\frac{3\theta}{2}\right)\right] - \frac{K_{II}}{4}\left[\sin\left(\frac{\theta}{2}\right) + \sin\left(\frac{3\theta}{2}\right)\right], \\ K_{II}^{\text{local}} &= \frac{K_I}{4}\left[\sin\left(\frac{\theta}{2}\right) + \sin\left(\frac{3\theta}{2}\right)\right] + \frac{K_{II}}{4}\left[\cos\left(\frac{\theta}{2}\right) + 3\cos\left(\frac{3\theta}{2}\right)\right]. \end{aligned} \tag{4.29}$$

The turn angle corresponding to $K_{II}^{\text{local}} = 0$ is therefore

$$\theta = 2\arctan\left(\frac{K_I - \sqrt{K_I^2 + 8K_{II}^2}}{4K_{II}}\right). \tag{4.30}$$

The Mode II stress intensity factor K_{II} is prescribed through σ_{shear}, using the analytical result for a plane strain fracture in pure shear stress field (Tada et al., 2000),

$$K_{II} = \sigma_{\text{shear}}\sqrt{\pi a}. \tag{4.31}$$

Knowledge of K_I and σ_{shear} is sufficient to determine the turn angle θ based on the analytical solution (4.30) with the use of (4.31). This result is used as a reference to

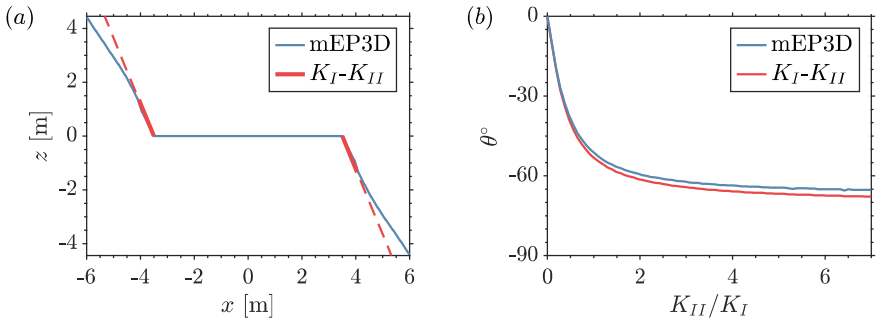

Figure 28: (a) Numerical solution for a plane strain hydraulic fracture under uniform shear stress (solid lines). The dashed red lines show theoretical prediction according to (4.30). (b) Direction of the fracture growth for different values of K_{II}/K_I. The solid blue line shows mEP3D numerical solution, while the red line indicates theoretical prediction (4.30).

validate the initial turn angle computed by the mEP3D model. Figures 28a shows the crack path and the initial turn angle computed with the mEP3D simulation (blue lines) and the turn angle according to the reference solution (red lines) at $K_{II}/K_I = 6$. The mEP3D fracture in Figure 28a initially propagates at the angle of -67° and then the angle slowly goes to -45°. The red lines in Figure 28a shows the direction of the propagation according to the analytical relation (4.30). The initial turn angle of the numerical solution is in excellent agreement with the analytical relation.

Figure 28b shows the comparison of the initial angle of the fracture turn versus the ratio of K_{II}/K_I. Results of the mEP3D model and analytical prediction are in a good agreement. Small discrepancies that are observed can be related to the discretization error in the mEP3D model. Specifically, the near-front part of the fracture is represented by the rotated planar tip element, which does not capture the curvature near the tip.

In addition to the solution for a plane strain fracture under applied shear stress, we present the numerical results for multiple interacting fractures. The results are computed for the parameters for K, M, $\tilde{K}$, $\tilde{M}$, and mixed regimes from Table 3. The total injection rate is five times Q_0 since five fractures are considered in this

example. The spacing between injection points is set to 10 m, and limited entry is enforced in all cases to intensify the elastic interactions between fractures. The cracks are initiated at 5° angle from the normal to the wellbore to incorporate a small asymmetry into the problem and remove solutions with unstable configurations. The compressive geological stress is applied with the normal component in the x direction denoted by σ_1 (maximum horizontal stress), and in the z direction by σ_2 (minimum horizontal stress). The selected values of σ_1 and σ_2 correspond to weak and strong stress contrasts relative to the fluid pressure. Therefore, the fracture propagation is not limited to planar surfaces (in contrast to the case when the stress contrast much larger than the fluid pressure). The minimum stress is kept constant for all cases, namely $\sigma_2 = -10$ MPa. For $\tilde{K}$ regime, we consider the following two values of the maximum stress $\sigma_1 = -10.2$ MPa (weak contrast), and $\sigma_1 = -10.5$ MPa (strong contrast). For other regimes, namely K, M, $\tilde{M}$, and mixed regimes, we take $\sigma_1 = -10.1$ MPa (weak contrast), and $\sigma_1 = -10.5$ MPa (strong contrast).

The results of simulations are presented in Figures 29-33 at 1000 s after the initiation. The fractures are differentiated by color: blue is the first crack, red is the second, green is the third, yellow is the forth, purple is the fifth. The black color indicates the wellbore.

The results of K regime are shown in Figure 29. The weak stress contrast is presented in Figure 29a and Figure 29b, where the first figure shows the paths of five cracks in top view on the xz plane, and the second shows the crack footprints on a side view on the $\tilde{x}\tilde{y}$ plane. The strong stress contrast case is illustrated in Figure 29c and Figure 29d, where the first figure shows the paths of five cracks in top view on the xz plane, and the second the crack footprints on a side view on the $\tilde{x}\tilde{y}$ plane. In both the weak and the strong stress contrast cases, the crack growth in the x direction in Figures 29a,c is not symmetrical with respect to the wellbore. Since the elastic effects

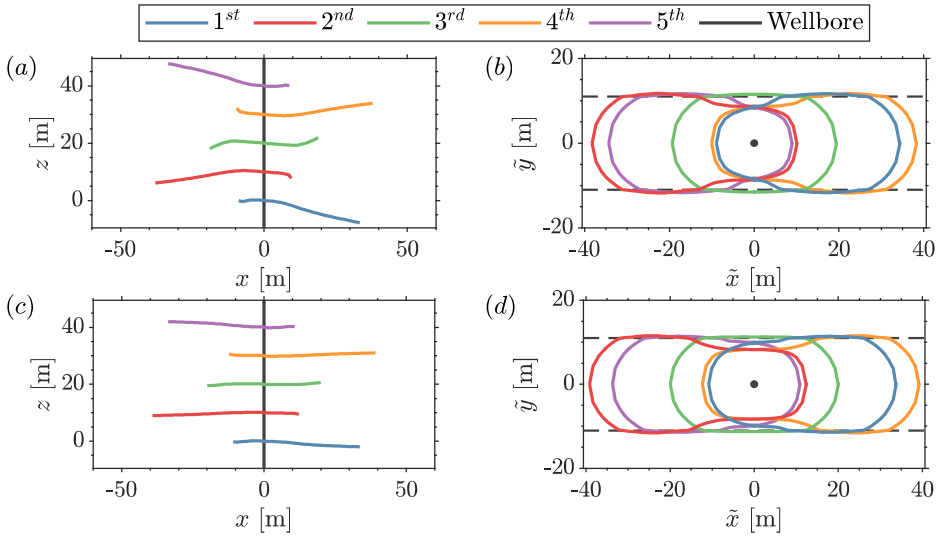

Figure 29: Numerical solution for curved hydraulic fractures propagating in K regime at $t = 1000$ s under limited entry conditions. (a)-(b): Top and side views of crack path for weak stress anisotropy $\sigma_1 = -10.1$ MPa, $\sigma_2 = -10$ MPa; (c)-(d): Top and side views of crack path for strong stress anisotropy $\sigma_1 = -10.5$ MPa, $\sigma_2 = -10$ MPa.

are strong in K regime, the cracks tend to grow away from each other. Similar results were obtained in (Dontsov and Suarez-Rivera, 2020) using a fully three-dimensional hydraulic fracturing simulator. Finally, it is interesting to observe that despite the small initial crack angle, the cracks 1, 2, 4, and 5 grow in the z direction almost symmetrically relative to the central fracture.

The M regime fractures are presented in Figure 30 with weak stress contrast in Figure 29a and Figure 29b, and strong stress contrast in Figure 29c and Figure 29d. The plots show the cracks in top view on the xz plane and side view on the $\tilde{x}\tilde{y}$ plane. In both stress contrast cases, the cracks grow symmetrically in the x direction relative to the wellbore. The fluid viscosity may be the driving factor that preserves the symmetric growth, which is consistent with the earlier results in (Dontsov and Suarez-Rivera, 2020). The inclination and asymmetry of the cracks in the z direction in weak stress contrast in Figure 30a is due to the initial 5° angle to the x axis. The crack growth in the z direction in strong contrast in Figure 30c is symmetrical with

respect to the central fracture.

The results of $\tilde{K}$ regime are shown in Figure 31. The weak and strong stress contrast cases are given in Figures 29a,b and Figures 29c,d, respectively. The cracks' tendency to grow away from each other is similar to the K regime.

The curved cracks in $\tilde{M}$ regime are shown in Figure 32 with those in weak stress contrast given in Figure 29a,b and those in strong stress contrast given in Figure 29c,d. In weak stress, cracks two and four exhibit attraction to the outer cracks 1 and 5. Otherwise, the cracks grow more equally in positive and negative $\tilde{x}$ directions than in the K and $\tilde{K}$ cases, but less than in the M case.

The results of the mixed regime are presented in Figure 33. The weak stress contrast case is demonstrated in Figure 29a,b, and the strong stress contrast in Figure 29c,d. The cracks grow more equally in positive and negative $\tilde{x}$ directions than in the K and $\tilde{K}$ cases, but less than in the M case.

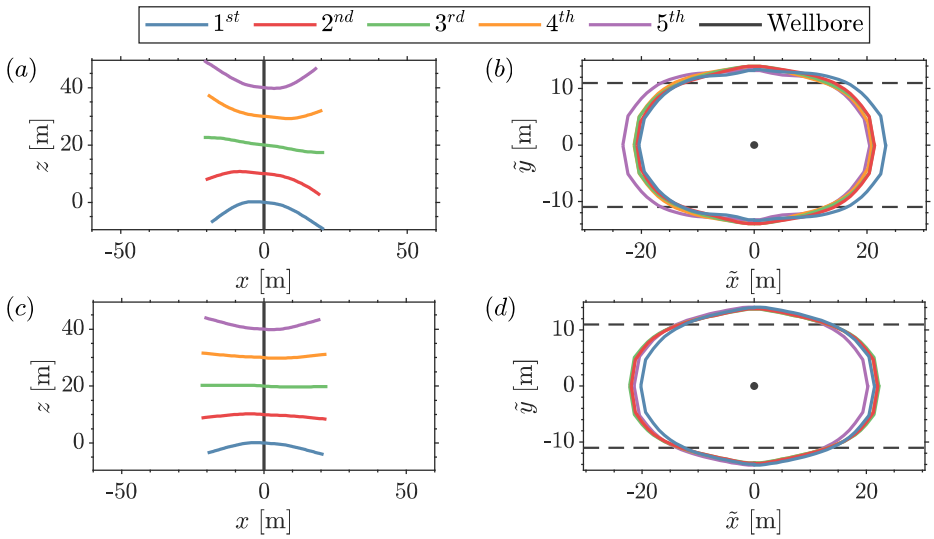

Figure 30: Numerical solution for curved hydraulic fractures propagating in M regime at $t = 1000$ s under limited entry conditions. (a)-(b): Top and side views of crack path for weak stress anisotropy $\sigma_1 = -10.1$ MPa, $\sigma_2 = -10$ MPa; (c)-(d): Top and side views of crack path for strong stress anisotropy $\sigma_1 = -10.5$ MPa, $\sigma_2 = -10$ MPa.

This section presented numerical results for the mEP3D model in the context of

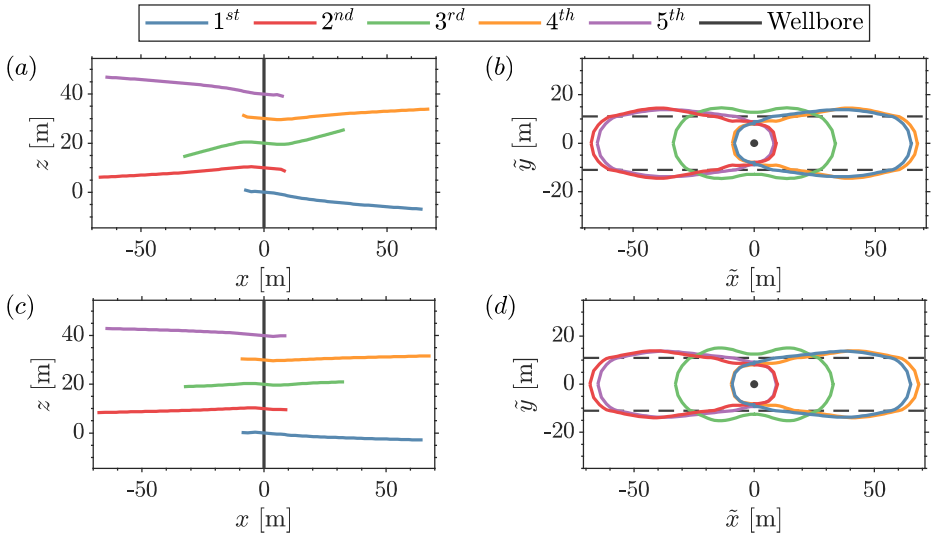

Figure 31: Numerical solution for curved hydraulic fractures propagating in $\tilde{K}$ regime at $t = 1000$ s under limited entry conditions. (a)-(b): Top and side views of crack path for weak stress anisotropy $\sigma_1 = -10.2$ MPa, $\sigma_2 = -10$ MPa; (c)-(d): Top and side views of crack path for strong stress anisotropy $\sigma_1 = -10.5$ MPa, $\sigma_2 = -10$ MPa.

non-planar fractures, which is one of the distinguishing features of the algorithm. First, the crack front turning algorithm has been validated for a plane strain hydraulic fracture subjected to the shear stress field. Then, numerical solutions for five simultaneously growing non-planar hydraulic fractures have been presented for the cases of weak and strong stress anisotropy. Results demonstrate that the fracture behavior varies as a function of the regime of propagation - something that has also been observed previously using a fully 3D simulator. This once again demonstrates the algorithm's ability to capture the primary physical processes that are relevant for the modeling.

4.4 Summary

This chapter presented a computationally fast hydraulic fracturing model for multiple non-planar hydraulic fractures (HFs) propagating in a homogeneous linear elastic rock with symmetric stress layers. The formulation of the method is based on a model

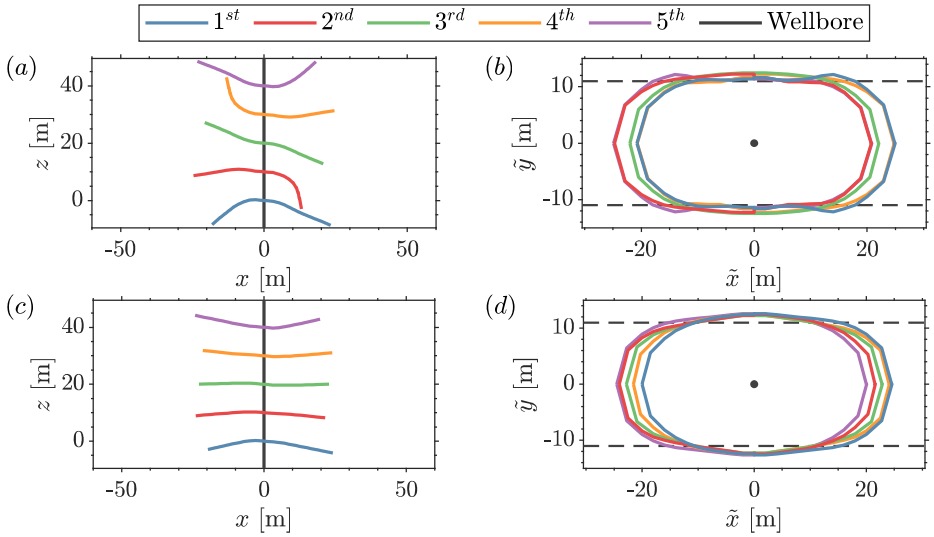

Figure 32: Numerical solution for curved hydraulic fractures propagating in $\tilde{M}$ regime at $t = 1000$ s under limited entry conditions. (a)-(b): Top and side views of crack path for weak stress anisotropy $\sigma_1 = -10.1$ MPa, $\sigma_2 = -10$ MPa; (c)-(d): Top and side views of crack path for strong stress anisotropy $\sigma_1 = -10.5$ MPa, $\sigma_2 = -10$ MPa.

order reduction of the exact problem, and it extends the enhanced pseudo-3D (EP3D) model that was originally developed for a single planar fracture. We have made substantial modifications to the EP3D model to account for multiple non-planar HFs (mEP3D).

The exact problem is reduced by approximating the crack surface into a series of piece-wise constant elements along its length by assuming plane strain (or radial) fracture opening across the vertical cross-section of each element. Similarly to EP3D, the analytical solutions for plane strain and radial fractures are modified to account for the fluid viscosity. In addition, we have considered the effect of fluid leak-off.

We have incorporated discretization of the integral equations, that relate displacements and tractions along the crack, by approximating the displacements discontinuities in each vertical cross-section as a combination of ellipses, similar to the EP3D model. However, due to the non-planarity of the problem, the method has been extended to include integral equations, responsible for the shear components, and a

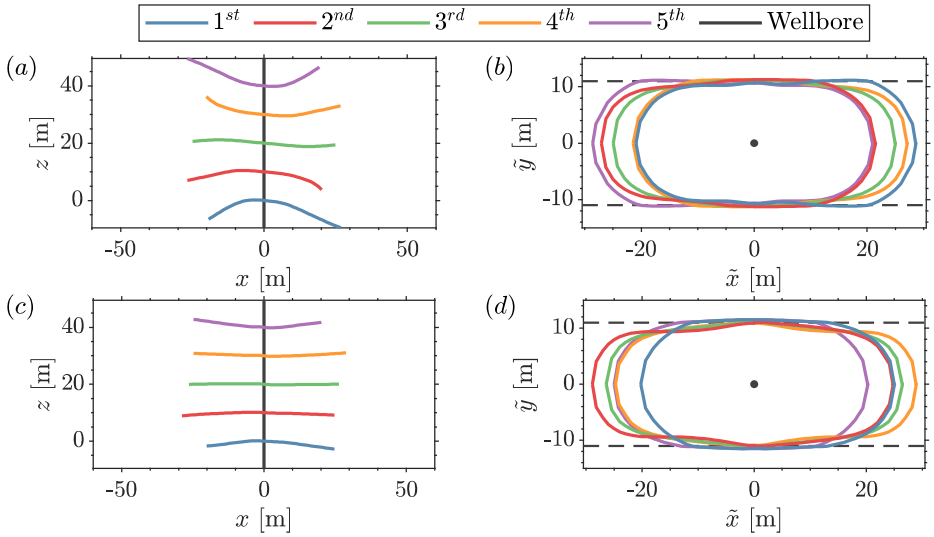

Figure 33: Numerical solution for curved hydraulic fractures propagating in mixed regime at $t = 1000$ s under limited entry conditions. (a)-(b): Top and side views of crack path for weak stress anisotropy $\sigma_1 = -10.1$ MPa, $\sigma_2 = -10$ MPa; (c)-(d): Top and side views of crack path for weak stress anisotropy $\sigma_1 = -10.5$ MPa, $\sigma_2 = -10$ MPa.

fixed mesh accounting for a coordinate rotation.

We have implemented a recently developed multi-scale near-tip asymptotic solution (Dontsov and Peirce, 2015c) that relaxes mesh size requirements by incorporating fracture toughness, fluid viscosity, and leak-off fracture propagation regimes at different length scales. The formulation uses the zero Mode II criterion to select the direction of the crack extension, and the extension is determined according to the Mode I stress intensity factor equal to the fracture toughness.

We have identified that the standard approach taken in the EP3D model underestimates fluid pressure near the wellbore because of the constant pressure assumption at any vertical cross-section. This issue is important for multiple fractures due to the flux distribution equation. We have proposed correction by constructing an equivalent two-dimensional fluid flow problem and solving it for fluid pressure near the wellbore.

To demonstrate the accuracy of the developed mEP3D model, we verify the results

of mEP3D by comparison with reference analytical and numerical solutions. The considered problem cases are a single plane strain hydraulic fracture, a single hydraulic fracture in isotropic medium (radial crack), and hydraulic fractures in a medium with symmetric stress layers. The results for the latter case are presented separately for a single crack and five equally spaced interacting planar cracks. The respective reference solutions have been obtained using the plane strain hydraulic fracture model, the radial hydraulic fracture model, and the hydraulic fracturing simulator based on the Implicit Level Set Algorithm (ILSA) (Peirce and Detournay, 2008). The comparison tests cover different fracture propagation regimes: viscosity-storage, viscosity-leak-off, toughness-storage, toughness-leak-off. The propagation regime corresponding to the symmetric stress layers case describes the state of a radial fracture upon reaching the stress barriers.

The numerical solutions for fracture opening, height, length, and storage efficiency are in a good agreement with the reference solutions for all the considered propagation regimes and different time instants. For multiple hydraulic fractures, in addition, we have provided the results for the distribution of fluid flux between fractures, which show the effect of the near-wellbore pressure correction.

To show capabilities of the mEP3D model for non-planar fractures, first, we validate the fracture turning for a single plane strain fracture under shear loading conditions. The angle obtained numerically for this problem is in a good agreement with the analytical predictions. Next, the results for multiple non-planar HFs have been demonstrated for different propagation regimes and strong and weak stress contrasts.

The proposed mEP3D model implements an efficient model order reduction for multiple non-planar hydraulic fractures in symmetric stress layers. The main feature of the model lies in its computational advantage over the direct solution methods, and the model has shown to be accurate by validating it against the reference models.

5 Efficient computation of fluid flow around hydraulic fracture

5.1 Background

Most hydraulic fracturing models consider rock to be brittle and elastic, and account for the poroelasticity effects produced by rock permeability through assumptions that simplify the analysis (S. H. Advaniand and Lee, 1990; Adachi et al., 2007; Adachi and Detournay, 2008; Dontsov and Peirce, 2015a; Wu et al., 2017; Dontsov and Peirce, 2017; Detournay, 2016; Zia and Lecampion, 2020; Settari et al., 1985; Madyarova, 2003; Savitski and Detournay, 2002; Bunger et al., 2005; Dontsov, 2016). These cited models, for example, use Carter's leak-off law (Carter, 1957), which considers one-dimensional pressure-independent filtration in the direction perpendicular to the fracture surface. However, in practice, the difference between the pore pressure and the fluid pressure inside the crack varies both spatially and with respect to time (Gottschling et al., 2010). Some models proposed a pressure-dependent mechanism of fluid exchange to replace Carter's law for radial and semi-infinite hydraulic fractures (Kanin et al., 2020b,a). The latter model is still based on solving the one-dimensional diffusion equation perpendicular to fracture, which stems from the assumption of the smallness of the diffusion length scale relative to fracture size. For a more general case involving potentially large pressure diffusion zones, a rigorous way to describe the fluid filtration is to couple the fluid flow inside the crack with three-dimensional diffusion throughout the porous media. Realizing the need for hydraulic fracture simulation in poroelastic media, several studies developed fully coupled models for single (Boone and Ingraffea, 1990; Boone et al., 1991; Vandamme and Roegiers, 1990; Kovalyshen, 2010) or multiple fractures (Sherman et al., 2015; Rezaei et al., 2019; Chukwudozie et al., 2019; McClure et al., 2018). In addition,

simulation of reservoir flow requires not only a realistic description of fracture propagation but also fluid flow in the surrounding porous medium at the production stage, where a somewhat similar coupled problem occurs.

This chapter describes the coupling of fluid flow and crack extension in a poroelastic medium. Because this study is concerned with the computational efficiency of hydraulic fracture simulators, we propose a method that couples the previously discussed reduced-order models for hydraulic fracture with a computational paradigm that accelerates the numerical solutions of problems involving fluid flow in porous media. Such acceleration is possible for the porous media flow problem because it is formulated in terms of partial differential equations. The fracture propagation problem, on the other hand, cannot benefit from this technique because the associated elasticity equations are integral equations. The acceleration of the fracture component of the problem is achieved by the previously described reduced-order models. Here we have prepared the groundwork for this coupled computational approach by developing a software package used in combination with state of the art scientific computing frameworks, to enable the necessary tools for accelerated fluid flow simulations. Several examples of porous media flow problems are given to demonstrate the potential of this method. The implementation of the coupling itself is beyond the scope of this thesis and is therefore left to future work.

The chapter is organized as follows. In Section 5.2 we introduce the governing equations for the coupled problem, including the porous medium flow, fluid flow inside the fracture, poroelasticity, and the propagation of the fracture. For illustrative purposes, we limit the discussion to the case of a single crack. But we note that the governing equations are formulated without loss of generality, and can be easily applied to multiple fractures by including the Mode II stress intensity factor calculation and the criterion of local symmetry to allow the cracks to become nonplanar,

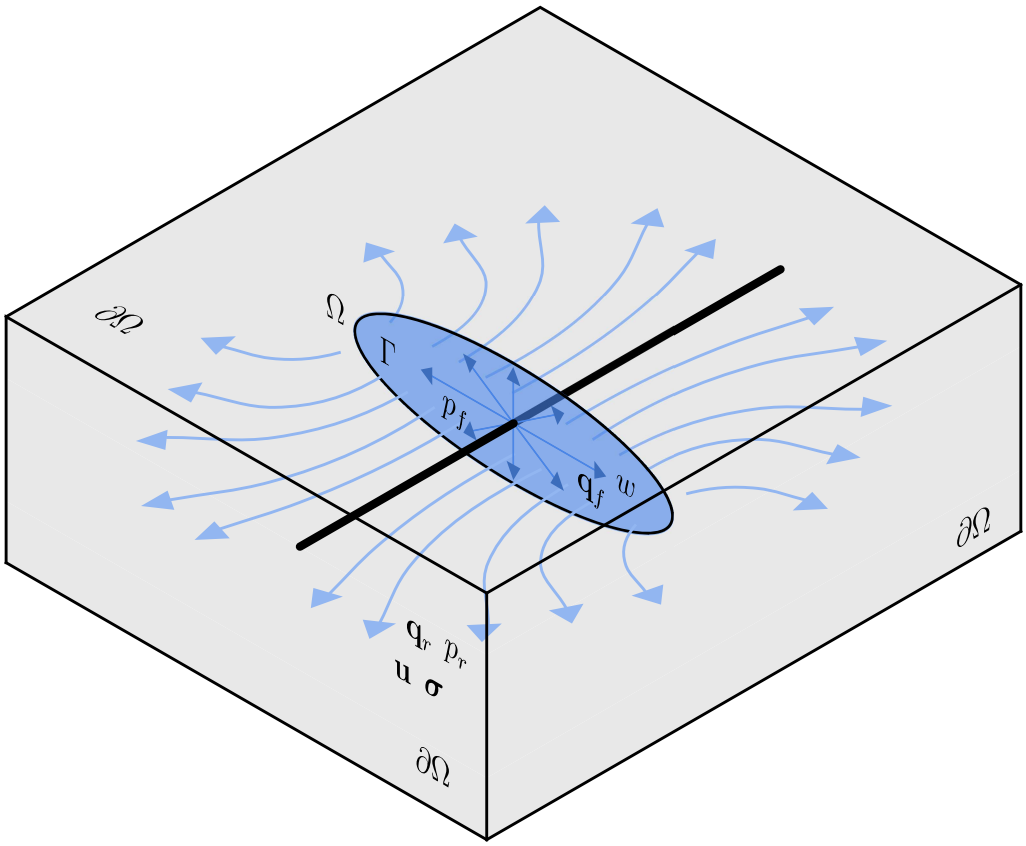

Figure 34: Scheme of porous media flow problem

in addition to the enforcement of flux balance at the wellbore. The computational paradigm for efficient computations of porous medium flow is presented in Section 5.2. The computational efficiency and scaling for a simple case of porous medium flow are given in Section 5.3.1. Section 5.3.2 presents the computational efficiency and scaling for a more complex double porosity-permeability model. Finally, the chapter is summarized in Section 5.4.

5.2 Problem formulation

In this section, we formulate the governing equations for the coupled system of fluid flow in poroelastic medium, fluid flow inside the fracture, and fracture propagation. Figure 34 illustrates a porous domain whose volume is denoted by Ω and

whose boundary is $\partial\Omega$. A set of two-dimensional fracture surfaces in Ω is denoted by Γ. We limit the discussion to the case of a single-phase Newtonian fluid distributed throughout the volume.

The mass balance equation, which repeats the lubrication equation (2.15) in Chapter 2 in a different form, is given by

$$\frac{\partial w}{\partial t} + \nabla_\Gamma \cdot \mathbf{q}_f + q_l = q_{fs} \qquad \text{in } \Gamma, \tag{5.1}$$

$$\mathbf{q}_f = -\frac{w^3}{12\mu}\nabla_\Gamma p_f \qquad \text{in } \Gamma, \tag{5.2}$$

$$\text{and} \quad q_l = -\left(\mathbf{q}_r^- \cdot \mathbf{n}_\Gamma^- + \mathbf{q}_r^+ \cdot \mathbf{n}_\Gamma^+\right) \qquad \text{on } \Gamma, \tag{5.3}$$

where w is the fracture opening, ∇_Γ is the surface divergence, $\mathbf{n}_\Gamma^\pm$ denote the normal to both sides of Γ, $\mathbf{q}_f$ is the fluid flux inside the crack, $\mathbf{q}_r$ is the fluid flux in the porous medium, p_f is the fluid pressure inside the crack, μ is the fluid viscosity, and q_l is the fluid leak-off from the crack into the porous medium.

Next, we introduce the governing equations for a single-phase, slightly compressible fluid in the poroelastic medium (Biot, 1941; Lewis and Schrefler, 1998; Zheng et al., 2003). Considering that $\partial\Omega = \partial_D^f\Omega \bigcup \partial_N^f\Omega$, where $\partial_D^f\Omega$ is Dirichlet boundary, $\partial_N^f\Omega$ is Neumann boundary, the equations read

$$\frac{\partial \zeta}{\partial t} + \nabla \cdot \mathbf{q}_r = q_{rs} \qquad \text{in } \Omega, \tag{5.4}$$

$$\zeta = \alpha \nabla \cdot \mathbf{u} + \frac{p_r}{M} \qquad \text{in } \Omega, \tag{5.5}$$

$$\mathbf{q}_r = -\frac{K}{\mu}\nabla p_r \qquad \text{in } \Omega, \tag{5.6}$$

$$p_r = p_D \qquad \text{on } \partial_D^f\Omega, \tag{5.7}$$

$$\mathbf{q}_r \cdot \mathbf{n} = q_n \qquad \text{on } \partial_N^f\Omega, \tag{5.8}$$

$$\text{and} \quad q_l = -\left(\mathbf{q}_r^- \cdot \mathbf{n}_\Gamma^- + \mathbf{q}_r^+ \cdot \mathbf{n}_\Gamma^+\right) \qquad \text{on } \Gamma, \tag{5.9}$$

where ζ is Biot's increment of fluid mass, q_{rs} is the volumetric source term (added for generality), α is Biot's coefficient, $\mathbf{u}$ is the displacement of the porous medium, p_r is the pore pressure, M is Biot's modulus, K is the permeability tensor, p_D is the prescribed pressure on $\partial\Omega_D$, and q_n is the prescribed normal flux on $\partial\Omega_n$. Equation (5.6) represents Darcy's law.

Assuming the porous domain Ω is elastic and brittle, with $\partial\Omega = \partial^{\sigma}_{D}\Omega \bigcup \partial^{\sigma}_{N}\Omega$, where $\partial^{\sigma}_{D}\Omega$ is the Dirichlet boundary and $\partial^{\sigma}_{N}\Omega$ is the Neumann boundary, the poroelastic stress is written as

$$\boldsymbol{\sigma}^{\text{eff}} = \boldsymbol{\sigma} - \alpha p_r \mathbf{I} \qquad \text{in } \Omega, \tag{5.10}$$

$$-\nabla \cdot \boldsymbol{\sigma} = \mathbf{f} \qquad \text{in } \Omega, \tag{5.11}$$

$$\boldsymbol{\sigma}^{\text{eff}} = \mathbf{A}\mathbf{u} \qquad \text{in } \Omega, \tag{5.12}$$

$$\boldsymbol{\sigma} \cdot \mathbf{n} = \boldsymbol{\tau} \qquad \text{on } \partial^{\sigma}_{N}\Omega, \tag{5.13}$$

$$\mathbf{u} = \mathbf{u_0} \qquad \text{on } \partial^{\sigma}_{D}\Omega, \tag{5.14}$$

$$\text{and} \quad \boldsymbol{\sigma}^{\pm} \cdot \mathbf{n}_{\Gamma^{\pm}} = -p_f \mathbf{n}_{\Gamma^{\pm}} \qquad \text{on } \Gamma, \tag{5.15}$$

where $\mathbf{f}$ denotes the external body force, $\mathbf{A}$ is the linear elastic operator representing Hooke's law, $\boldsymbol{\tau}$ is the prescribed traction, and $\mathbf{u}_0$ is the prescribed displacement. It is worth noting that, when the poroelastic effects are neglected (i.e., $\alpha = 0$), the diffusion zone is much smaller than the fracture size, and the net pressure in the fracture is much smaller than the difference between the *in-situ* stress and initial pore pressure, the reduced equations can be formulated in the integral form (2.6) and (2.8) using the boundary element method and Carter's leak-off, as was done in Chapter 2.

The initial condition for the governing equations can be formulated as

$$\Gamma\big|_{t=0} = \Gamma^0 \qquad \text{in } \Omega, \tag{5.16}$$

$$w\big|_{t=0} = w^0 \qquad \text{on } \Gamma^0, \tag{5.17}$$

$$p_r\big|_{t=0} = p_r^0 \qquad \text{in } \Omega, \tag{5.18}$$

$$\text{and} \quad \boldsymbol{\sigma}\big|_{t=0} = \boldsymbol{\sigma}^0 \qquad \text{in } \Omega, \tag{5.19}$$

where Γ^0 is the fracture surface at $t = 0$, w^0 denotes the initial fracture opening, p_r^0 is the initial pore pressure, and $\boldsymbol{\sigma}^0$ denotes the initial stress.

The fracture opening is related to the displacement by

$$w = \mathbf{u}^+ \cdot \mathbf{n}^+ + \mathbf{u}^- \cdot \mathbf{n}^-. \tag{5.20}$$

Recall that cracks in a brittle medium follow linear elastic fracture mechanics solution, given by

$$w = \sqrt{\frac{32}{\pi}} \frac{K_I}{E'} s^{1/2} \quad \text{on } \Gamma, \quad s \to 0, \tag{5.21}$$

where s is the normal distance inwards from $\partial\Gamma$, and K_I is the Mode I stress intensity factor. The propagation condition is

$$K_I = K_{Ic}, \tag{5.22}$$

where K_{Ic} is the effective fracture toughness of the porous medium.

These governing equations form a coupled system that characterizes fluid flow in porous media, fluid flow inside the cracks, poroelasticity, and crack extension. Fluid flow in the porous medium is formulated as a three-dimensional problem and is,

therefore, typically computed using the finite element method. In the next section, we describe an efficient method for solving the finite element method equations.

5.3 Efficient computation of finite element simulations

Efficient computations of finite element simulations rely on special methods of solving systems of algebraic equations. To ensure efficient simulations of large problems, methods to solve linear or nonlinear systems of equations have to be massively parallel and scalable from the high-performance computing point of view, meaning that the simulation has to run simultaneously on multiple computing units with maximum effectiveness. There are two major types of algebraic solvers for systems of equations: direct solvers and iterative solvers. Parallel direct solvers provide the most accurate results, but they become too slow for large problems. The accuracy of iterative solvers can be adjusted, and they are considered faster than the direct solvers. However, the convergence of iterative solvers depends on the condition number of the system of equations. Neither direct solvers nor simple implementations of iterative solvers may be efficient enough for large scale problems. A good convergence rate for iterative solvers is attained not only by selecting the right solver but also by coupling it with the right preconditioner, which is an operator that changes the condition number of the system of equations.

Modern approaches use a complex technique described next. Often, the matrix corresponding to the system of equations can be split into blocks related to different fields, such as velocity and pressure in the porous media flow problem. Each matrix block may consist of other blocks, forming a nested structure, where the matrix elements are at the bottom level. The blocks of the matrix can be operated with as if they were matrix elements, including applying preconditioners and linear solvers to all levels of the nested block structure. Because the block structure is defined by the

physics of the problem, this approach is called physics-based block solvers (Brown et al., 2012).

The implementation of said methods requires significant programming skills and is, therefore, the prerogative of computer science. Because the finite element method has a great impact when applied to engineering problems, there exist several state-of-the-art scientific libraries for finite element simulations aimed specifically at domain scientists, one of the most popular of which is FEniCS (Alnæs et al., 2015). In particular, FEniCS provides massively parallel and scalable finite element simulations aimed at supercomputers. However, the aforementioned physics based-block solvers are not readily available in FEniCS. For that purpose, a pFibs package was developed as a part of this study, to enable efficient computations of porous media flow problems (Chang et al., 2019). Because of the scientific scope of this manuscript, the implementation details of pFibs software are omitted.

To evaluate the computational performance and scalability of composable block solvers, we use the static-scaling concept (Brown, 2016; Chang et al., 2018). First, it is necessary to introduce the following definitions. Degrees of freedom (Dofs) denote the total number of unknowns in the discretized problem. The computational rate is defined as degrees of freedom divided by the time spent on computations. It effectively shows the number of unknowns solved per unit time, being the measure of efficiency. In the static-scaling concept, the number of computational units is kept constant, while the problem size changes. Given this, the computational rate is plotted on the vertical axis vs the degrees of freedom on the horizontal axis. The purpose of this plot is to compare the efficiency of computations for different problem sizes. For example, large problems use a lot of memory. Therefore the computational rate is expected to go down at some point along the horizontal axis due to the limit on available memory. For small problems, which are located at the beginning of the horizontal axis, the

computational rate is also expected to be low, because of the so-called overhead. The overhead refers to all the processes necessary for the simulation to run, but that are not directly related to solving the system of equations. Somewhere between these two limiting cases, the computational rate reaches its maximum. The whole curve on the static scaling plot is used to evaluate the computational performance of the model. In particular, the performance is defined not only by the maximum computational rate but also by the width of the peak that defines positions of the left and the right boundaries that outline the region of highly efficient computations.

5.3.1 Porous media flow problem

In this section, we demonstrate the use of block solvers to model problems of flow in porous media. The purpose of the following discussion is to demonstrate the computational efficiency and scaling of the method. Therefore, to simplify complexity, we ignore the poroelastic coupling and focus solely on the flow problem.

We consider the use of block solvers and preconditioners to solve the mixed Poisson problem. First, we introduce the governing equations. Then, we describe the corresponding block structure of the arising system of equations and the solving strategy. In particular, block solvers and preconditioners are used. Finally, we show the computational efficiency and scalability of this approach in parallel computations.

Governing equations. The governing equations for the porous media flow problem can be written as

$$\frac{\mu}{K}\mathbf{q}_r + \nabla p_r = 0 \qquad \text{in } \Omega, \tag{5.23}$$

$$\frac{1}{M}\frac{\partial p_r}{\partial t} + \nabla \cdot \mathbf{q}_r = q_{rs}, \qquad \text{in } \Omega, \tag{5.24}$$

$$p_r = p_D \qquad \text{on } \partial^f_D\Omega, \tag{5.25}$$

$$\mathbf{q}_r \cdot \mathbf{n} = q_n \qquad \text{on } \partial^f_N\Omega, \tag{5.26}$$

$$q_l = -\left(\mathbf{q}_r^- \cdot \mathbf{n}_\Gamma^- + \mathbf{q}_r^+ \cdot \mathbf{n}_\Gamma^+\right) \qquad \text{on } \Gamma, \tag{5.27}$$

$$\text{and} \quad p_r\big|_{t=0} = p_r^0 \qquad \text{in } \Omega. \tag{5.28}$$

The time derivative in equation (5.24) is discretized using the backward Euler scheme. In what follows next, we consider the solution of the governing equations for one time step of size Δt.

Block structure. First, to emphasize the block structure of the problem, we denote the solution vector as

$$\mathbf{w} = \left(\begin{array}{c} \mathbf{q}_r \\ \hline p_r \end{array}\right). \tag{5.29}$$

The governing equations (5.23)-(5.28) are then formulated as

$$\left(\begin{array}{c|c} \frac{\mu}{K}\mathbf{I} & \nabla \\ \hline \nabla\cdot & \frac{1}{M\Delta t} \end{array}\right)\mathbf{w} = \left(\begin{array}{c} 0 \\ \hline q_{rs} + \frac{p_r^0}{M\Delta t} \end{array}\right). \tag{5.30}$$

where the horizontal and vertical lines are drawn to separate blocks.

Next, we describe the Schur complement approach, which is typically used for the solution of block problems. For a block problem consisting of two-by-two blocks,

which can be represented by

$$\begin{pmatrix} A & B \\ C & D \end{pmatrix} \begin{pmatrix} x_1 \\ x_2 \end{pmatrix} = \begin{pmatrix} f_1 \\ f_2 \end{pmatrix}, \tag{5.31}$$

the Schur complement approach utilizes the following factorization

$$\begin{pmatrix} A & B \\ C & D \end{pmatrix} = \begin{pmatrix} I & 0 \\ CA^{-1} & I \end{pmatrix} \begin{pmatrix} A & 0 \\ 0 & S \end{pmatrix} \begin{pmatrix} I & A^{-1}B \\ 0 & I \end{pmatrix}, \tag{5.32}$$

where

$$S = D - CA^{-1}B \tag{5.33}$$

is referred to as Schur complement. The Schur complement approach reduces the problem of inverting the full matrix to the problem of inverting two blocks, A and S, since the inverse of (5.32) is

$$P = \begin{pmatrix} I & -A^{-1}B \\ 0 & I \end{pmatrix} \begin{pmatrix} A^{-1} & 0 \\ 0 & S^{-1} \end{pmatrix} \begin{pmatrix} I & 0 \\ -CA^{-1} & I \end{pmatrix}. \tag{5.34}$$

Expression (5.34) is applied as a preconditioner to the linear system (5.30), to obtain the first approximation of the flux and pressure fields. Here, A is the mass matrix $\frac{\mu}{K}\mathbf{I}$, and we are interested in its inverse of A, which can be approximately computed. The matrix S has the following form

$$S = \frac{1}{M\Delta t} - \nabla \cdot \left(\frac{\mu}{K}\mathbf{I}\right)^{-1} \nabla, \tag{5.35}$$

where the inversion of $\frac{\mu}{K}\mathbf{I}$ yields a dense matrix, rendering the related matrix multiplication costly. To resolve this we adopt an approximation to $\left(\frac{\mu}{K}\mathbf{I}\right)^{-1}$, which uses

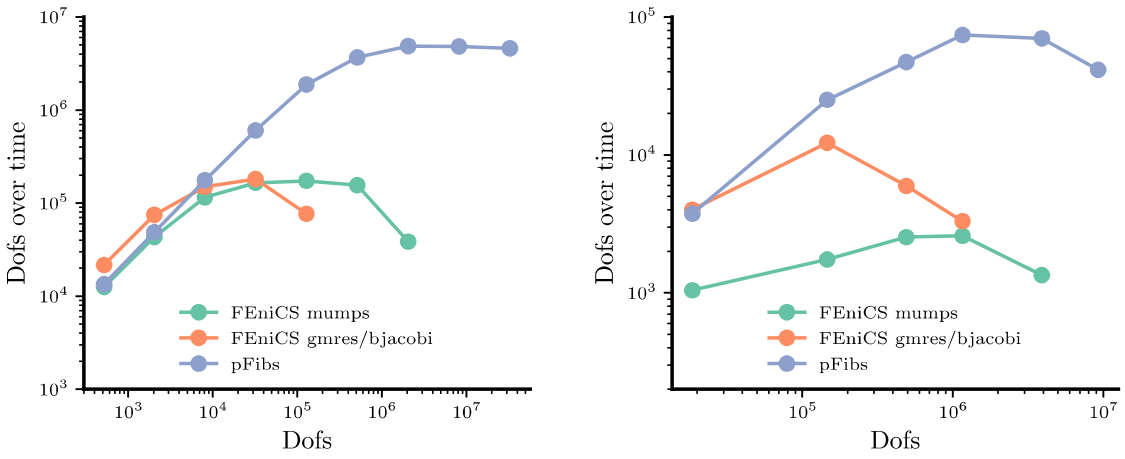

(a) Static scaling for 2D mixed Poisson problem.

(b) Static scaling for 3D mixed Poisson problem.

Figure 35: Static scaling plots for mixed Poisson problem on a unit square (a) or a unit cube (b) domains. FEniCS default solvers are compared with pFibs solver with Schur factorization.

the inverse diagonal of A resulting in

$$\tilde{S} = \frac{1}{M\Delta t} - \nabla \cdot \mathrm{diag}\left(\frac{\mu}{K}\mathbf{I}\right)^{-1} \nabla. \tag{5.36}$$

Next, $\tilde{S}^{-1}$ is calculated using the approximate algorithm.

Computational efficiency and scalability. The numerical results were computed using the finite element method with FEniCS (Alnæs et al., 2015) and pFibs (Chang et al., 2019). We considered the 2D case on a unit square and the 3D case in a unit cube. The computations were run on a node with 96 GB of memory and dual Intel Xeon Gold Skylake 6154 (3.0 GHz, 18-core) processors with 36 processing units in total. To understand the performance of the computations, we use the static-scaling concept described in Section 5.3.

The 2D problem had the following number of finite element nodes along each dimension: [10, 20, 40, 80, 160, 320, 640, 1280, 2560]. The corresponding number of

degrees of freedom was equal to: [520, 2040, 8080, 32160, 128320, 512640, 2049280, 8194560, 32773120]. The Schur complement approach was compared to MUltifrontal Massively Parallel sparse direct Solver (MUMPS) (Amestoy et al., 2000), based on the Gaussian elimination, and an iterative solver, denoted by gmres/bjacobi (Balay et al., 2019). The static scaling plot, presented in Figure 35a, shows that the Schur complement approach has a much higher maximum computational rate and also the curve becomes horizontal, meaning that the amount of available memory is greater than required for this approach even for large problem sizes. The direct solver MUMPS clearly reaches memory limitation as the problem size increases, and its line curves down. While the gmres/bjacobi iterative solver is supposed to conserve memory, it's performance is worsened by poor convergence. Therefore its maximum computational rate is much lower than that of the Schur complement approach. In addition, the gmres/bjacobi line also curves down, and eventually, the algorithm stops converging. The Schur complement approach conserves memory and keeps a good convergence rate due to the effective preconditioning of the system. The difference between the computational rate between the Schur complement approach and the direct solver MUMPS is negligible for small problem sizes, but increases by almost two orders of magnitude before MUMPS reaches memory limit.

The 3D problem had the following number of nodes along each dimension: [10, 15, 20, 30, 40, 80, 160]. The number of degrees of freedom was equal to: [18600, 62100, 146400, 491400, 1161600, 9254400, 73881600]. The comparison used the same solvers as in the 2D case: MUMPS, gmres/bjacobi, and the Schur complement block solver. The performance of the solvers, presented in the static scaling plot 35b, is similar to the 2D case: the Schur complement approach has a better performance than the other solvers because it conserves memory and preconditions the system. However, the computational rate of all methods is less than in the 2D case, because of the

more complex 3D structure of the problem. The Schur complement approach curve shows memory-related effects on the right side of the plot. The direct solver MUMPS performs worse than the Schur complement approach even for small problems.

This comparison demonstrates that the physical block solver is much more computationally efficient than the direct solver for this formulation of porous media flow problem. The next section will consider a more complex case of flow in porous media. Specifically, we consider the double porosity-permeability problem.

5.3.2 Double porosity-permeability problem

In this section, we consider the double porosity-permeability (DPP) model (Nakshatrala et al., 2018), which describes the flow of incompressible fluid in a porous medium with two pore-networks and mass transfer between them. The need to model different scales of porous networks and the interaction between them may arise in reservoir simulation. The resulting mathematical model has four-fields: macro velocity-pressure and micro velocity-pressure, for which this section demonstrates the use of nested block solvers and preconditioners. The block solver technique is especially important for many-field formulations with complex block structure such as the DPP model. We start by introducing the governing equations. The block structure of the arising system of equations and the solving strategy is described next. Finally, the scalability results are presented.

Governing equations. The primary goal of this section is to show the advantages of the block solver technique in many-field formulations with complex block structure such as the DPP model. Because the block structure of the transient problem is similar to that of the steady-state problem, we limit our analysis to the steady-state case.

The macro scale is denoted by subscript 1, the micro scale - by subscript 2. The

porous medium domain is denoted by Ω. The macro-scale pressure and Darcy velocity fields are denoted by p_{r1} and $\mathbf{q}_{r1}$ and the micro-scale fields are denoted by p_{r2} and $\mathbf{q}_{r2}$, respectively. The governing equations for a steady-response under the DPP model are

$$\frac{\mu}{K_1}\mathbf{q}_{r1} + \nabla p_{r1} = 0 \qquad \text{in } \Omega, \tag{5.37}$$

$$\frac{\mu}{K_2}\mathbf{q}_{r2} + \nabla p_{r2} = 0 \qquad \text{in } \Omega, \tag{5.38}$$

$$\nabla \cdot \mathbf{q}_{r1} = -\frac{\beta}{\mu}\left(p_{r1} - p_{r2}\right) + q_{rs1} \qquad \text{in } \Omega, \tag{5.39}$$

$$\text{and} \quad \nabla \cdot \mathbf{q}_{r2} = +\frac{\beta}{\mu}\left(p_1 - p_2\right) + q_{rs2} \qquad \text{in } \Omega, \tag{5.40}$$

where μ is the fluid viscosity, K_1 and K_2 are the (isotropic) permeabilities of the macro-scale and micro-scale pore networks, and β is a dimensionless characteristic of the porous medium. The equations above take into account the mass transfer per unit volume between the macro-scale and the micro-scale pore networks.

$$\chi = -\frac{\beta}{\mu}\left(p_{r1} - p_{r2}\right). \tag{5.41}$$

Considering the domain boundary $\partial\Omega = \Gamma_1^p \bigcup \Gamma_2^p \bigcup \Gamma_1^u \bigcup \Gamma_2^u$, boundary conditions for (5.37)-(5.40) are

$$p_{r1} = p_{01} \qquad \text{on } \Gamma_1^p, \tag{5.42}$$

$$p_{r2} = p_{02} \qquad \text{on } \Gamma_2^p, \tag{5.43}$$

$$\mathbf{q}_{r1} \cdot \mathbf{n} = q_{n1} \qquad \text{on } \Gamma_1^q, \tag{5.44}$$

$$\text{and} \quad \mathbf{q}_{r2} \cdot \mathbf{n} = q_{n2} \qquad \text{on } \Gamma_2^q, \tag{5.45}$$

where p_{01} and p_{02} are prescribed pressure fields on the boundaries Γ_1^p and Γ_2^p, $\mathbf{n}$

denotes the outward normal to the boundary, and q_{n1} and q_{nw} are prescribed normal components of Darcy velocities on the boundaries Γ_1^q and Γ_2^q.

Block structure. The DPP model cannot be reformulated in single-field Poisson form (Joshaghani et al., 2019). We consider grouping the fields using the scale-split, with the solution vector

$$\mathbf{w} = \left(\begin{array}{c} \mathbf{q}_{r1} \\ p_{r1} \\ \hline \mathbf{q}_{r2} \\ p_{r2} \end{array}\right). \tag{5.46}$$

The corresponding block structure of governing equations (5.37)-(5.40) is

$$\left(\begin{array}{cc|cc} \frac{\mu}{K_1}\mathbf{I} & \nabla & \mathbf{0} & 0 \\ \nabla\cdot & \frac{\beta}{\mu} & \mathbf{0} & -\frac{\beta}{\mu} \\ \hline \mathbf{0} & 0 & \frac{\mu}{K_2}\mathbf{I} & \nabla \\ \mathbf{0} & -\frac{\beta}{\mu} & \nabla\cdot & \frac{\beta}{\mu} \end{array}\right) \cdot \mathbf{w} = \left(\begin{array}{c} 0 \\ q_{rs1} \\ \hline 0 \\ q_{rs2} \end{array}\right). \tag{5.47}$$

The system (5.47) is preconditioned with so-called multiplicative fieldsplit preconditioner (Balay et al., 2019), in which the preconditioners for each block are applied sequentially to the residual. Then, the linear solver gmres (Balay et al., 2019) solves the system. The blocks corresponding to each scale are preconditioned using Schur factorization (5.32), where

$$\begin{pmatrix} A_i & B_i \\ C_i & D_i \end{pmatrix} = \left(\begin{array}{c|c} \frac{\mu}{K_i}\mathbf{I} & \nabla \\ \hline \nabla\cdot & \frac{\beta}{\mu} \end{array}\right), \quad i = 1, 2. \tag{5.48}$$

Since $\left(\frac{\mu}{K_i}\mathbf{I}\right)^{-1}$ are dense, the approximation of S_i is calculated as

$$\tilde{S}_i = \frac{\beta}{\mu} - \nabla \cdot \operatorname{diag}\left(\frac{\mu}{K_i}\mathbf{I}\right)^{-1} \nabla. \tag{5.49}$$

The action of A_i^{-1} and $\tilde{S}_i^{-1}$ in equation (5.34) are computed with bjacobi and hypre algebraic multigrid (Balay et al., 2019) respectively.

Computational efficiency and scalability. This goal of this section is to show the efficiency of the block solver approach on systems with small memory. The numerical results were computed using the finite element method on a unit square (2D) and in a unit cube (3D) with FEniCS (Alnæs et al., 2015) and pFibs (Chang et al., 2019). The computations were run on a laptop with 8 GB of memory and dual-core Intel Core i5 with two processing units in total. We additionally provide the results computed with the algorithm for DPP used in (Joshaghani et al., 2019), where the block solvers were used with Firedrake (Rathgeber et al., 2016). The performance of the computations is analyzed using the static-scaling concept described in Section 5.3.

The number of nodes in each dimension for the 2D unit square was: [100, 150, 200, 250, 350, 400, 600, 800]. The number of degrees of freedom was: [100400, 225600, 400800, 626000, 1226400, 1601600, 3602400, 6403200]. For 3D unit cube, the number of nodes in each dimension: [10, 15, 20, 30, 40, 50, 60], and total number of degrees of freedom: [37200, 124200, 292800, 982800, 2323200, 4530000, 7819200]. The static scaling plots, presented in Figure 36, show the performance of the block solver approach described in the previous section. The performance of the direct solver is known to be poor when the memory is small, and the problem size is large. Therefore, it is not presented in the plots. The computational rates corresponding to the block solvers approach implemented in FEniCS and Firedrake are reasonably stable for large problems. In particular, the performance remains high even for large problems, and, as was mentioned, the simulations were run on a system with only 8 GB of memory. This proves that the block solver approach is highly efficient for large simulations on systems with small memory. The difference in computational rate between one and two processing units seems small on the plots due to the logarithmic

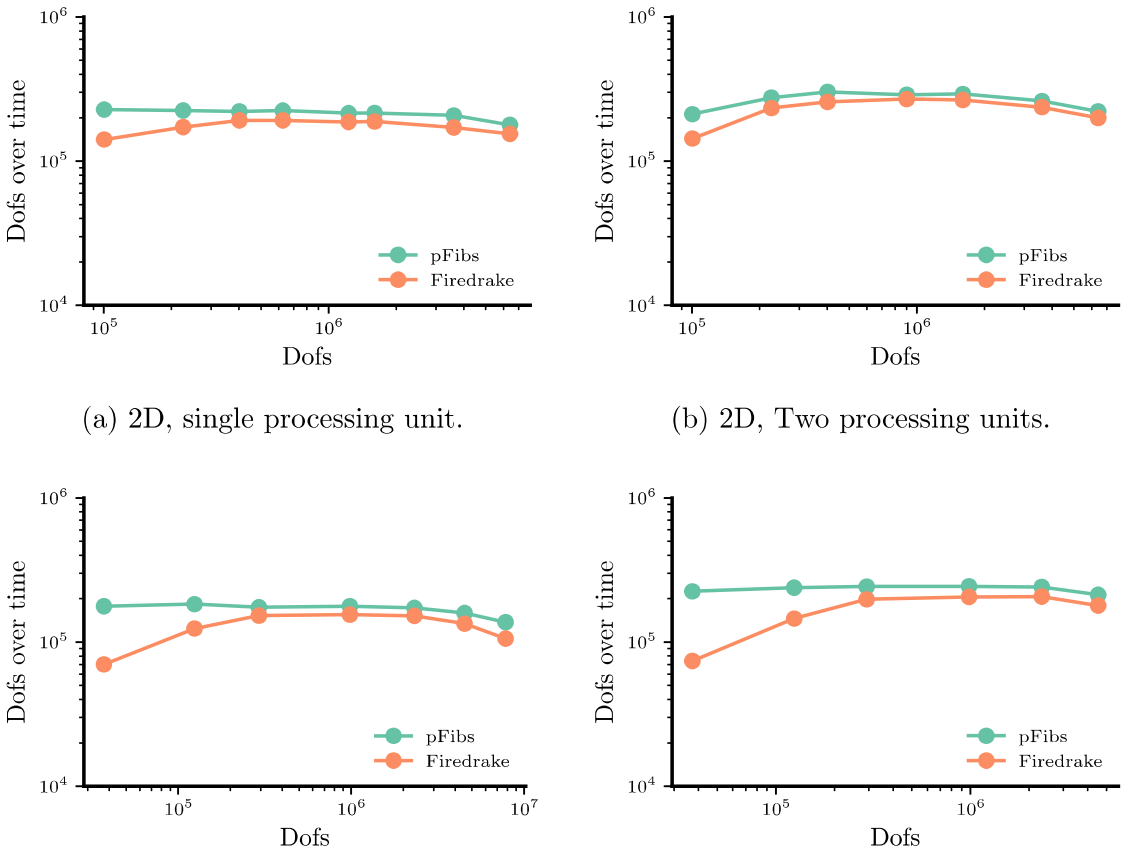

(a) 2D, single processing unit.

(b) 2D, Two processing units.

(c) 3D, single processing unit.

(d) 3D, Two processing units.

Figure 36: Static scaling plots for double porosity-permeability problem on a unit square (a, b) or cube (c, d) for 1 and 2 MPI threads. The results were obtained with Firedrake and FEniCS/pFibs block solvers.

scale, but the ratio is actually close to two. This shows that parallel computations on many processing units can efficiently accelerate the computations even on small systems, assuming the block solver approach is applied to finite element simulations for porous media flow.

5.4 Summary

In this chapter, we introduced a method for further extension of the reduced-order models for hydraulic fracture, described in Chapter 3 and 4, by coupling them with fluid flow in porous media. The motivation for such coupling stems from the

limited applicability of Carter's leak-off law used in the reduced-order models, and, additionally, from the interest to the physics of porous medium flow during the production stage of reservoir stimulation. Because 3D simulation of porous medium flow can become a bottleneck in the coupled model, the investigation of related acceleration methods is crucial. We described a computational paradigm that accelerates the numerical solutions of porous media flow problems, which in future work can be coupled with the reduced-order hydraulic fracturing models to create an efficient and physically realistic hydraulic fracture simulator. Several finite element models were constructed for the governing equations for porous media flow arising in reservoir simulation. The state-of-the-art acceleration technique was applied to the said finite element models using the developed software package pFibs and scientific framework FEniCS. The result showed high computational efficiency and scalability of this approach over the regular methods, which makes it a viable candidate for the coupled model. The implementation of the coupled model is left to future work.

6 Conclusions

6.1 Main contributions

The main contributions of this study are summarized as:

1. The analysis of different approaches to efficient and relatively accurate approximations of the elasticity relation that represent the propagation of a crack in an elastic medium has been performed. Those include the local elasticity as in the classical PKN models and the non-local elasticity, as in the enhanced PKN and the 2D DDM model. It is shown that the enhanced PKN approach is the most accurate.

2. A procedure for approximate calculation of elastic interactions between multiple fractures has been introduced. The procedure extends the non-local elasticity approach of the enhanced PKN model, which was formulated for a single fracture. The new formulation adds normal and shear stress components, as well as out-of-plane configurations necessary for multiple cracks in 3D. The accuracy of the method is shown by comparisons with the reference model ILSA.

3. A reduced order model for multiple planar blade-like hydraulic fractures, referred to as mEPKN, has been developed. The mEPKN model combines the plane strain approximation of the enhanced PKN model with the developed approximate elasticity relation. Compared to the enhanced PKN model, mEPKN is aimed at multiple hydraulic fractures and also considers wellbore fluid balance. The obtained solution has been validated against the reference model ILSA (Peirce and Detournay, 2008; Dontsov and Peirce, 2017) for the case of five uniformly spaced parallel fractures and covering toughness K, viscosity M, and mixed propagation regimes. The mEPKN model shows good agreement

with the reference results for most cases. The inaccuracy in the calculation of flux distribution in the low perforation friction case has been identified.

4. A procedure for the accurate evaluation of fluid pressure near the wellbore has been derived. The procedure considers the correct singularity of the fluid pressure at the injection point, which is used in the wellbore fluid balance calculation. The comparison with the reference solution shows that the "pressure correction" results in significantly more accurate flux distribution.

5. A reduced order model for multiple non-planar hydraulic fractures, referred to as mEP3D, has been developed. The mEP3D model is based on the mEPKN model and the enhanced pseudo-3D model. The mEP3D addresses the following limitations of mEPKN: inability to model height growth, inability to model non-planar fracture, inaccurate wellbore fluid balance calculation, inability to model hydraulic fracture at early times, and no fluid leak-off. The mEP3D model has been validated against the reference model ILSA for five equally spaced planar hydraulic fractures in K, M, $\tilde{K}$, $\tilde{M}$, and mixed propagation regimes. The fracture turning has been compared to the analytical predictions for the case of plane strain hydraulic fracture.

6. The multi-scale asymptotic solution for the near-tip region of a hydraulic fracture has been implemented for a non-planar fracture geometry.

7. Analysis of multiple hydraulic fractures propagating in different regimes under the condition of limited entry has been performed. It is shown that the fracture growth pattern is unstable in the toughness regime, whereby some fractures grow in one direction, while others grow in the opposite direction. At the same time, all generated fractures are nearly identical in the viscosity dominated regime.

8. A computationally efficient method for simulating flow in porous media has been presented. The method uses the existing state-of-the-art techniques in numerical methods and computer science, provided by well-established scientific libraries. A software package pFibs (Chang et al., 2019) has been developed to enable the said techniques for the porous media flow problem. It is shown that the three-dimensional porous media flow model can be significantly accelerated to be considered for coupling with the reduced-order hydraulic fracture models.

6.2 Future work

We suggest the following topics for future work that expand the results of this research:

1. The current model is based on the plane strain solution for a fracture inside three symmetric stress layers. In order to model multiple layers of confining stress, typically observed during hydraulic fracturing treatment, the mEP3D model has to modified by replacing the plane strain approximation of the fracture opening with the general expression for multiple stress layers and additionally deriving all the related approximations.

2. The coupling between the hydraulic fracture model with the porous media flow has been done in the past. In this study, it has been shown that the coupling between the fast hydraulic fracture models and the three-dimensional porous media flow model can be considered if the flow model is accelerated via the state-of-the-art computational techniques. As a logical step, the implementation of the coupling itself can be accomplished, combining hydraulic fracture modeling, high-performance computing, and computer science fields.

Bibliography

Abe, H., Keer, L. M., and Mura, T. (1976). Growth rate of a penny-shaped crack in hydraulic fracturing of rocks, 2. *Journal of Geophysical Research*, 81(35):6292–6298.

Abou-Sayed, A. S., Andrews, D. E., and Buhidma, I. M. (1989). Evaluation of oily waste injection below the permafrost in Prudhoe Bay field. In *Proceedings of the California Regional Meetings*, pages 129–142. Society of Petroleum Engineers.

Adachi, J., Siebrits, E., Peirce, A., and Desroches, J. (2007). Computer simulation of hydraulic fractures. *International Journal of Rock Mechanics and Mining Sciences*, 44:739–757.

Adachi, J. I. and Detournay, E. (2002). Self-similar solution of a plane-strain fracture driven by a power-law fluid. *International Journal for Numerical and Analytical Methods in Geomechanics*, 26:579–604.

Adachi, J. I. and Detournay, E. (2008). Plane-strain propagation of a hydraulic fracture in a permeable rock. *Engineering Fracture Mechanics*, 75:4666–4694.

Adachi, J. I., Detournay, E., and Peirce, A. P. (2010). Analysis of the classical pseudo-3D model for hydraulic fracture with equilibrium height growth across stress barriers. *International Journal of Rock Mechanics and Mining Sciences*, 47(4):625–639.

Adachi, J. I. and Peirce, A. P. (2008). Asymptotic analysis of an elasticity equation for a finger-like hydraulic fracture. *Journal of Elasticity*, 90(1):43–69.

Alnæs, M. S., Blechta, J., Hake, J., Johansson, A., Kehlet, B., Logg, A., Richardson, C., Ring, J., Rognes, M. E., and Wells, G. N. (2015). The fenics project version 1.5. *Archive of Numerical Software*, 3(100).

Amestoy, P. R., Duff, I. S., and L'excellent, J.-Y. (2000). Multifrontal parallel distributed symmetric and unsymmetric solvers. *Computer Methods in Applied Mechanics and Engineering*, 184(2-4):501–520.

Balay, S., Abhyankar, S., Adams, M., Brown, J., Brune, P., Buschelman, K., Dalcin, L., Dener, A., Eijkhout, V., Gropp, W., Karpeyev, D., Kaushik, D., Knepley, M., May, D., Curfman McInnes, L., Mills, R., Munson, T., Rupp, K., Sanan, P., Smith, B., Zampini, S., Zhang, H., and Zhang, H. (2019). Petsc users manual. Argonne National Laboratory.

Baykin, A. and Golovin, S. (2018). Application of the fully coupled planar 3D poroelastic hydraulic fracturing model to the analysis of the permeability contrast impact on fracture propagation. *Rock Mechanics and Rock Engineering*, 51:3205–3217.

Bessmertnykh, A. O. and Dontsov, E. V. (2019). A semi-infinite hydraulic fracture driven by a Herschel-Bulkley fluid. *Journal of Applied Mechanics*, 86(12):121008.

Biot, M. A. (1941). General theory of three-dimensional consolidation. *Journal of Applied Physics*, 12(2):155–164.

Boone, T. and Ingraffea, A. (1990). A numerical procedure for simulation of hydraulically-driven fracture propagation in poroelastic media. *International Journal for Numerical and Analytical Methods in Geomechanics*, 14:27–47.

Boone, T., Ingraffea, A., and Roegiers, J. (1991). Simulation of hydraulic fracture propagation in poroelastic rock with application to stress measurement techniques. *International Journal of Rock Mechanics and Mining Sciences*, 28:1–14.

Brown, D. W. (2000). A hot dry rock geothermal energy concept utilizing supercritical CO_2 instead of water. In *Proceedings of the 25th Workshop on Geothermal Reservoir Engineering Stanford University, Stanford, California.*

Brown, J. (2016). Threading tradeoffs in domain decomposition. *SIAM Parallel Processing Conference, To Thread or Not To Thread Minisymposium.*

Brown, J., Knepley, M. G., May, D. A., McInnes, L. C., and Smith, B. (2012). Composable linear solvers for multiphysics. In *Proceedings of the 11th International Symposium on Parallel and Distributed Computing*, pages 55–62.

Bunger, A. P. and Detournay, E. (2007). Early time solution for a penny-shaped hydraulic fracture. *Journal of Engineering Mechanics*, 133:175–190.

Bunger, A. P., Detournay, E., and Garagash, D. I. (2005). Toughness-dominated hydraulic fracture with leak-off. *International Journal of Fracture*, 134(2):175–190.

Carter, E. D. (1957). Optimum fluid characteristics for fracture extension. In Howard, G. C. and Fast, C. R., editors, *Drilling and production practices*, pages 261–270.

Chang, J., Allen, J., and Protasov, I. (2019). PFIBS: A parallel FEniCS implementation of block solvers. `https://github.com/NREL/pfibs`.

Chang, J., Nakshatrala, K. B., Knepley, M. G., and Johnsson, L. (2018). A performance spectrum for parallel computational frameworks that solve pdes. *Concurrency and Computation: Practice and Experience*, 30(11):e4401.

Chen, Z. (2013). An ABAQUS implementation of the XFEM for hydraulic fracture problems. In *Proceedings of ISRM International Conference for Effective and Sustainable Hydraulic Fracturing*. International Society for Rock Mechanics and Rock Engineering.

Chukwudozie, C., Bourdin, B., and Yoshioka, K. (2019). A variational phase-field model for hydraulic fracturing in porous media. *Computer Methods in Applied Mechanics and Engineering*, 347:957 – 982.

Cotterell, B. and Rice, J. R. (1980). Slightly curved or kinked cracks. *International Journal of Fracture*, 16(2):155–169.

Cramer, D. D. (1987). The application of limited-entry techniques in massive hydraulic fracturing treatments. In *Proceedings of SPE Production Operations Symposium*. Society of Petroleum Engineers.

Crouch, S. L. and Starfield, A. M. (1983). *Boundary element methods in solid mechanics*. George Allen & Unwin, London.

Crump, J. B. and Conway, M. W. (1988). Effects of perforation-entry friction on bottomhole treating analysis. *Journal of Petroleum Technology*, 40(08):1–041.

Damjanac, B. and Cundall, P. (2016). Application of distinct element methods to

simulation of hydraulic fracturing in naturally fractured reservoirs. *Computers and Geotechnics*, 71:283–294.

Damjanac, B., Detournay, C., Cundall, P. A., and Varun. (2013). Three-dimensional numerical model of hydraulic fracturing in fractured rock mass. In Bunger, A. P., McLennan, J., and Jeffrey, R., editors, *Effective and Sustainable Hydraulic Fracturing*, chapter 41, pages 819–830. Intech.

Desroches, J., Detournay, E., Lenoach, B., Papanastasiou, P., Pearson, J. R. A., Thiercelin, M., and Cheng, A. (1994). The crack tip region in hydraulic fracturing. *Proceedings of the Royal Society of London. Series A: Mathematical and Physical Sciences*, 447(1929):39–48.

Detournay, E. (2004). Propagation regimes of fluid-driven fractures in impermeable rocks. *International Journal of Geomechanics*, 4(1):35–45.

Detournay, E. (2016). Mechanics of hydraulic fractures. *Annual Review of Fluid Mechanics*, 48:311–339.

Detournay, E. and Garagash, D. I. (2003). The near-tip region of a fluid-driven fracture propagating in a permeable elastic solid. *Journal of Fluid Mechanics*, 494:1–32.

Detournay, E. and Peirce, A. (2014). On the moving boundary conditions for a hydraulic fracture. *International Journal of Engineering Science*, 84:147–155.

Dontsov, E., Bunger, A., Abell, B., and Suarez-Rivera, R. (2019). Ultrafast hydraulic

fracturing model for optimizing cube development. In *Proceedings of Unconventional Resources Technology Conference*.

Dontsov, E. V. (2016). An approximate solution for a penny-shaped hydraulic fracture that accounts for fracture toughness, fluid viscosity and leak-off. *Royal Society Open Science*, 3(12):160737.

Dontsov, E. V. (2017). An approximate solution for a plane strain hydraulic fracture that accounts for fracture toughness, fluid viscosity, and leak-off. *International Journal of Fracture*, 205(2):221–237.

Dontsov, E. V. and Kresse, O. (2018). A semi-infinite hydraulic fracture with leak-off driven by a power-law fluid. *Journal of Fluid Mechanics*, 837:210–229.

Dontsov, E. V. and Peirce, A. P. (2015a). An enhanced pseudo-3D model for hydraulic fracturing accounting for viscous height growth, non-local elasticity, and lateral toughness. *Engineering Fracture Mechanics*, 142:116–139.

Dontsov, E. V. and Peirce, A. P. (2015b). Incorporating viscous, toughness, and intermediate regimes of propagation into enhanced pseudo-3D model. In *Proceedings of the 49th US Rock Mechanics/Geomechanics Symposium*. American Rock Mechanics Association.

Dontsov, E. V. and Peirce, A. P. (2015c). A non-singular integral equation formulation to analyse multiscale behaviour in semi-infinite hydraulic fractures. *Journal of Fluid Mechanics*, 781:R1.

Dontsov, E. V. and Peirce, A. P. (2016a). Comparison of toughness propagation criteria for blade-like and pseudo-3D hydraulic fractures. *Engineering Fracture Mechanics*, 160:238–247.

Dontsov, E. V. and Peirce, A. P. (2016b). Implementing a universal tip asymptotic solution into an implicit level set algorithm (ILSA) for multiple parallel hydraulic fractures. In *Proceedings of the 50th US Rock Mechanics/Geomechanics Symposium*. American Rock Mechanics Association.

Dontsov, E. V. and Peirce, A. P. (2017). A multiscale implicit level set algorithm (ILSA) to model hydraulic fracture propagation incorporating combined viscous, toughness, and leak-off asymptotics. *Computer Methods in Applied Mechanics and Engineering*, 313:53–84.

Dontsov, E. V. and Suarez-Rivera, R. (2020). Propagation of multiple hydraulic fractures in different regimes. *International Journal of Rock Mechanics and Mining Sciences*, 128:104270.

Economides, M. J. and Nolte, K. G., editors (2000). *Reservoir Stimulation*. John Wiley & Sons, Chichester, UK, 3rd edition.

El-Rabaa, A. M., Shah, S. N., and Lord, D. L. (1997). New perforation pressure loss correlations for limited entry fracturing treatments. In *Procedings of SPE Rocky Mountain Regional Meeting*. Society of Petroleum Engineers.

Erdogan, F. and Sih, G. (1963). On the crack extension in plates under plane loading and transverse shear. *Journal of Basic Engineering*, 85(4):519–525.

Garagash, D. and Detournay, E. (2000). The tip region of a fluid-driven fracture in an elastic medium. *Journal of Applied Mechanics*, 67(1):183–192.

Garagash, D. and Detournay, E. (2005). Plane-strain propagation of a fluid-driven fracture: Small toughness solution. *Journal of Applied Mechanics*, 72:916–928.

Garagash, D. I. (2006). Plane-strain propagation of a fluid-driven fracture during injection and shut-in: Asymptotics of large toughness. *Engineering Fracture Mechanics*, 73:456–481.

Garagash, D. I., Detournay, E., and Adachi, J. I. (2011). Multiscale tip asymptotics in hydraulic fracture with leak-off. *Journal of Fluid Mechanics*, 669:260–297.

Geertsma, J. and De Klerk, F. (1969). A rapid method of predicting width and extent of hydraulically induced fractures. *Journal of Petroleum Technology*, 21(12):1–571.

Gordeliy, E., Abbas, S., and Peirce, A. (2019). Modeling nonplanar hydraulic fracture propagation using the XFEM: An implicit level-set algorithm and fracture tip asymptotics. *International Journal of Solids and Structures*, 159:135–155.

Gordeliy, E. and Peirce, A. P. (2013). Implicit level set schemes for modeling hydraulic fractures using the XFEM. *Computer Methods in Applied Mechanics and Engineering*, 266:125–143.

Gottschling, J. C. et al. (2010). Marcellus net fracturing pressure analysis. In *Proceedings of SPE Eastern Regional Meeting*. Society of Petroleum Engineers.

Hills, D. A., Kelly, P. A., Dai, D. N., and Korsunsky, A. M. (1996). *Solution of crack*

problems, the distributed dislocation technique, solid mechanics and its applications, volume 44. Kluwer Academic Publisher, Dordrecht.

Hu, J. and Garagash, D. I. (2010). Plane-strain propagation of a fluid-driven crack in a permeable rock with fracture toughness. *Journal of Engineering Mechanics*, 136:1152–1166.

Jeffrey, R. G. and Bunger, A. P. (2007). A detailed comparison of experimental and numerical data on hydraulic fracture height growth through stress contrasts. In *Proceedings of SPE Hydraulic Fracturing Technology Conference, SPE 106030.*

Jeffrey, R. G. and Mills, K. W. (2000). Hydraulic fracturing applied to inducing longwall coal mine goaf falls. In *Proceedings of the 4th North American Rock Mechanics Symposium*, pages 423–430.

Joshaghani, M. S., Chang, J., Nakshatrala, K. B., and Knepley, M. G. (2019). Composable block solvers for the four-field double porosity/permeability model. *Journal of Computational Physics*, 386:428–466.

Kanin, E. A., Dontsov, E. V., Garagash, D. I., and Osiptsov, A. A. (2020a). A radial hydraulic fracture with pressure-dependent leak-off. *Journal of the Mechanics and Physics of Solids*, page 104062.

Kanin, E. A., Garagash, D. I., and Osiptsov, A. A. (2020b). The near-tip region of a hydraulic fracture with pressure-dependent leak-off and leak-in. *Journal of Fluid Mechanics*, 892:A31.

Khristianovic, S. A. and Zheltov, Y. P. (1955). Formation of vertical fractures by means of highly viscous fluids. In *Proceedings of the 4th World Petroleum Congress*, volume 2, pages 579 – 586.

Kovalyshen, Y. (2010). *Fluid-driven fracture in poroelastic medium*. PhD thesis, University of Minnesota.

Kresse, O., Weng, X., Gu, H., and Wu, R. (2013). Numerical modeling of hydraulic fracture interaction in complex naturally fractured formations. *Rock Mechanics and Rock Engineering*, 46:555–558.

Kumar, D. and Ghassemi, A. (2015). 3D simulation of multiple fracture propagation from horizontal wells. In *Proceedings of the 49th U.S. Rock Mechanics Symposium*. American Rock Mechanics Association.

Lecampion, B., Bunger, A., and Zhang, X. (2018). Numerical methods for hydraulic fracture propagation: A review of recent trends. *Journal of Natural Gas Science and Engineering*, 49:66–83.

Lenoach, B. (1995). The crack tip solution for hydraulic fracturing in a permeable solid. *Journal of the Mechanics and Physics of Solids*, 43:1025–1043.

Lewis, R. W. and Schrefler, B. A. (1998). *The finite element method in the static and dynamic deformation and consolidation of porous media*. John Wiley.

Linkov, A. M. and Markov, N. S. (2020). Improved pseudo three-dimensional model for hydraulic fractures under stress contrast. *International Journal of Rock Mechanics and Mining Sciences*, 130:104316.

Lord, D. L. (1994). Study of perforation friction pressure employing a large-scale fracturing flow simulator. In *Proceedings of SPE Annual Technical Conference and Exhibition*. Society of Petroleum Engineers.

Madyarova, M. V. (2003). *Fluid-driven penny-shaped fracture in elastic medium*. PhD thesis, University of Minnesota.

McClure, M., Kang, C., Hewson, C., and Medam, S. (2018). Resfrac technical writeup. *arXiv:1804.02092*.

McLennan, J. D. and Picardy, J. C. (1985). Pseudo-three-dimensional fracture growth modeling. In *Proceedings of the 26th US Symposium on Rock Mechanics*, pages 323–331. American Rock Mechanics Association.

Mikelić, A., Wheeler, M. F., and Wick, T. (2015). Phase-field modeling of a fluid-driven fracture in a poroelastic medium. *Computational Geosciences*, 19(6):1171–1195.

Montgomery, C. T. and Smith, M. B. (2010). Hydraulic fracturing: History of an enduring technology. *Journal of Petroleum Technology*, 62(12):26–40.

Moukhtari, F.-E. and Lecampion, B. (2018). A semi-infinite hydraulic fracture driven by a shear-thinning fluid. *Journal of Fluid Mechanics*, 838:573–605.

Nakshatrala, K. B., Joodat, S. H. S., and Ballarini, R. (2018). Modeling flow in porous media with double porosity/permeability: Mathematical model, properties, and analytical solutions. *Journal of Applied Mechanics*, 85(8).

Nolte, K. G. (1991). Fracturing-pressure analysis for nonideal behavior. *Journal of Petroleum Technology*, 43(02):210–218.

Nordgren, R. P. (1972). Propagation of a vertical hydraulic fracture. *SPE Journal*, 12(04):306–314.

Olson, J. E. (2008). Multi-fracture propagation modeling: Applications to hydraulic fracturing in shales and tight gas sands. In *Proceedings of the 42nd U.S. Rock Mechanics Symposium*. American Rock Mechanics Association.

Palmer, I. D. (1983). Three-dimensional hydraulic fracture propagation in the presence of stress variations. *SPE Journal*, 23:870–878.

Palmer, I. D. and Carroll, H. B. (1983). Numerical solution for height and elongated hydraulic fractures. In *Proceedings of SPE/DOE Low Permeability Gas Reservoirs Symposium*. Society of Petroleum Engineers.

Peirce, A. and Bunger, A. (2015). Interference fracturing: Nonuniform distributions of perforation clusters that promote simultaneous growth of multiple hydraulic fractures. *SPE Journal*, 20(02):384–395.

Peirce, A. and Detournay, E. (2008). An implicit level set method for modeling hydraulically driven fractures. *Computer Methods in Applied Mechanics and Engineering*, 197(33-40):2858–2885.

Perkins, T. K. and Kern, L. R. (1961). Widths of hydraulic fractures. *Journal of Petroleum Technology*, 13(09):937–949.

Protasov, I. and Donstov., E. (2017). A comparison of non-local elasticity models for a blade-like hydraulic fracture. In *Proceedings of the 51st U.S. Rock Mechanics/-Geomechanics Symposium*. American Rock Mechanics Association.

Protasov, I. I., Peirce, A. P., and Dontsov, E. V. (2018). Modeling constant height parallel hydraulic fractures with the elliptic displacement discontinuity method (EDDM). In *Proceedings of the 52nd US Rock Mechanics/Geomechanics Symposium*. American Rock Mechanics Association.

Rathgeber, F., Ham, D. A., Mitchell, L., Lange, M., Luporini, F., McRae, A. T. T., Bercea, G.-T., Markall, G. R., and Kelly, P. H. J. (2016). Firedrake: automating the finite element method by composing abstractions. *ACM Transactions on Mathematical Software (TOMS)*, 43(3):1–27.

Rezaei, A., Siddiqui, F., Bornia, G., and Soliman, M. (2019). Applications of the fast multipole fully coupled poroelastic displacement discontinuity method to hydraulic fracturing problems. *Journal of Computational Physics*, 399:108955.

Rice, J. R. (1968). Mathematical analysis in the mechanics of fracture. In Liebowitz, H., editor, *Fracture: An Advanced Treatise*, volume II, chapter 3, pages 191–311. Academic Press, New York, NY.

Romero, J., Mack, M. G., and Elbel, J. L. (1995). Theoretical model and numerical investigation of near-wellbore effects in hydraulic fracturing. In *Proceedings of SPE Annual Technical Conference and Exhibition*. Society of Petroleum Engineers.

S. H. Advaniand, T. S. L. and Lee, J. (1990). Three-dimensional modeling of hydraulic

fractures in layered media: Part I–finite element formulations. *J. Energy Resour. Technol.*, 112:1–9.

Salimzadeh, S. and Khalili, N. (2015). A three-phase XFEM model for hydraulic fracturing with cohesive crack propagation. *Computers and Geotechnics*, 69:82–92.

Sarvaramini, E. and Garagash, D. (2015). Breakdown of a pressurized fingerlike crack in a permeable solid. *Journal of Applied Mechanics*, 82:061006.

Savitski, A. A. and Detournay, E. (2002). Propagation of a penny-shaped fluid-driven fracture in an impermeable rock: Asymptotic solutions. *International Journal of Solids and Structures*, 39:6311–6337.

Settari, A. and Cleary, M. P. (1986). Development and testing of a pseudo-three-dimensional model of hydraulic fracture geometry. *SPE Production Engineering*, 1(06):449–466.

Settari, A. et al. (1985). A new general model of fluid loss in hydraulic fracturing. *Society of Petroleum Engineers Journal*, 25(04):491–501.

Sherman, C. S., Aarons, L. R., and Morris, J. P. (2015). Finite element modeling of curving hydraulic fractures and near-wellbore hydraulic fracture complexity. In *Proceedings of the 49th U.S. Rock Mechanics Symposium*. American Rock Mechanics Association.

Skopintsev, A. M., Dontsov, E. V., Kovtunenko, P. V., Baykin, A. N., and Golovin, S. V. (2020). The coupling of an enhanced pseudo-3D model for hydraulic fracturing with a proppant transport model. *arXiv preprint arXiv:2003.05676*.

Tada, H., Paris, P. C., Irwin, G. R., and Tada, H. (2000). *The stress analysis of cracks handbook*, volume 130. ASME press New York.

Vandamme, L. and Curran, J. H. (1989). A three-dimensional hydraulic fracturing simulator. *International Journal for Numerical Methods in Engineering*, 28(4):909–927.

Vandamme, L. M. and Roegiers, J.-C. (1990). Poroelasticity in hydraulic fracturing simulators. *Journal of Petroleum Technology*, 42:1199–1203.

Warpinski, N. R., Abou-Sayed, I. S., Moschovidis, Z., and Parker, C. (1993). Hydraulic fracture model comparison study: Complete results. Technical report, Sandia National Labs., Albuquerque, NM (United States).

Weng, X. (1992). Incorporation of 2D fluid flow into a pseudo-3D hydraulic fracturing simulator. *SPE Production Engineering*, 7(04):331–337.

Wu, K., Olson, J., Balhoff, M. T., and Yu, W. (2017). Numerical analysis for promoting uniform development of simultaneous multiple-fracture propagation in horizontal wells. *SPE Production & Operations*, 32(01):41–50.

Wu, K. and Olson, J. E. (2015). A simplified three-dimensional displacement discontinuity method for multiple fracture simulations. *International Journal of Fracture*, 193(2):191–204.

Wu, R., Kresse, O., Weng, X., Cohen, C.-E., and Gu, H. (2012). Modeling of interaction of hydraulic fractures in complex fracture networks. In *Proceedings of SPE Hydraulic Fracturing Technology Conference*. Society of Petroleum Engineers.

Yoshioka, K. and Bourdin, B. (2016). A variational hydraulic fracturing model coupled to a reservoir simulator. *International Journal of Rock Mechanics and Mining Sciences*, 88:137–150.

Zheng, Y., Burridge, R., and Burns, D. R. (2003). Reservoir simulation with the finite element method using biot poroelastic approach. Technical report, Massachusetts Institute of Technology. Earth Resources Laboratory.

Zia, H. and Lecampion, B. (2020). Pyfrac: A planar 3D hydraulic fracture simulator. *Computer Physics Communications*, 255:107368.

Appendices

A Stress field of point displacement discontinuity

The stress field $\boldsymbol{\sigma}^p$ induced by a point displacement discontinuity can be expressed through the following relations (Crouch and Starfield, 1983):

$$
\begin{aligned}
\sigma^p_{11} &= \frac{E'}{8\pi}[\phi_{3,33} + 2\phi_{1,13} + 2\nu\phi_{2,23} + (1-2\nu)\phi_{3,22} - \sum_{k=1}^{3} x_3\phi_{k,k11}],\\
\sigma^p_{22} &= \frac{E'}{8\pi}[\phi_{3,33} + 2\phi_{2,23} + 2\nu\phi_{1,13} + (1-2\nu)\phi_{3,11} - \sum_{k=1}^{3} x_3\phi_{k,k22}],\\
\sigma^p_{33} &= \frac{E'}{8\pi}[\phi_{3,33} - \sum_{k=1}^{3} x_3\phi_{k,k33}],\\
\sigma^p_{13} &= \frac{E'}{8\pi}[\phi_{1,33} + \nu\frac{\partial}{\partial x_2}(\phi_{1,2} - \phi_{2,1}) - \sum_{k=1}^{3} x_3\phi_{k,k13}],\\
\sigma^p_{23} &= \frac{E'}{8\pi}[\phi_{2,33} - \nu\frac{\partial}{\partial x_1}(\phi_{1,2} - \phi_{2,1}) - \sum_{k=1}^{3} x_3\phi_{k,k23}],\\
\sigma^p_{12} &= \frac{E'}{8\pi}[(1-\nu)\frac{\partial}{\partial x_3}(\phi_{1,2} + \phi_{2,1}) - (1-2\nu)\phi_{3,12} - \sum_{k=1}^{3} x_3\phi_{k,k12}],
\end{aligned}
\tag{A.1}
$$

where the local coordinate system is centered at the point displacement discontinuity, and $\boldsymbol{\sigma}^p$ is considered at x_1, x_2, x_3. The elastic potential ϕ_i corresponding to the point displacement discontinuity is defined in Eq. (2.3), and its derivatives are denoted by

$$
\phi_{i,j} = \frac{\partial\phi_i}{\partial x_j}, \quad \phi_{i,jp} = \frac{\partial^2\phi_i}{\partial x_j\partial x_p}, \quad \phi_{i,jpq} = \frac{\partial^3\phi_i}{\partial x_j\partial x_p\partial x_q}. \tag{A.2}
$$

B Approximation of stress tensor

The stress approximation reduces the computational complexity of the reduced-order models based on the EPKN and EP3D methods. The method is referred to as the elliptic displacement discontinuity method (EDDM) (Protasov et al., 2018). It assumes and involves the potential (4.8), the computation of which reduces to the following integral

$$\phi^* = \int_{-\Delta x_1/2}^{\Delta x_1/2} I(x_1, x_2, x_3, x_1', h)\ dx_1', \tag{B.1}$$

where

$$I(x_1, x_2, x_3, x_1', h) = \int_{-h/2}^{h/2} \frac{\sqrt{1 - 4{x_2'}^2/h^2}}{\sqrt{(x_1 - x_1')^2 + (x_2 - x_2')^2 + x_3^2}}\ dx_2'. \tag{B.2}$$

Substituting $\xi_i = 2x_i/h$, $\xi_i' = 2x_i'/h$, $\eta = \frac{4}{h^2}\left[(x_1 - x_1')^2 + x_3^2\right]$ into equation (B.2) yields

$$I(x_1, x_2, x_3, x_1', h) = \hat{I}(\eta, \xi_2) = \int_{-1}^{1} \frac{\sqrt{1 - \xi_2'^2}}{\sqrt{\eta + (\xi_2 - \xi_2')^2}}\ d\xi_2'. \tag{B.3}$$

The EP3D model's boundary conditions for stress are formulated at $x_2 = 0$, which corresponds to $\xi_2 = 0$. In this case, the integral (B.3) can be calculated analytically, which results in

$$\hat{I}(\eta, 0) = 2\sqrt{1+\eta}\left[\mathrm{K}\left(\frac{1}{1+\eta}\right) - \mathrm{E}\left(\frac{1}{1+\eta}\right)\right], \quad \eta \neq 0, \tag{B.4}$$

where

$$\mathrm{K}(m) = \int_0^{\pi/2} (1 - m\sin^2\theta)^{-1/2}\ d\theta, \tag{B.5}$$

is the complete elliptic integrals of the first kind, and

$$\mathrm{E}(m) = \int_0^{\pi/2} (1 - m \sin^2 \theta)^{1/2} \, d\theta. \tag{B.6}$$

is the complete elliptic integral of the second kind.

The elasticity relations (A.1) require computation of derivatives of the integral (B.1) that transfer to the integral (B.3). The first derivative of (B.3) with respect to ξ_2 is zero at $\xi_2 = 0$. The expression for the second derivative is

$$\frac{\partial}{\partial \xi_2^2} \left[\hat{I}(\eta, \xi_2) \right] \Big|_{\xi_2 = 0} = \frac{2}{\sqrt{1+\eta}} \left[\mathrm{E}\left(\frac{1}{1+\eta} \right) - \mathrm{K}\left(\frac{1}{1+\eta} \right) \right], \quad \eta \neq 0. \tag{B.7}$$

Other derivatives with respect to ξ_1 and ξ_3 are calculated by differentiating Equation (B.4) with respect to $\eta(\xi_1, \xi_2)$. As a result, the computational complexity of the integral (B.1) corresponds to one-dimension.

For a single fracture element, the numerical integration of the expression (B.1) requires evaluation of the integrand at several point along x_1. The number of these points affect the accuracy of the numerical integration. The largest numerical error occurs in the computation of the self-effect, i.e., the stress field that the element induces on itself, which may require additional evaluation points. However, for self-effect $x_3 = 0$ and $\phi^*_{,33}$ can be computed purely analytically, resulting in

$$\phi^*_{,33} = \frac{4}{h} \left[G\left(\frac{2(x_1 + \frac{\Delta x_1}{2})}{h} \right) - G\left(\frac{2(x_1 - \frac{\Delta x_1}{2})}{h} \right) \right], \tag{B.8}$$

where, G is given by

$$G(s) = \frac{\sqrt{1+s^2}}{s}\mathrm{E}\left(\frac{1}{1+s^2}\right). \tag{B.9}$$

The plane strain limit of pressure can be obtained by taking the plane strain limit of equation (B.8) and using equations (A.1). For the approximate displacement discontinuity (4.6) the plane strain limit of pressure is

$$p_{\mathrm{ps}} = \frac{E' D_3^h}{2h} + \frac{E' D_3^{h_{\Delta\sigma}}}{2h_{\Delta\sigma}}. \tag{B.10}$$

On the other hand, the plane strain solution for pressure that corresponds to the fracture opening (4.3) yields (Adachi et al., 2007)

$$p = \sqrt{\frac{2}{\pi h}} K_I + \Delta\sigma \left[1 - \frac{2}{\pi}\arcsin\left(\frac{H}{h}\right)\right]. \tag{B.11}$$

These two equations in conjunction with (4.3) and (4.5) can be used to find $h_{\Delta\sigma}$, D_3^h, and $D_3^{h_{\Delta\sigma}}$ in the approximate relation (4.6). In addition, the approximation is required to maintain the cross-sectional area of the fracture opening. Since the first term in (4.3) represents an ellipse, the approximation does not change its shape and

$$D_3^h = \frac{4K_I}{E'}\sqrt{\frac{h}{2\pi}}. \tag{B.12}$$

The cross-sectional area of the approximate relation (4.6) must be equal to the area of the fracture opening (4.3), which can be found from (4.5). The area of the second

term in (4.3) must be equal to the area of the second ellipse, i.e., in (4.6)

$$\frac{\Delta\sigma H}{E'}\sqrt{h^2 - H^2} = \frac{\pi}{4} D_3^{h_{\Delta\sigma}} h_{\Delta\sigma}. \tag{B.13}$$

This relation can be combined with (4.3) and (4.5) to yield

$$h_{\Delta\sigma} = \left(\frac{2H\sqrt{h^2 - H^2}}{\pi - 2\arcsin\left(H/h\right)} \right)^{1/2} \tag{B.14}$$

and

$$D_3^{h_{\Delta\sigma}} = \left(\Delta\sigma \left[1 - \frac{2}{\pi} \arcsin\left(\frac{H}{h}\right) \right] \right) \frac{2h_{\Delta\sigma}}{E'}. \tag{B.15}$$

C Multi-scale near-tip asymptotics

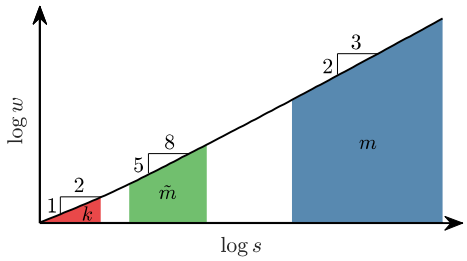

Figure 37: Asymptotic solution for the fracture opening w in the near-tip region of a hydraulic fracture plotted on a logarithmic scale. Red, green, and blue colors represent the regions corresponding to toughness (k), leak-off ($\tilde{m}$), and viscous (m) limiting solutions, respectively, see Eq. (C.1).

Analysis of a semi-infinite fluid-driven crack under plane strain conditions (model for the near tip region) (Garagash et al., 2011; Detournay, 2016) shows that there are three limiting regimes of propagation related to domination of either fracture toughness (k regime), fluid leak-off ($\tilde{m}$ regime), or fluid viscosity (m regime). The corresponding crack-opening displacements in the near-front region are given by (Rice, 1968; Lenoach, 1995; Desroches et al., 1994),

$$w_k = \frac{K'}{E'} s^{1/2}, \quad w_{\tilde{m}} = \beta_{\tilde{m}} \left(\frac{4\mu'^2 V C'^2}{E'^2} \right)^{1/8} s^{5/8}, \quad w_m = \beta_m \left(\frac{\mu' V}{E'} \right)^{1/3} s^{2/3}, \qquad \text{(C.1)}$$

where V is the propagation velocity of the fracture front, K', E', μ', C' are the scaled toughness, modulus, viscosity, and leak-off (see (2.2)), while $\beta_{\tilde{m}} = 4/(15^{1/4}(\sqrt{2}-1)^{1/4})$ and $\beta_m = 2^{1/3}3^{5/6}$ are numeric constants.

As demonstrated in (Garagash et al., 2011), transitions between the regimes occur

on the following length scales,

$$l_{mk} = \left(\frac{K'^3}{E'^2 V \mu'}\right)^2, \quad l_{m\tilde{m}} = \frac{K'^8}{E'^6 C'^2 V \mu'^2}, \quad l_{\tilde{m}k} = \frac{C'^6 E'^2}{V^5 \mu'^2}, \tag{C.2}$$

where l_{mk} corresponds to the transition from k regime to m regime, $l_{\tilde{m}k}$ – from k regime to $\tilde{m}$ regime, and $l_{m\tilde{m}}$ – from $\tilde{m}$ to m. The closest to the front is the k regime, which can transition to either $\tilde{m}$ and then to m regime, or directly to m, depending on the parameters.

The general solution for a semi-infinite hydraulic fracture that incorporates all the aforementioned limiting regimes was computed numerically in (Garagash et al., 2011). Figure 37 schematically shows the solution as well as outlines validity regions for the toughness, leak-off, and viscosity limiting solutions in red, green, and blue, respectively. For the purpose of the development of the numerical algorithm, as considered in this study, it is beneficial to utilize the fast approximate closed-form relation constructed in (Dontsov and Peirce, 2015c), which has been shown to be accurate up to 0.14% for the whole parametric space. In this paper, the latter solution, denoted by $w_a(s)$, is used as a propagation condition for the fracture opening, namely

$$w(s) \approx w_a(s), \quad s = o(L), \tag{C.3}$$

where L is the characteristic fracture size and s is the distance to the fracture front. Note that (C.3) captures the behavior outlined in (4.15) in the limit of $s \to 0$. But it has an extended validity zone, that is determined purely by the fracture size, by

capturing the effects of fluid viscosity and leak-off. The exact form of the approximate solution (C.3) can be found in (Dontsov and Peirce, 2015c), where it is expressed as

$$\frac{s^2 V \mu'}{E' w_a^3} = g_\delta\Big(\frac{K' s^{1/2}}{E' w_a}, \frac{2 s^{1/2} C'}{w_a V^{1/2}}\Big), \tag{C.4}$$

where g_δ is an analytic function. One the properties of the solution $w_a(s)$ is that

$$w_a(s) \propto s^\delta, \tag{C.5}$$

where

$$\delta = \frac{1}{2}\left[1 + \Delta\Big(\frac{K' s^{1/2}}{E' w_a}, \frac{2 s^{1/2} C'}{w_a V^{1/2}}\Big)\right], \tag{C.6}$$

where Δ is an analytic function. Both functions g_δ and Δ are given in (Dontsov and Peirce, 2015c).

D Fixed mesh approach

D.1 Motivation

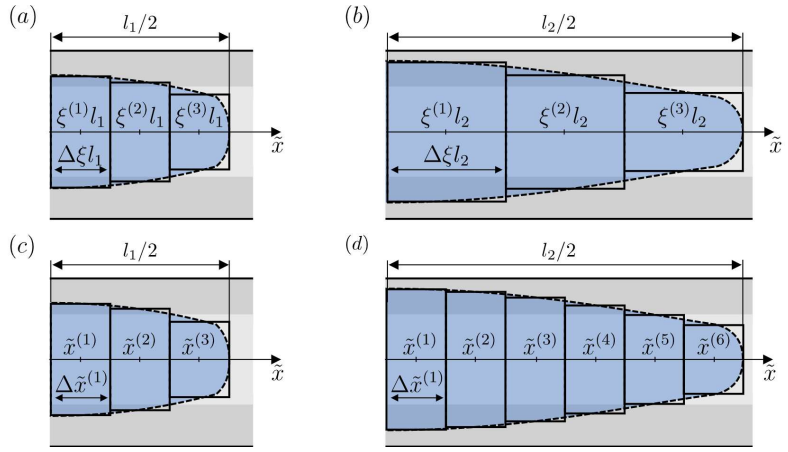

Figure 38: Illustration of the moving mesh approach for fracture lengths $l = l_1$ (a) and $l = l_2$ (b). Schematics of the fixed mesh approach for fracture lengths $l = l_1$ (c) and $l = l_2$ (d).

The original EPKN and EP3D models (Dontsov and Peirce, 2015a, 2016a) deal with a moving boundary by introducing a scaled coordinate in the $\tilde{x}$ direction, $\xi = 2\tilde{x}/l(t)$ $(0 \leq \xi \leq 1)$, where $l(t)$ is the length of the fracture. The moving mesh approach offers an efficient way to compute the fracture propagation and automatically scales the mesh relative to the fracture length. It works well for a single fracture that is planar and symmetric with respect to $\tilde{x}$. However, in the case of multiple fractures, it is more convenient to have a spatially fixed mesh in the physical coordinate $\tilde{x}$. While it is possible to use separate dimensionless coordinates for each wing of each fracture, this would introduce additional challenges, such as the coordinate transformation and re-computation of the stress tensor. Most importantly, the fixed mesh approach allows for easier representation of the curved non-planar

fractures.

Numerical discretizations for the moving mesh and the fixed mesh approaches are illustrated in Fig. 38. Figure 38a shows the moving mesh for fracture length $l = l_1$, where ξ_1, ξ_2, ξ_3 are the dimensionless coordinates that correspond to the x coordinate through $x = \xi l$, and $\Delta\xi$ is the dimensionless length of the mesh element. Figure 38b shows the moving mesh for a larger fracture length $l = l_2$. The positions of the fracture elements in dimensionless space ξ do not change, and the fracture propagation is reflected in the change of l from l_1 to l_2. The velocity of the fracture propagation $V = \frac{\mathrm{d}l}{\mathrm{d}t}$ is an unknown that is determined by the boundary conditions. In this approach, the position and the physical length of the mesh elements constantly change, resulting in mesh stretching. At the same time, the moving mesh approach keeps the number of mesh elements constant throughout the simulation. Figure 38c shows the fixed mesh methodology for fracture length $l = l_1$, while Fig. 38d shows the fracture with length $l = l_2$. The positions and lengths of all the mesh elements, but the tip, are fixed in the physical coordinate $\tilde{x}$. Therefore, the number of mesh elements increases in time. The tip element length is unknown and is determined by the propagation condition. Once the length of the tip element reaches a critical value, it is divided into two smaller elements.

Each element is referred to through the index $i = 1, \ldots, N$. The element's position in space is represented by the coordinate of its midpoint $\tilde{x}^{(i)}$, its length $\Delta\tilde{x}^{(i)}$, its height $h^{(i)}$, and its angle with the global x axis $\theta^{(i)}$. These are combined into the vectors $\tilde{\boldsymbol{x}} = (\tilde{x}^{(1)}, \ldots, \tilde{x}^{(N)})^T$, $\Delta\tilde{\boldsymbol{x}} = (\Delta\tilde{x}^{(1)}, \ldots, \Delta\tilde{x}^{(N)})^T$, $\boldsymbol{h} = (h^{(1)}, \ldots, h^{(N)})^T$, and $\boldsymbol{\theta} = (\theta^{(1)}, \ldots, \theta^{(N)})^T$.

The effective fracture opening is considered constant within each element and denoted by $\bar{w}^{(i)}$. These piece-wise constant values are combined into the vector $\bar{\boldsymbol{w}} = (\bar{w}^{(1)}, \ldots, \bar{w}^{(N)})^T$. The fluid pressure is considered at midpoint of each element is denoted by $p^{(i)}$ and combined into the vector $\bar{\boldsymbol{p}} = (\bar{p}^1, \ldots, \bar{p}^{(N)})^T$. The injection rate values Q_k are combined into $\boldsymbol{Q} = (Q_1, \ldots, Q_{N_f})$.

D.2 Tip element implementation

In this section, we describe the tip element implementation in the mEPKN and mEP3D model. The fracture tip element needs special consideration because it affects the following parts of the algorithm:

(1) the fracture extension which is computed by applying the boundary condition on the tip element;

(2) the numerical calculation of tractions which relies on the near-tip behavior;

(3) the split of the tip element when its length becomes large enough as the fracture propagates.

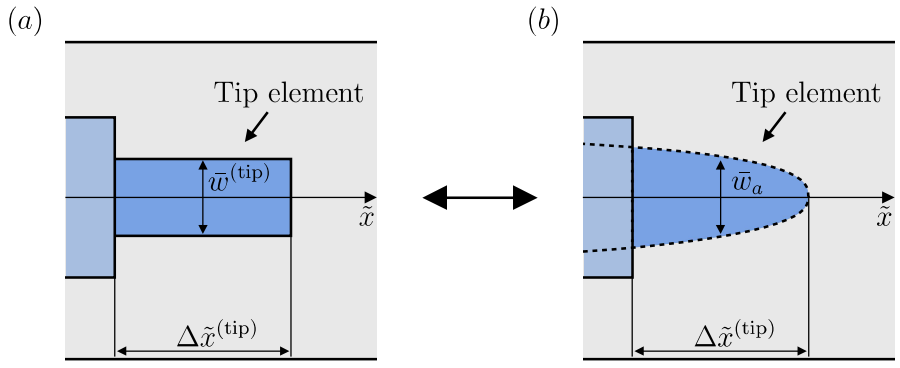

Figure 39: Fracture near-tip region represented by (a) the tip element of the numerical mesh, and (b) the asymptotic solution.

As other fracture elements, the tip element is characterized by a single value of

$\bar{w}^{(\text{tip})}$ since the fracture opening is a piece-wise constant function in the numerical algorithm, illustrated in Fig. 39a. Alternatively, the tip element is represented by the near-tip asymptotic solution, illustrated in Fig. 39b. These two representations are connected by the same volume of the tip element. In particular, the volume of the tip element of length Δs, denoted by $\mathcal{V}(\Delta s)$, is calculated according to the near-tip asymptotic solution. The exact expression for $\mathcal{V}(s)$ is given in Appendix E for the mEPKN model, and in Appendix G for the mEP3D model.

First, we discuss the tip extension driven by fluid flux, which changes the volume of the element. The length and the volume of the tip element must be in agreement with the asymptotic relation (E.3). The condition is schematically shown in Fig. 39. Therefore, the tip element's length is computed by solving (E.3) using the the volume of the tip element,

$$\mathcal{V}(\Delta\tilde{x}^{(\text{tip})}) = \bar{w}^{(\text{tip})} H \Delta\tilde{x}^{(\text{tip})}. \tag{D.1}$$

This expression directly relates $\Delta\tilde{x}^{(\text{tip})}$ and $\bar{w}^{(\text{tip})}$. After solving the lubrication equation, the fracture is extended by updating the tip elements' lengths based on the effective fracture opening.

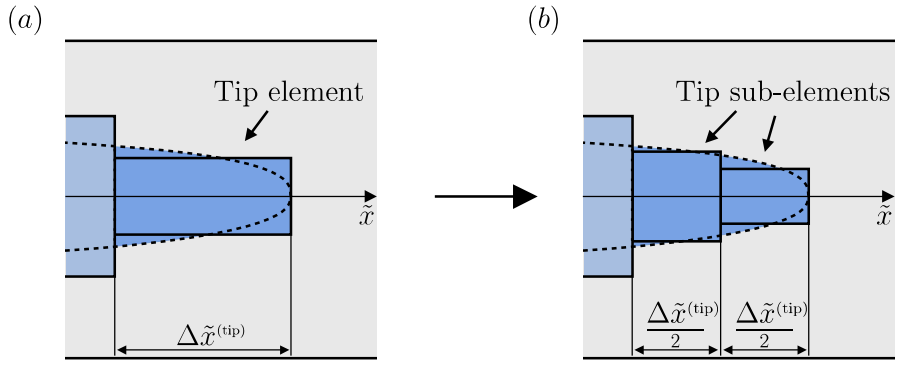

Figure 40: Tip element refinement for elasticity computation. (a) Tip element. (b) Tip is represented by two sub-elements.

Next, the near-tip asymptotic solution is used in the tractions calculation. The approximate elastic potential (B.1) is computed for the piece-wise constant displacement discontinuities along the fracture length. The accurate calculation of tractions requires a fine discretization of the mesh near the fracture, since the pressure is singular at the tip. Alternatively, the accurate results can be obtained on a coarse mesh by using the asymptotic near-tip solution for the fracture opening. This method, illustrated in Fig. 40, is based on the tip element splitting according to the near-tip asymptotic solution, which results in the expanded, but still coarse, mesh. The tip element of length $\Delta\tilde{x}^{(\mathrm{tip})}$ is split into two elements, denoted by 1 and 2 from the fracture front, with equal lengths

$$\Delta\tilde{x}_1^{(\mathrm{tip})} = \Delta\tilde{x}_2^{(\mathrm{tip})} = \frac{\Delta\tilde{x}^{(\mathrm{tip})}}{2}. \tag{D.2}$$

Their volumes, $\mathcal{V}_1$ and $\mathcal{V}_2$, are computed as

$$\mathcal{V}_1 = \mathcal{V}\left(\Delta\tilde{x}^{(\mathrm{tip})}/2\right), \quad \mathcal{V}_2 = \bar{w}^{(\mathrm{tip})} H \Delta\tilde{x}^{(\mathrm{tip})} - \mathcal{V}\left(\Delta\tilde{x}^{(\mathrm{tip})}/2\right). \tag{D.3}$$

The effective width of the new elements, given by

$$\bar{w}_1^{(\mathrm{tip})} = \frac{\mathcal{V}_1}{H\Delta\tilde{x}_1^{(\mathrm{tip})}}, \quad \bar{w}_2^{(\mathrm{tip})} = \frac{\mathcal{V}_2}{H\Delta\tilde{x}_2^{(\mathrm{tip})}}, \tag{D.4}$$

is used to compute the height of the corresponding elements. The obtained two new sub-elements replace the tip element in the elasticity computations, and the tractions are then computed on the expanded mesh.

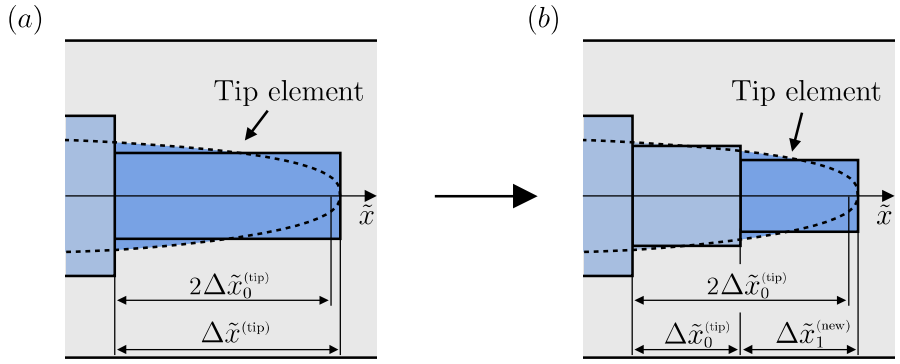

Figure 41: Creation of a new tip element. (a) Original tip element. (b) New split tip element.

Finally, we describe remeshing of the tip elements. Since the length of a tip element increases in time when the fracture propagates, the tip element may become too large compared to its original size, which leads to discretization error. The remeshing procedure is only applied to the tip element keeping other mesh elements intact. The scheme of the method is shown in Fig. 41. The length of the tip element of the original mesh at the initial moment of time is denoted by $\Delta\tilde{x}_0^{(\mathrm{tip})}$. The remeshing of the tip element applies to the evolved mesh when $\Delta\tilde{x}^{(\mathrm{tip})} > 2\Delta\tilde{x}_0^{(\mathrm{tip})}$. Once this happens, the tip element is split into two new elements, denoted by 1 and 2 from the fracture front, along its length. Element 1 becomes the new tip element and element 2 becomes a regular channel element. Note that this splitting is different from the one used in the elasticity calculation. The split is done so that the length of the second element is

$$\Delta\tilde{x}_2^{(\mathrm{new})} = \Delta\tilde{x}_0^{(\mathrm{tip})}, \tag{D.5}$$

and, consequently, the length of the new tip element is

$$\Delta\tilde{x}_1^{(\text{new})} = \Delta\tilde{x}^{(\text{tip})} - \Delta\tilde{x}_0^{(\text{tip})}. \tag{D.6}$$

The volumes of the new elements are computed as

$$\mathcal{V}_1 = \mathcal{V}\left(\Delta\tilde{x}_1^{(\text{new})}\right), \quad \mathcal{V}_2 = \bar{w}^{(\text{tip})} H \Delta\tilde{x}^{(\text{tip})} - \mathcal{V}\left(\Delta\tilde{x}_1^{(\text{new})}\right). \tag{D.7}$$

The effective width can be computed using relation (D.4).

E Numerical algorithm of mEPKN model

In this appendix, we describe the numerical algorithm for the mEPKN model. The model utilizes the fixed mesh approach detailed in Appendix D. The tip element volume calculation via the asymptotic near-tip solution is given in Section G.1. The discretized governing equations are presented in Section G.2.

E.1 Tip element volume

In this section, the tip element volume for the mEPKN model is presented. Denoting the horizontal distance from the tip by s, the fracture opening can be written as

$$w_a(x, y) = \alpha s^{\delta}, \tag{E.1}$$

where δ is defined in (C.6), and α is a constant, the exact value of which is not necessary for this derivation. The height of the fracture is constant and equal to H. We assume that the asymptotic solution (E.1) represents the fracture opening at $\tilde{y} = 0$.

Following the fracture opening approximation (3.3), the effective width is written as

$$\bar{w}_a(\tilde{x}) = \frac{\pi}{4}\alpha s^{\delta}. \tag{E.2}$$

The asymptotic volume of the tip element of length Δs can be obtained by integrating

the effective fracture opening (E.2)

$$\mathcal{V}(\Delta s) = H \int_0^{\Delta s} \bar{w}_a ds = \frac{\pi H}{4(\delta+1)} w_a(\Delta s)\Delta s \tag{E.3}$$

where, additionally, α has been substituted from equation (E.1) and the function $w_a(\Delta s)$ can be obtained from (C.4).

The volume of the tip element given by Eq. E.3 is used in the numerical algorithm to compute the fracture extension, the tractions, and to update the mesh with new elements, as described in Appendix D.

E.2 Discretized governing equations

We start by introducing the discretized elasticity relation arising in the mEPKN model. The numerically computed pressure in the tip element has the largest error among other crack segments due to the singular nature of the stress field at the fracture tip and the zero fluid lag assumption. This error leads to the wrong calculation of fluid flux into the tip element. One way to overcome this limitation is by splitting the tip element into two sub-elements. In this case, one can be treated as the tip element, and the other one is effectively the inner element. Since the primary source of error is related to the tip, the inner sub-element's stress field is accurate and can be used for calculation of fluid flux into the whole tip element, including both sub-elements. The correct splitting of the tip element is ensured by utilizing the asymptotic near-tip solution, which also governs the flux between the two sub-elements. The tip sub-elements are expressed in terms of the tip element volume

and length. The length of the sub-elements is one half of the tip element, and their volumes are given by equation (D.4). The original mesh of size N is replaced by the expanded mesh, which contains tip sub-elements replacing the original tip elements. Since each tip element yields two sub-elements, the number of elements of the expanded mesh is larger than N and is denoted by N_e. At the center of each element of this mesh, the piece-wise constant normal and shear displacement discontinuities are combined into $\boldsymbol{D}_n = (D_n^{(1)}, \ldots, D_n^{(N_e)})^T$ and $\boldsymbol{D}_s = (D_s^{(1)}, \ldots, D_s^{(N_e)})^T$, and the stress tensor components into $\boldsymbol{\sigma}_n = (\sigma_n^{(1)}, \ldots, \sigma_n^{(N_e)})^T$ and $\boldsymbol{\sigma}_s = (\sigma_n^{(1)}, \ldots, \sigma_s^{(N_e)})^T$. Note that the vector of normal displacement discontinuity $\boldsymbol{D}_n$ has the size N_e and corresponds to the expanded mesh, while the fracture opening vector $\bar{\boldsymbol{w}}$ has the size N and corresponds to the original mesh.

The elasticity relation, computed using the stress integral (2.6) and the approximation for the elastic potential (4.8), reduces to

$$\begin{aligned} \boldsymbol{\sigma}_n &= \boldsymbol{C}_{nn}\boldsymbol{D}_n + \boldsymbol{C}_{ns}\boldsymbol{D}_s, \\ \boldsymbol{\sigma}_s &= \boldsymbol{C}_{sn}\boldsymbol{D}_n + \boldsymbol{C}_{ss}\boldsymbol{D}_s, \end{aligned} \tag{E.4}$$

where $\boldsymbol{C}_{nn}$, $\boldsymbol{C}_{ns}$, $\boldsymbol{C}_{sn}$, and $\boldsymbol{C}_{ss}$ are the elasticity matrices. Each term on the right-hand side of (E.4) represents matrix-vector multiplication.

After applying stress boundary conditions (4.9) to the elasticity relation (E.4), the shear displacement discontinuity is expressed as

$$\boldsymbol{D}_s = -\boldsymbol{C}_{ss}^{-1}\boldsymbol{C}_{sn}\boldsymbol{D}_n, \tag{E.5}$$

and the pressure values vector of the expanded mesh can be written as

$$\hat{\boldsymbol{p}} = -\left(\boldsymbol{C}_{nn} - \boldsymbol{C}_{ns}\boldsymbol{C}_{ss}^{-1}\boldsymbol{C}_{sn}\right)\boldsymbol{D}_n. \tag{E.6}$$

The latter expression relates the pressure and the normal displacements at the elements of the expanded mesh of size N_e, including all sub-elements of the tip elements.

Next, the elasticity relation (E.6) is reduced to the original mesh, so that the fluid flux into the tip element is calculated based on the pressure at its inner sub-element. The pressure values at other sub-elements are not used in further computations. Because the vector $\boldsymbol{D}_n$ is larger than $\bar{\boldsymbol{w}}$, are extra components are written in terms of fracture opening according to the near-tip asymptotic solution, as detailed in Appendix D. Overall, the vector of pressure over the regular mesh is

$$\bar{\boldsymbol{p}} = -\boldsymbol{C}\bar{\boldsymbol{w}}. \tag{E.7}$$

Note that in the vector of numerical values $\bar{\boldsymbol{p}}$, each component corresponds to pressure at the center of fracture element, with the exception of the tip elements, for which the pressure corresponds to the center of its inner sub-element.

The subset of $\bar{\boldsymbol{p}}$ corresponding to the injection points of each fracture is denoted by $\boldsymbol{p}_w$. The flux balance, consisting from equations (2.9) and (2.10), takes the following form

$$\begin{cases} \boldsymbol{I}_v^T\boldsymbol{Q} = Q_0, \\ \\ \boldsymbol{p}_w + \Delta\boldsymbol{p}_{\text{perf}} = p_0\boldsymbol{I}_v, \end{cases} \qquad \text{with } \Delta\boldsymbol{p}_{\text{perf}} = \left(\Delta p_{\text{perf}}^{(1)}, \ldots, \Delta p_{\text{perf}}^{(N_f)}\right)^T, \tag{E.8}$$

where $\boldsymbol{I}_v$ is the vector of ones of size N_f, and $\Delta p^{(k)}_{\text{perf}} = \frac{8\rho Q_k^2}{\pi^2 C_{d,k}^2 d_k^4}$.

To obtain the discretized lubrication equation (4.13), the time derivative is discretized by the backward finite difference,

$$\frac{\partial \bar{w}^{(i)}}{\partial t} \approx \frac{\bar{w}^{(i)} - \bar{w}_0^{(i)}}{\Delta t}, \tag{E.9}$$

which can be summarized for all elements in a vector form as

$$\frac{1}{\Delta t}\left[\bar{\boldsymbol{w}} - \bar{\boldsymbol{w}}^0\right]. \tag{E.10}$$

The derivative of flux is discretized by the central difference scheme as

$$\frac{\partial \bar{q}_{\tilde{x}}^{(i)}}{\partial \tilde{x}} \approx \frac{\bar{q}_{\tilde{x}}^{(i+)} - \bar{q}_{\tilde{x}}^{(i-)}}{\Delta \tilde{x}^{(i)}}, \tag{E.11}$$

where $\bar{q}_{\tilde{x}}^{(i+)}$ and $\bar{q}_{\tilde{x}}^{(i-)}$ denote the flux through the two lateral edges located at $\tilde{x} = \tilde{x}^{(i)} + \frac{\Delta \tilde{x}^{(i)}}{2}$ and $\tilde{x} = \tilde{x}^{(i)} - \frac{\Delta \tilde{x}^{(i)}}{2}$ respectively. At the tip element, $\bar{q}_{\tilde{x}}^{(i\pm)}$ is zero at the edge corresponding to the crack front to satisfy the zero flux boundary condition. The flux at the edge between adjacent elements i and j can be written by discretizing equation (4.12) as

$$\bar{q}_{\tilde{x}}^{(i+)} \approx -\frac{1}{\pi^2 \mu'} \frac{\bar{p}^{(j)} - \bar{p}^{(i)}}{\tilde{x}^{(j)} - \tilde{x}^{(i)}} \left(\frac{w^{(j)} + w^{(i)}}{2}\right)^3. \tag{E.12}$$

The source term is rewritten in the discretized form as

$$\frac{Q_k}{H}\delta(\tilde{x}) \approx \frac{Q_k}{H}\frac{\delta_{ii^k}}{\Delta\tilde{x}^{(i^k)}}, \tag{E.13}$$

where δ_{ii^k} is the Kronecker delta function that enables to prescribe the source term at the injection element denoted by (i^k). The source term (E.13) is represented by the vector $\boldsymbol{q}_s$.

Given all of the above, the lubrication equation can be written as

$$\left[\frac{1}{\Delta t}\boldsymbol{I} - \boldsymbol{AC}\right]\bar{\boldsymbol{w}} = \boldsymbol{q}_s + \frac{1}{\Delta t}\bar{\boldsymbol{w}}^0, \tag{E.14}$$

where $\boldsymbol{I}$ is identity matrix and $\bar{\boldsymbol{w}}^0$ is the solultion from the previous time step. Denoting

$$\boldsymbol{L} = \frac{1}{\Delta t}\boldsymbol{I} - \boldsymbol{AC}, \qquad \boldsymbol{b} = \boldsymbol{q}_s + \frac{1}{\Delta t}\bar{\boldsymbol{w}}^0. \tag{E.15}$$

Eq. (E.14) can be written as

$$\boldsymbol{L}\bar{\boldsymbol{w}} = \boldsymbol{b}. \tag{E.16}$$

The initial guess for $\bar{\boldsymbol{w}}$ is taken from the solution for the previous time step $\bar{\boldsymbol{w}}^0$. The operator $\boldsymbol{L}$ and the right-hand side vector $\boldsymbol{b}$ depend on $\bar{\boldsymbol{w}}$, either directly or through the position the lateral fracture tip. Assuming that this dependence is small relative to the elastic effects, the system (E.16) is solved for $\bar{\boldsymbol{w}}$ as a linear system. Then, $\boldsymbol{L}$, $\boldsymbol{b}$, $\boldsymbol{Q}$, and the position and direction of the lateral fracture fronts are updated for the new $\bar{\boldsymbol{w}}$. The process repeats until convergence. The initial condition for $\bar{\boldsymbol{w}}^0$

is constructed from the volume of the radial fracture solution (Dontsov, 2016) with diameter equal to H.

The lateral extension of the fracture is guided by the growth of the tip elements, the lengths of which are computed from the effective fracture opening using equations (E.3) and (D.1).

F Correction for viscous and leak-off dominated height growth

As was mentioned in section 4, the concept of apparent fracture toughness allows accounting for viscous dissipation in fracture height growth (Dontsov and Peirce, 2015a). The classic P3D model employs a constant pressure plane strain solution and becomes inaccurate in the presence of viscous fluid since the latter may cause a pressure gradient. To address this problem, the EP3D model (Dontsov and Peirce, 2015a) introduced the apparent toughness

$$K^{\text{apparent}} = K_{Ic} + \Delta K_{Ic}, \tag{F.1}$$

that replaces fracture toughness in the equations and captures the effect of viscous resistance on fracture height's growth via ΔK_{Ic}. First, the correction is estimated for the case of a plane strain fracture by equating the near-tip asymptotics for toughness and viscous regimes of propagation at characteristic distance d, which results in

$$\Delta K_{Ic} = \mu'^{1/3} E'^{2/3} V^{1/3} d^{1/6}, \quad h > H. \tag{F.2}$$

The expression for characteristic length is found from dimensional analysis of the plane strain problem with symmetric stress barriers

$$d = \frac{C_1 h}{1 + C_2 \dfrac{H\Delta\sigma}{h^{1/2}\Delta K_{Ic}}}, \quad h > H. \tag{F.3}$$

Here, the constants $C_1 = 0.175$ and $C_2 = 0.5$ are fitted to minimize the error of the approximate solution obtained with the derived toughness correction relative to the numerically computed result.

The case of a radial fracture is considered separately. The toughness correction has a similar expression

$$\Delta K_{Ic} = C_3 \mu'^{1/3} E'^{2/3} V^{1/3} d^{1/6}, \quad h \leq H \tag{F.4}$$

but with a different constant $C_3 = 1.2$. Before the radial fracture reaches stress barriers, i.e., $\max(h) < H$, $r = h/2$ is the radius of the fracture, and characteristic length $d = r$. After the fracture propagates through the barriers, the radial solution is still used to model the vertical cross-section near the tip region, where the height is less than H. For these cross-sections, $d = b\frac{H}{2}$, where $b = 1.5$.

The approach is extended to include leak-off in the toughness correction. The correction for the plane strain fracture is obtained by equating the near-tip asymptotics of the toughness and leak-off regimes of propagation, yielding

$$\Delta K_{Ic} = \mu'^{1/4} E'^{3/4} C'^{1/4} V^{1/8} d^{1/8}, \quad h > H. \tag{F.5}$$

The characteristic length can be found from (F.3), while $C_1 = 0.15$ and $C_2 = 1.2$ are again selected to have the best match to the reference solutions.The correction for

the radial fracture case is

$$\Delta K_{Ic} = C_3 \mu'^{1/4} E'^{3/4} C'^{1/4} V^{1/9} d^{1/8}, \quad h \leq H, \tag{F.6}$$

where $C_3 = 0.6$ is obtained by matching the solution to that for the radial fracture propagating in the leak-off regime (Dontsov, 2016).

G Numerical algorithm of mEP3D model

This appendix describes the numerical algorithm for the mEP3D model. The algorithm is based on the fixed mesh approach discussed in Appendix D. We introduce the tip element volume calculation according to the asymptotic near-tip solution in Section G.1. The discretized governing equations are given in Section G.2.

G.1 Tip element volume

The effective fracture opening of the tip element is approximated by the radial fracture solution, according to relation (4.5). Therefore, it is necessary to consider the asymptotic near-tip solution in radial geometry. By applying the radial fracture symmetry to the near-tip asymptotic solution (C.5), the fracture opening can be written as

$$w_a(x,y) = \alpha \left(\sqrt{r^2 - \tilde{x}^2 - \tilde{y}^2} \right)^{2\delta}, \tag{G.1}$$

where r is the radius, and δ is defined in (C.6). Note that α is a constant, the exact value of which is not necessary for this derivation. The height of the fracture is $h = 2\sqrt{r^2 - \tilde{x}^2}$. The distance from the tip at $\tilde{y} = 0$ is denoted by $s = r - \tilde{x}$. Near the tip, assuming $s \ll r$, the solution takes the following form

$$w_a(s) = \alpha \left(2rs\right)^{\delta}. \tag{G.2}$$

Based on this expression, we compute the effective width as

$$\bar{w}_a(\tilde{x}) = \frac{1}{H}\int_{-h/2}^{h/2} \alpha \left(\sqrt{r^2 - \tilde{x}^2 - \tilde{y}^2}\right)^{2\delta} d\tilde{y} = \frac{\alpha}{H}\left(r^2 - \tilde{x}^2\right)\frac{\sqrt{\pi}\Gamma\left(\delta+1\right)}{\Gamma\left(\delta+\frac{3}{2}\right)}, \tag{G.3}$$

where Γ denotes Gamma function. Note that this effective fracture opening has been derived from the analytical asymptotics and depends on $\tilde{x}$, in contrast to $\bar{w}^{(\text{tip})}$, which is used in the numerical algorithm and does not depend on $\tilde{x}$ in the tip element. The asymptotic volume of the fracture fragment with bounds at $\tilde{x} = r - \Delta s$ and $\tilde{x} = r$ can be obtained by integrating the effective fracture opening (G.3)

$$\mathcal{V}(\Delta s) = H\int_{r-\Delta s}^{r} \bar{w}_a d\tilde{x} = \frac{w_a(\Delta s)}{(2r\Delta s)^{\delta}}\frac{\sqrt{\pi}\Gamma\left(\delta+1\right)}{\Gamma\left(\delta+\frac{3}{2}\right)}\left(r\Delta s^2 - \frac{\Delta s^3}{3}\right), \tag{G.4}$$

where, additionally, α has been substituted from equation (G.2) into equation (G.3) and the function $w_a(\Delta s)$ can be obtained from (C.4).

The volume of the tip element given by Eq. G.4 is used in the numerical algorithm to compute the fracture extension, the tractions, and to update the mesh with new elements, as described in Appendix D.

G.2 Discretized governing equations

This section describes the discretization of the governing equations in the mEP3D model. Similar to Appendix E, where we described the mEPN algorithm, the numerical calculation of stress requires mesh expansion by refining the tip elements. The original mesh of size N is replaced by the expanded mesh of size N_e. The normal and

shear displacement discontinuities vectors are $\boldsymbol{D}_n$ and $\boldsymbol{D}_s$, and the stress tensor components are $\boldsymbol{\sigma}_n$ and $\boldsymbol{\sigma}_s$. Specific to the mEP3D algorithm, the approximation for the displacement discontinuity (4.6) adds additional vectors $\boldsymbol{D}_n^h = (D_n^{h,(1)}, \ldots, D_n^{h,(N_e)})^T$ and $\boldsymbol{D}_n^{h_{\Delta\sigma}} = (D_n^{h_{\Delta\sigma},(1)}, \ldots, D_n^{h_{\Delta\sigma},(N_e)})^T$, constructed from $\boldsymbol{D}_n$ using equations (B.12) and (B.15). It is worth mentioning, that the size of vector $\boldsymbol{D}_n$ is N_e, while the size of $\bar{\boldsymbol{w}}$ is N. Those vectors denote the same physical quantity but correspond to different meshes, the expanded and the original.

The elasticity relation, computed using the stress integral (2.6) and the approximation for the elastic potential (4.8), is written as

$$\begin{aligned} \boldsymbol{\sigma}_n &= \boldsymbol{C}_{nn}^h \boldsymbol{D}_n^h + \boldsymbol{C}_{nn}^{h_{\Delta\sigma}} \boldsymbol{D}_n^{h_{\Delta\sigma}} + \boldsymbol{C}_{ns}^h \boldsymbol{D}_s, \\ \boldsymbol{\sigma}_s &= \boldsymbol{C}_{sn}^h \boldsymbol{D}_n^h + \boldsymbol{C}_{sn}^{h_{\Delta\sigma}} \boldsymbol{D}_n^{h_{\Delta\sigma}} + \boldsymbol{C}_{ss}^h \boldsymbol{D}_s, \end{aligned} \tag{G.5}$$

where $\boldsymbol{C}_{nn}^h$, $\boldsymbol{C}_{ns}^h$, $\boldsymbol{C}_{sn}^h$, and $\boldsymbol{C}_{ss}^h$ are the elasticity matrices corresponding to the ellipse with height h, while $\boldsymbol{C}_{nn}^{h_{\Delta\sigma}}$ and $\boldsymbol{C}_{sn}^{h_{\Delta\sigma}}$ are the elasticity matrices corresponding to the ellipse with height $h_{\Delta\sigma}$. Each term on the right hands side of (G.5) represents matrix-vector multiplication. The stress tensor can be expressed solely in terms of $\boldsymbol{D}_n$ and $\boldsymbol{D}_s$ through the updated elasticity matrices yielding

$$\begin{aligned} \boldsymbol{\sigma}_n &= \boldsymbol{C}_{nn} \boldsymbol{D}_n + \boldsymbol{C}_{ns} \boldsymbol{D}_s, \\ \boldsymbol{\sigma}_s &= \boldsymbol{C}_{sn} \boldsymbol{D}_n + \boldsymbol{C}_{ss} \boldsymbol{D}_s. \end{aligned} \tag{G.6}$$

The latter expression is similar to Eq. (E.4). Here, however, the elasticity matrices $\boldsymbol{C}_{nn}$, $\boldsymbol{C}_{ns}$, $\boldsymbol{C}_{sn}$, and $\boldsymbol{C}_{ss}$ are defined differently than in Eq. (E.4).

The stress boundary conditions (4.9) and the elasticity relation (G.6) are used to obtain the shear displacement discontinuity $\boldsymbol{D}_s$ as

$$\boldsymbol{D}_s = -\boldsymbol{C}_{ss}^{-1}\boldsymbol{C}_{sn}\boldsymbol{D}_n, \tag{G.7}$$

and the effective fluid pressure $\hat{\boldsymbol{p}}$ on the expanded mesh as

$$\hat{\boldsymbol{p}} = -\left(\boldsymbol{C}_{nn} - \boldsymbol{C}_{ns}\boldsymbol{C}_{ss}^{-1}\boldsymbol{C}_{sn}\right)\boldsymbol{D}_n. \tag{G.8}$$

Because $\hat{\boldsymbol{p}}$ represents the expanded mesh, we extract the subset of size N required for the fluid flux calculation. In addition, the $\boldsymbol{D}_n$ is replaced by $\bar{\boldsymbol{w}}$, which is represented by Eq. (E.7).

The mEP3D model implements a procedure for the fluid pressure calculation that accounts for the singularity at the wellbore. The vector of local pressure values $\boldsymbol{p}_l$ must be computed from $\bar{\boldsymbol{p}}$ using relation (4.23). Let us denote the gradient operator on the left-hand side of (4.23) as $\boldsymbol{K}$ which acts on $\boldsymbol{p}$, and the gradient operator with a factor on the right-hand side as $\boldsymbol{K}_l$ which acts on $\boldsymbol{p}_l$, i.e.,

$$\boldsymbol{K}\bar{\boldsymbol{p}} = \boldsymbol{K}_l\boldsymbol{p}_l. \tag{G.9}$$

This system is underdetermined, since there is no constraint on the baseline value of $\boldsymbol{p}_l$. Before this expression can be used to find $\boldsymbol{p}_l$, it is necessary to add an additional requirement for possible values of $\boldsymbol{p}_l$. The approximate elasticity relation (E.7) can be used to relate the local pressure $\boldsymbol{p}_l$ and the volume of the fracture. The inverse

elasticity matrix is applied to the local pressure vector to obtain the vector of effective fracture opening. The distribution of this effective fracture opening between elements near the wellbore is inaccurate. The total volume associated with this vector of effective fracture opening must be equal to the real volume of the fracture. The real volume of the fracture can also be represented by the effective pressure and the elasticity matrix. Given this, the volume constrain reads as

$$\Delta\tilde{\boldsymbol{x}}^T \boldsymbol{C}^{-1} \boldsymbol{p}_l = \Delta\tilde{\boldsymbol{x}}^T \boldsymbol{C}^{-1} \bar{\boldsymbol{p}}. \tag{G.10}$$

The derived relation is combined with $\boldsymbol{K}$ and $\boldsymbol{K}_l$ to obtain the updated operators $\hat{\boldsymbol{K}}$ and $\hat{\boldsymbol{K}}_{\boldsymbol{l}}$. The vector of local pressure values can then be computed from the effective pressure as

$$\boldsymbol{p}_l = \hat{\boldsymbol{K}}_l^{\ -1} \hat{\boldsymbol{K}} \bar{\boldsymbol{p}}. \tag{G.11}$$

Next, the reduced vector of local pressure values containing wellbore elements $\boldsymbol{p}_w$ is extracted from $\boldsymbol{p}_l$. The global fluid balance given by Eq. (2.9) and (2.10), is represented by Eq. (E.8).

Several terms in the lubrication equation are discretized, similar to the mEPKN model. The time derivative is discretized by the backward finite difference in Eq. (E.9). The derivative of flux is discretized by the central difference scheme in Eq. (E.11). The flux at the crack front is zero.

The flux at the edge between adjacent elements i and j differs from Eq. (E.12),

and can be written by discretizing equation (4.12) as

$$\bar{q}_{\tilde{x}}^{(i+)} \approx -\frac{1}{H\mu'} \frac{\bar{p}^{(j)} - \bar{p}^{(i)}}{\tilde{x}^{(j)} - \tilde{x}^{(i)}} \sum_{m=0}^{N_y} \left[\left(\frac{w^{(j,m)} + w^{(i,m)}}{2} \right)^3 \Delta\tilde{y}^{(m)} \right], \tag{G.12}$$

where the sum corresponds to the integral of w_k^3 over $\tilde{y}$, and $\Delta\tilde{y}^{(m)}$ is the integration step in the vertical direction

The leak-off term is included in the mEP3D model. The arising integral is computed numerically for i_{th} element as

$$\left(\frac{1}{H} \int_{-h_k/2}^{h_k/2} \frac{C'}{\sqrt{t - t_{0,k}(\tilde{x}, \tilde{y})}} \, d\tilde{y} \right)^{(i)} \approx \frac{C'}{H} \sum_{m=1}^{N_h} \frac{\Delta h^{(i,m)}}{\sqrt{t - t_0^{(i,m)}}}, \tag{G.13}$$

where $\Delta h^{(i,m)}$ and $t_0^{(i,m)}$ track the position of the fracture front in time by storing the time history of height growth for each fracture element. At $m = 0$, the value $t_0^{(i,0)}$ denotes the time step when the fracture front reached $\tilde{x}^{(i)}$. For $m = 1, \ldots, N_h$, the value $t_0^{(i,m)}$ is the m_{th} time step after $t_0^{(i,0)}$ and $\Delta h^{(i,m)}$ is the corresponding height increment at $\tilde{x}^{(i)}$. The leak-off values from (G.13) are combined into the vector $\boldsymbol{q}_l$.

The discretized form of the source term is given by Eq. (E.13). The source term (E.13) is represented by the vector $\boldsymbol{q}_s$.

Finally, the lubrication equation can be written as

$$\left[\frac{1}{\Delta t} \boldsymbol{I} - \boldsymbol{AC} \right] \bar{\boldsymbol{w}} = -\boldsymbol{q}_l + \boldsymbol{q}_s + \frac{1}{\Delta t} \bar{\boldsymbol{w}}^0, \tag{G.14}$$

or, equivalently, as

$$\boldsymbol{L}\bar{\boldsymbol{w}} = \boldsymbol{b}, \tag{G.15}$$

where

$$\boldsymbol{L} = \frac{1}{\Delta t}\boldsymbol{I} - \boldsymbol{AC}, \qquad \boldsymbol{b} = -\boldsymbol{q}_l + \boldsymbol{q}_s + \frac{1}{\Delta t}\bar{\boldsymbol{w}}^0. \tag{G.16}$$

The nonlinear system (G.15) is solved as a linear system. First, $\bar{\boldsymbol{w}}$ is computed, then $\boldsymbol{h}$, $\boldsymbol{L}$, $\boldsymbol{b}$, $\boldsymbol{Q}$, and the position and direction of the lateral fracture fronts are updated. The process repeats until convergence. The solution $\bar{\boldsymbol{w}}^0$ at the first time step is calculated from the radial fracture solution (Dontsov, 2016).

The direction of the lateral front propagation is determined by the zero Mode II criteria (4.16). The tip element is allowed to change its angle until the splitting, and then the resultant new inner element has fixed orientation in space. The turn angle of the tip element is computed to ensure the components of $\boldsymbol{D}_s$ corresponding to the tip elements are zero, which is equivalent to $K_{II} = 0$ at the crack tip. The vector $\boldsymbol{D}_s$ is given by equation (G.7). The lateral extension of the fracture is guided by the growth of the tip elements, the lengths of which are computed from the effective fracture opening using equations (G.4) and (D.1).